5-2012

# Investigation of Negative Differential Resistance Phenomena in Quantum Well Heterostructures

Nazariy Andrushchak
*University of Arkansas, Fayetteville*

# INVESTIGATION OF NEGATIVE DIFFERENTIAL RESISTANCE PHENOMENA IN QUANTUM WELL HETEROSTRUCTURES

# INVESTIGATION OF NEGATIVE DIFFERENTIAL RESISTANCE PHENOMENA IN QUANTUM WELL HETEROSTRUCTURES

A thesis submitted in partial fulfillment
of the requirements for the degree of
Master of Science in Microelectronics-Photonics

By

Nazariy Andrushchak
Lviv Polytechnic National University
Master of Science in Telecommunication and Information Systems, 2008
Lviv Polytechnic National University
Bachelor of Science in Telecommunications, 2007

May 2012
University of Arkansas

## Abstract

Increasing interest in entirely new possibilities for quantum mechanical description of carriers transport is becoming more evident with the developing advancements in epitaxial growth technique. Consequently, molecular beam epitaxy (MBE) technique is considered to be the most precise technique that allows the growth of ultra-thin layers of different compositions.

Those structures can be designed to investigate the wave-nature of carriers, which broadens the possibilities in device design and fabrication for a specific area. In this thesis the fundamental study of the real space charge transfer (RST) mechanism that took place in quantum well heterostructures and led to the negative differential resistance observation is presented. Using the Hall effect measurement technique, the mobility and carrier concentration were measured and analyzed by considering different scattering mechanisms and carrier thermal activation phenomena, respectively.

Deep level noise spectroscopy (DLNS) was used to investigate and probe the materials for the presence of defects and impurity states, which were needed to achieve the RST. The pulsed I-V measurements were performed to observe the negative differential resistance (NDR). Finally, the lock-in technique and pulsed I-V technique with light excitation and temperature cycling were used to prove the presence of RST mechanism in our system. The results of this study can be implemented to create devices for high frequency applications.

This dissertation is approved for recommendation
to the Graduate Council.

Thesis Director:

_____
Dr. Gregory Salamo

Thesis Committee:

_____
Dr. Keith Roper

_____
Dr. Simon Ang

_____
Prof. Ken Vickers

The following signatories attest that all software used in this thesis was legally licensed for use by Mr. Nazariy Andrushchak for research purposes and publication.

_____ _____
Mr. Nazariy Andrushchak, Student Dr. Gregory Salamo, Thesis Director

This dissertation was submitted to http://www.turnitin.com for plagiarism review by the Turnltlncompany's software. The signatories have examined the report on this dissertation that was returned by TurnItln and attest that, in their opinion, the items highlighted by the software are incidental to common usage and are not plagiarized material.

_____ _____
Prof. Ken Vickers, Program Director Dr. Gregory Salamo, Thesis Director

**Thesis Duplication Release**

I hereby authorize the University of Arkansas Libraries to duplicate this thesis when needed for research and/or scholarship.

Agreed _____
**Nazariy Andrushchak**

Refused _____
**Nazariy Andrushchak**

**Acknowledgments**

In the first place I would like to thank my academic advisor Dr. Gregory Salamo, who was willing to accept me as a Master's student into his research group. Without him, and the wonderful research facilities that he has provided here at the University of Arkansas, this work would never have been possible. I really appreciate his numerous advises and unique physical approach to understand complicated quantum mechanism in the simple way. He made me think as a scientist (not as an engineer, as I used to be) in order to accomplish my research and to explain the results from the scientific point view.

I gratefully acknowledge Dr. Vasyl Kunets for his wise advice, supervision, and reasonable critical contributions to the successful finish of this thesis. He introduced me to the real world of solid state physics, different setups operation and principles of device fabrication. I am very thankful to Dr. Kunets for his valuable advices in science discussions and supervision in performing experiments. Also, I would like to thank Dr. Kunets for reading this thesis and giving his critical comments about it. I have learned a lot from working together with Dr. Kunets, and not just how to be a great scientist, but also how to be a good husband, father and honest person.

I would also like to thank my committee members, Dr. Keith Roper, Dr. Simon Ang, and Prof. Ken Vickers, for agreeing to participate in my thesis defense, and I would like to acknowledge their support and encouragement.

Additional thanks I would like to give to Prof. Vickers for guiding me throughout all process of preparing and writing of my thesis. His advice helped me to improve the quality of writing and also to pay more attention to formatting issues.

Many thanks I would like to give to Dr. Morgan Ware for his valid contribution to my presentation and for better understanding of quantum physics mechanisms.

My special thanks go to Colin Furrow. Without him this thesis would be unintelligible to read at all due to my Ukrainian accent throughout the whole thesis.

I would like to thank my mother, Galina and brother, Maryan, for encouragement and truthful belief in my ability to finish this thesis successfully. They are the closest people in the world, I really love them and I will always be thankful for having them in my life.

Also, I would like to thank the Fulbright International Educational Program for providing me a scholarship for my education at the University of Arkansas. Without this program my interesting and outstanding journey to the world of novel semiconductor physics will never happened. And my special thanks to Emily Bosio from Institute of International Education for her support and willingness to help at different situations.

Finally, I would like to thank everybody who was important to the successful realization of this thesis, as well as expressing my apology that I could not mention personally one by one.

**Table of Contents**

**Chapter 1. Introduction ..... 1**

1.1. Research Project Overview ..... 3

1.2. Theory of Negative Differential Resistance ..... 4

1.2.1. Real Space Charge Transfer Effect ..... 6

1.2.2. Transferred-Electron Effect ..... 8

1.3. Gunn Effect Theory ..... 10

1.4. Gunn Oscillations Formation ..... 11

**Chapter 2. Theory of Quantum Well Heterostructures with Remote Doping ..... 14**

2.1. Principles of Molecular Beam Epitaxy Growth ..... 14

2.2. Theory of Quantum Well Heterostructures (QWHs) ..... 16

2.2.1. Theory of Heterostructures ..... 16

2.2.2. QWHs Advantages ..... 18

2.2.3. Mechanisms of QWHs Formation ..... 19

2.3. Applications of QWHs ..... 20

**Chapter 3. MBE Growth and Hall Effect Measurements ..... 21**

3.1. AlGaAs/GaAs QW Heterostructure Growth ..... 21

3.2. Mobility in Semiconductors ..... 26

3.3. Hall Effect Measurements ..... 27

3.4. Scattering Mechanisms in AlGaAs/GaAs Structures ..... 30

3.5. Scattering in Bulk GaAs ..... 31

3.5.1. Scattering on Ionized Impurities ..... 31

3.5.2. Phonon or Lattice Scattering ..... 32

3.5.3. Acoustic Phonons Scattering: Deformation Potential ..... 32

3.5.4. Acoustic Phonon Scattering: Piezoelectric Scattering ..... 32

3.5.5. Optical Phonons Scattering: Polar Scattering ..... 33
3.6. Scattering in QW Heterostructures ..... 33
3.6.1. Scattering by Remote Ionized Impurities ..... 35
3.6.2. Scattering by Interface Roughness ..... 36
3.6.3. Alloy Scattering ..... 36
3.7. Experimental Mobility and Density Data Discussion ..... 38
3.7.1. Mobility ..... 38
3.7.2. Carrier Concentration ..... 42
**Chapter 4. Experimental Device Fabrication ..... 45**
4.1. Processes for Experimental Device Fabrication ..... 45
4.1.1. Photolithography Technique ..... 45
4.1.2. Etching Technique ..... 48
4.1.3. Ohmic and Schottky Contacts Theory and Formation ..... 49
4.1.4. Lift-off Technique ..... 52
4.1.5. Annealing Technique ..... 53
4.2. Contact Resistance Optimization ..... 54
4.3. Completed Experimental Device ..... 58
**Chapter 5. Methodology of Noise Measurements ..... 60**
5.1. Types of Noise in Semiconductor Devices ..... 60
5.1.1. Shot Noise ..... 61
5.1.2. Thermal Noise ..... 61
5.1.3. 1/f Noise (Flicker Noise) ..... 61
5.1.4. Generation-Recombination (GR) Noise ..... 64
5.2. Noise Spectroscopy of Deep Traps ..... 66
5.3. Experimental Setup and Measurement Results ..... 70

5.3.1. Installation and Setup Calibration....70
5.3.2. Low Frequency Noise Measurements....73
5.3.3. 1/f Noise and Hooge Parameter....75
5.3.4. Generation-Recombination Noise and Impurity States in AlGaAs Barriers....79
5.3.5. Generation-Recombination Noise Results Discussion....87
**Chapter 6. Pulsed I-V Measurements....91**
6.1. I-V Measurements in the Dark....91
6.2. I-V Measurements with Exposure to Light....94
6.2.1. Lock-in Technique....96
**Chapter 7. Conclusions....101**
**Chapter 8. Future Work....105**
**Appendix A: Noise Spectra Analysis on the Matter of Traps and Impurity States for All Samples....111**
**Appendix B: Description of Research for Popular Publication....118**
**Appendix C: Executive Summary of Newly Created Intellectual Property....121**
**Appendix D: Potential Patent and Commercialization Aspects of listed Intellectual Property Items....122**
**Appendix E. Societal and Environmental Impact of Research....124**
**Appendix F: Microsoft Project for MS Microelectronics-Photonics Degree Plan....125**
**Appendix G: Software Used in This Research....128**

## List of Figures

Figure 1.1. The I-V measurement curve for semiconductor device system with (a) typical I-V behavior, and (b) in system that has negative differential resistance region……...…4

Figure 1.2. I-V characteristics: (a) voltage-controlled I-V curve (N shape), (b) current-controlled I-V curve (S shape) [7]……....5

Figure 1.3. Energy-band diagram that shows the RST mechanism occurring at applied high electric field [5]……6

Figure 1.4. The energy-band diagram structure of the GaAs[11]……9

Figure 1.5. The process of domain formation: (a) typical v-E electrons behavior to achieve NDR and some relevant important points, (b) a small dipole formation, (c) a mature domain [5]…....12

Figure 2.1. Schematic view of the MBE chamber for III-V semiconductor layers [15]……...15

Figure 2.2. Typical view of RHEED screen while growing a crystalline material on top of GaAs [16]……...16

Figure 2.3. The main types of heterostructures: (a) – type I; (b) – type II; (c) – type III [17]…..……17

Figure 2.4. Bandgap diagrams for (a) single quantum well and (b) stepped quantum well [20]…….19

Figure 3.1. Schematic diagram of $Al_{0.3}Ga_{0.7}As$ epilayer uniformly doped by Si: growth (left), and its corresponding conduction band diagram (right) ($REF_U$ sample)……..21

Figure 3.2. Schematic diagram of $Al_{0.3}Ga_{0.7}As$ epilayer with multiple Si δ-dopants growth (left), and its corresponding conduction band diagram (right) ($REF_\delta$ sample)……....22

Figure 3.3. Schematic diagram of the GaAs quantum well heterostructure with Si δ-dopants in $Al_{0.3}Ga_{0.7}As$ barriers (left). The corresponding schematic diagram of the conduction band is shown (right). The growth conditions were kept the same for all samples $E_{1.0}$, $E_{0.8}$, $E_{0.5}$. The difference was only the doping level as it is shown in Table 3.1……..24

Figure 3.4. Schematic diagram of the preparation layer for the structure of the GaAs quantum well heterostructure with Si δ-dopants in $Al_{0.3}Ga_{0.7}As$ barriers…….....25

Figure 0.1. The simple quantum well heterostructure grown by MBE with ohmic contacts on top……..26

Figure 3.6. The sample of the special dimensionality to measure the Hall effect……..…28

Figure 3.7. Different possible carrier scattering mechanisms in AlGaAs/GaAs structure [10]…30

Figure 3.8. Different scattering mechanisms in GaAs sample and their influence on the mobility at different temperatures, where curves correspond to the calculated and circles to the measured mobility [28]……..……33

Figure 3.9. The schematic view of the conduction band diagram for AlGaAs/GaAs heterostructure junctions [29]……..…..34

Figure 3.10. A schematic view of the AlGaAs/GaAs quantum well that shows variations of the well thickness, which is the source of the interface roughness [29]……..36

Figure 3.11. Typical electron mobility behavior of semiconductors at different temperatures for various dopants concentration. Insert presents the theoretical temperature dependence of electron mobility [5]……37

Figure 3.12. A plot of temperature dependent measurements of electron mobility and density for $Al_{0.3}Ga_{0.7}As$ sample doped Si uniformly ($REF_U$)……...……...38

Figure 3.13. A plot of temperature dependent measurements of electron mobility and density for $Al_{0.3}Ga_{0.7}As$ sample with multiple Si δ-dopants ($REF_\delta$)……39

Figure 3.14. A plot of temperature dependent measurements of electron mobility and density for GaAs QW (sample $E_{1.0}$) with Si -dopants of $N_d=1x10^{12}cm^{-2}$ in AlGaAs barriers…….....40

Figure 3.15. A plot of temperature dependent measurements of electron mobility and density for GaAs QW ($E_{0.8}$, $Nd=8x10^{11}cm^{-2}$)……..41

Figure 3.16. plot of temperature dependent measurements of electron mobility and density for GaAs quantum well ($E_{0.5}$, $Nd=5x10^{11}cm^{-2}$)……..…….41

Figure 3.17. A plot of temperature dependent measurements of electron mobility for all GaAs quantum well samples ($E_{1.0}$, $E_{0.8}$, $E_{0.5}$ samples)……...……..42

Figure 3.18. A plot of temperature dependent measurements of electron density for GaAs quantum wells with Si δ-dopants ($E_{1.0}$, $E_{0.8}$, $E_{0.5}$ samples)……...43

Figure 3.19. A schematic structure of QW Si δ-doped sample (a), and the equivalent circuit consisting of three resistors (b)……..……44

Figure 4.1. A pattern of positive and negative photoresist after exposure to UV light and their development……...46

Figure 4.2. A typical Schottky contact barrier that is formed on metal-semiconductor interface under unbiased and biased conditions: (a) no bias; (b) forward bias; (3) reverse bias. $j_{1e}$ and $j_{3e}$ are injection current, and $j_{2e}$ is a tunneling current [27]……..…..50

Figure 4.3. Ideal I-V curves for ohmic (red) and Schottky (blue) contacts…….…..52

Figure 4.4. Experimentally measured I-V characteristics of ohmic contacts for different annealing time at ambient environment of $N_2$ gas……...……..54

Figure 4.5. (a) A standard TLM contact-resistance pattern with corresponding contact width and length, (b) a transmission-line-model equivalent circuit for current flow in a thin-layer semiconductor device…….55

Figure 4.6. An experimental TLM structure that was used to perform measurements of the contact resistance…….……..55

Figure 4.7. The expected resistance R as a function of contact-spacing Li for the pattern depicted in Figure 4.5a [27]…….…….56

Figure 4.8. A plot of contact resistance versus doping concentration at room temperature for QW heterostructure samples……..57

Figure 4.9. A plot of contact resistance versus temperature for $E_{1.0}$ sample……..…57

Figure 4.10. The SEM image of different device structures that were achieved at the end of the device fabrication process…….….58

Figure 4.11. The SEM images of the devices that were used in (a) pulsed I-V measurements, (b) low-frequency noise spectra measurements……...…59

Figure 5.1. An example of three types of noise measured in noise voltage fluctuations of the GaAs sample [54]……..65

Figure 5.2. Two different ways to display noise data [63]……....67

Figure 5.3.The plots to determine the slope $\theta_T$ and $\theta_S$ ……...……69

Figure 5.4. Schematic presentation of noise measurement setup for extracting of noise spectra..71

Figure 5.5. An example of a fitted spectrum for $E_{1.0}$ sample with 220 kOhm load resistor at T = 294 K……..74

Figure 5.6. (a) Noise voltage spectra for $E_{1.0}$ sample for various biases. The bias current increases from bottom curve (I = 29 μA) to top curve (I = 450 μA); (b) Plot of the amplitude of 1/f noise *A* versus $V^2$ for $E_{1.0}$ sample……....76

Figure 5.7. (a) Noise voltage spectra for $E_{0.8}$ sample for various bias currents. The bias current increases from bottom curve (I = 29 μA) to top curve (I = 660 μA); (b) Plot of the amplitude of 1/f noise *A* versus $V^2$ for $E_{0.8}$ sample…….77

Figure 5.8. a) Noise voltage spectra for E0.5 sample for various bias currents. The bias current increases from bottom curve (I = 29 μA) to top curve (I = 1.05 mA); (b) Plot of the amplitude of 1/f noise *A* versus $V^2$ for $E_{0.5}$ sample…….....77

Figure 5.9. Dependency of the Hooge parameter versus the electron mobility for three GaAs QW samples with different doping in the barriers…….....78

Figure 5.10. Dependency of the Hooge parameter versus the dopant concentration for three GaAs quantum well samples……....79

Figure 5.11. (a) Measured voltage noise spectral density for $REF_U$ sample. The spectra are shown in different temperature ranges as four separate graphs to distinguish presence of four different traps. Each trap is detected as unique generation-recombination process in for certain temperature range, (b) noise spectral density $S_{noise}$ versus temperature *T* and frequency…….81

Figure 5.12. a) Measured voltage noise spectral density for $E_{1.0}$ sample. The spectra are shown in different temperature ranges as four separate graphs to distinguish presence of three different traps. Each trap is detected as unique generation-recombination process in for certain temperature range, (b) noise spectral density $S_{noise}$ versus temperature *T* and frequency…….82

Figure 5.13. a) Measured voltage noise spectral density for $E_{0.8}$ sample. The spectra are shown in different temperature ranges as four separate graphs to distinguish presence of four different traps. Each trap is detected as unique generation-recombination process in for certain temperature range, (b) noise spectral density $S_{noise}$ versus temperature *T* and frequency…….83

Figure 5.14. a) Measured voltage noise spectral density for $E_{0.5}$ sample. The spectra are shown in different temperature ranges as four separate graphs to distinguish presence of four different traps. Each trap is detected as unique generation-recombination process in for certain temperature range, (b) noise spectral density $S_{noise}$ versus temperature *T* and frequency…….84

Figure 5.15. a) Measured voltage noise spectral density for $REF_{\delta}$ sample. The spectra are shown in different temperature ranges as four separate graphs to distinguish presence of three different traps. Each trap is detected as unique generation-recombination process in for certain temperature range, (b) noise spectral density $S_{noise}$ versus temperature $T$ and frequency…….85

Figure 6.1. The experimental setup for pulsed I-V measurements……....92

Figure 6.2. I-V measurement curves for $E_{1.0}$ sample (a) at 82 K after the sample was cooled down; and (b) after temperature of device was increased up to 390 K and then cooled down to 82 K…….....93

Figure 6.3. The experimental setup for I-V measurements with exposure to light…….....94

Figure 6.4. I-V curves for $E_{1.0}$ sample after exposure to light ($\lambda$ = 514 nm): (a) after first exposure, (b) after second exposure…..……..95

Figure 6.5. The experimental setup for noise signal measurements using lock-in amplifier…....97

Figure 6.6. Noise signal measurements using lock-in amplifier for sample $E_{1.0}$; (a) after cooling down to 82 K, (b) after applying of 5.5 V, (c) after applying of 8 V, (d) after the light exposure ($\lambda$ = 514 nm)……..…..98

## List of Tables

Table 3.1. The main parameters of samples that were grown by MBE and used in further measurements…….23

Table 4.1. The recipe for spin coater that was used to apply a photoresist……...47

Table 5.1. Trap characteristics for all samples used in this study……..87

# Chapter 1. Introduction

For many years the movement of charge carriers in bulk semiconductor materials was studied as one of the unique and fundamental features in solid state physics. For the last decade, investigation in this branch of solid state physics has made it possible to develop solid state electronics. However, with recent developments of new semiconductor growth techniques, such as Molecular Beam Epitaxy (MBE) and Metalorganic Chemical Vapor Deposition (MOCVD), ultra-thin materials of different compositions and interfaces as sharp as an atomic monolayer are readily available. When the thickness of the semiconductor structures becomes comparable to the deBroglie wavelength, usually about 0.1 nm to 1 nm, the transport properties have to be determined using a quantum mechanical theory approach.

By restricting carrier movement in a specific dimension, it is possible to widen the application of the quantum phenomena. During the last decade, quantum well heterostructures in III-V materials have drawn interest because of their extremely high electron mobilities. These high mobilities are possible due to the spatial separation of ionized impurities and the formation of a two-dimensional electron gas (2DEG). Many investigations were done to understand how these systems work and, based on the results, high electron mobility transistors (HEMT) were fabricated [1, 2].

Hot carrier transport instabilities in low-dimensional semiconductor structures have also attracted a lot of attention. By applying a high electric field across a semiconductor system (with quantum confinement), new types of instabilities can be observed, which are not observed in bulk materials. In particular, the oscillatory instabilities associated with hot electron transport are another important direction of experimental and theoretical studies for quantum well heterostructures [3]. It is possible to achieve these results because of new mechanisms of hot

carriers transfer in quantum well heterostructures, known as real space charge transfer (RST). The RST mechanism that takes place in quantum well heterostructures (explained later in this chapter) results in the observation of a negative differential resistance. Devices that use the principle of the negative differential resistance phenomena are in high demand for their applications in high-speed and high frequency electronics [4].

This thesis is organized in the following manner: in Chapter 1, the negative differential resistance (NDR) mechanisms are described and an introduction to the effects that led to the NDR are discussed. Also, the principle of domain formation for Gunn diodes, which uses the principle of NDR, is described. In Chapter 2,a brief overview of the MBE growth technique and the principles of quantum well heterostructure formation are presented. Chapter 3 mainly focuses on explaining the structure of the samples, grown by MBE, that were used in the experiments performed in this thesis. Different scattering mechanisms that might be present in bulk semiconductors and in the quantum well heterostructures are discussed. By performing Hall effect measurements, the temperature trends in the behavior of electron mobility and carrier concentration were investigated. Based on these experimental results and the theoretical understanding of scattering mechanisms, the behavior of mobility and carrier density for quantum well heterostructures are explained and compared to bulk materials. In Chapter 4, the device fabrication process and contact optimization using the Transmission Line Model (TLM) technique is presented. This allows for the estimation of contact resistance; which is important for accurate measurements of an electric field across the two terminal devices. Chapter 5 gives an overview of all available types of noises that might be present in quantum well heterostructures. In addition, the Deep Level Noise Spectroscopy (DLNS) technique was used to investigate impurities and deep level traps in semiconductors. In Chapter 6, pulsed I-V

measurements were performed to detect the NDR. The lock-in technique for noise signal measurements and pulsed I-V technique with light excitation and temperature cycling were used to detect real space charge transfer. The possible mechanism for carrier transfer in the quantum well heterostructure system is also presented. Finally, in Chapter 7, all experimental results were summarized to give the general overview of this work.

### 1.1. Research Project Overview

The main goal of this project was to experimentally observe the NDR in Quantum Well Heterostructures. Why is the investigation of the NDR phenomena important? The NDR phenomena has potential applications in high frequency devices. Thus, the study of alternative systems for devices able to generate or detect high frequency radiation is important.

It is well known that telecommunications and all its applications are moving into the range of high frequencies to provide more services with better quality. Therefore, the importance of devices that can perform in the THz frequency range increases. For that reason, this direction in the telecommunications area is under intense investigation.

Currently, one of the most commonly used types of device to perform at millimeter wavelengths is the Gunn diode, where the principle of NDR is successfully applied. It has been used as local oscillators and power amplifiers in the frequency range from 1 to 300 GHz. Also, transfer-electron devices (which use the principle of NDR) as solid-state microwave sources are used in radars, intrusion alarms, and microwave test instruments [5].

The crucial part of any device is the material where the unique electronic behavior takes place. In order to create a high-frequency device, the NDR has to be achieved in the material. One way to realize NDR is to fabricate material or material systems where at least two conduction bands are available: (1) one band of high mobility and (2) another band of low

mobility. The charge transfer from the high mobility band to the low mobility band can exhibit the NDR phenomena.

### 1.2. Theory of Negative Differential Resistance

By making I-V measurements across a two terminal semiconductor device with good ohmic contacts, i.e. by applying the electric field across the channel, the current will proportionally increase with an increasing of the electric field (see Figure 1.1a). At high electric fields, one can see that with further continuous increase of the electric field, the decrease of current across the device can be achieved in some systems. As shown in Figure 1.1b, from $V_T$ to $V_d$ the curve has a decrease in current despite the voltage increase. Hence, it exhibits a negative differential resistance region in this I-V curve, where differential means the change in the linearization of the function and Ohm's law, given by $U=IR$.

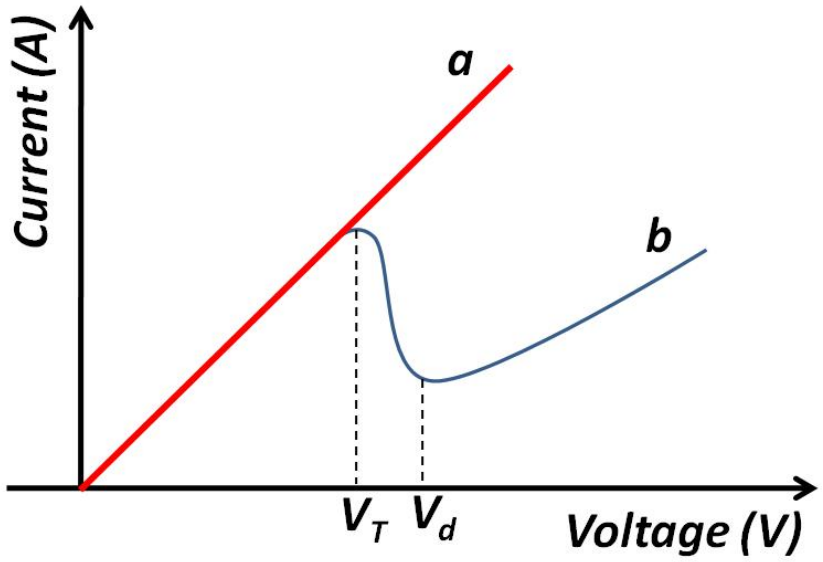


Figure 1.1.The I-V measurement curve for semiconductor device system with (a) typical I-V behavior, and (b) in system that has negative differential resistance region.

In bulk materials, because of the shape of the I-V curve, the NDR phenomena can be classified into two groups: voltage-controlled NDR (N-shaped) and current-controlled NDR (S-

shaped). The I-V curves for these two cases are shown in Figure 1.2. As described in [6], only in voltage-controlled NDR devices will high field domains be formed, and, in current-controlled NDR devices, high-current filaments will be formed [7].

There are two different mechanisms that lead to negative differential resistance – real space charge transfer and the transferred-electron effect. The similarity between these two mechanisms is that, by applying a high enough voltage, hot carriers (electrons that were heated up with electric field) will be transferred to a different band in k-space or to a different material in the real space. This transfer should happen from a high mobility band (low effective mass) to a low mobility band with higher effective mass. As a result of this transfer, the reduction of current will be observed at the higher voltage. The real space charge transfer effect occurs in semiconductor quantum well heterostructures while the transferred-electron effect occurs in bulk materials where transfer between $\Gamma$ and $L$ valleys in $k$- space occurs [5].

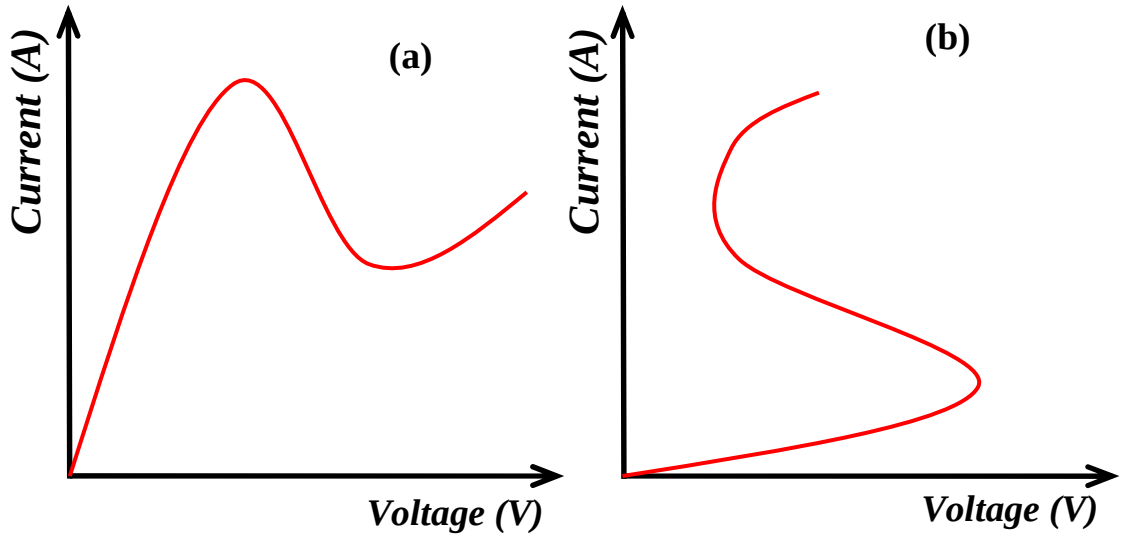


Figure 1.2. I-V characteristics: (a) voltage-controlled I-V curve (N shape), (b) current-controlled I-V curve (S shape) [7].

1.2.1. Real Space Charge Transfer Effect

The first experimental device that successfully applied the RST mechanism to obtain NDR was done in 1981 [8]. To observe RST, a special diode was fabricated with a AlGaAs/GaAs heterostructure. The RST and transferred-electron effect are very similar, and both can result in NDR [9]. Sometimes it is difficult, even experimentally, to separate those two effects. Despite this, these effects are different. For example, transferred-electron effect can occur for a homogeneous bulk sample. When the high electric field is applied to the sample and carriers are transferred in the *E-k* from the high mobility band to the band with lower mobility, the reduction of current will be observed and the NDR is measured. The transfer of carriers in RST takes place in real space compared to the transferred-electron effect that happens in k-space. The energy band diagram for an AlGaAs/GaAs sample is depicted in Figure 1.3.

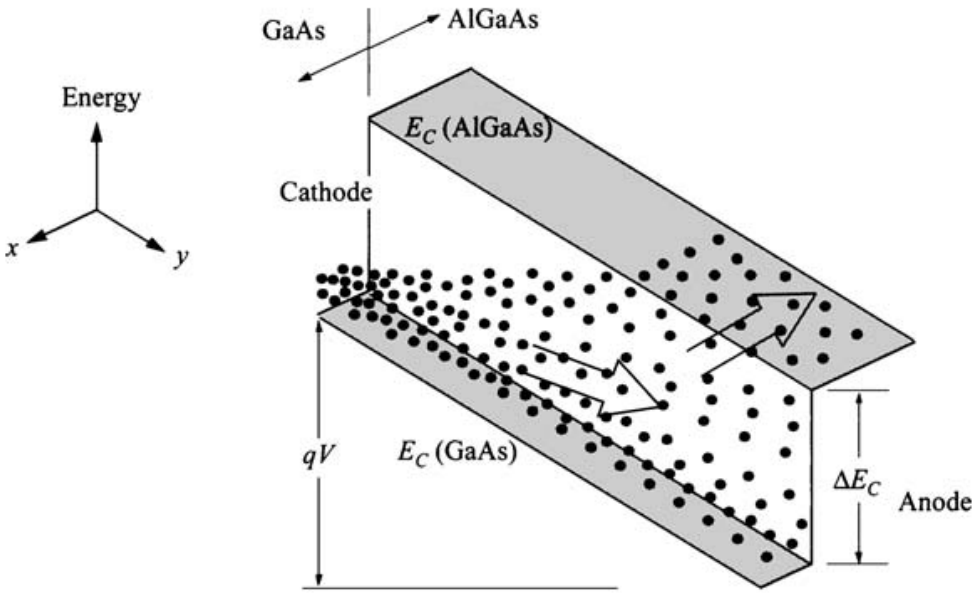


Figure 1.3. Energy-band diagram that shows the RST mechanism occurring at applied high electric field [5].

As seen in Figure 1.3,the carriers in the GaAs channel (high mobility and low effective mass) had enough energy to overcome the barrier and move towards the AlGaAs (low mobility

and high effective mass). Therefore, it is reasonable to say that NDR can be detected as the current decrease with an increase of the electric field [5, 6].

As it was previously mentioned, the RST effect is very similar to the transferred-electron effect and the I-V characteristics of these two effects are similar. In order to achieve an efficient RST diode, the heterostructure has to be chosen with optimum band-gap discontinuity between AlGaAs and GaAs compared to the $\Gamma$-$L$ band separation of GaAs.

Modeling the RST diode is a difficult task to accomplish. Hence, there are no simple equations that can be used for the specific current-voltage characteristics. However, if to use the theory that is presented in [5], the total drift current can be presented as

$$J = qn_{s1}\mu_1 E + qn_{s2}\mu_2 E = qN_s E\left[\mu_1 - (\mu_1 - \mu_2)F\right], \tag{1.1}$$

and from the Equation 1.1 the differential resistance is given as

$$\frac{dJ}{dE} = qN_S\left[\mu_1 - (\mu_1 - \mu_2)F - E(\mu_1 - \mu_2)\frac{dF}{dE}\right], \tag{1.2}$$

where $J$ is the density of current, $E$ is the electric field, $\mu_1$ and $\mu_2$ are mobilities in GaAs and AlGaAs, respectively, $F$ is the fraction of carriers that are excited to the AlGaAs layer ($F=n_{S2}/N_S$, $n_{S2}$ is number of carriers in AlGaAs layer, $N_s=n_{s1}+n_{s2}$ is the total number of carriers in AlGaAs layer and GaAs, $n_{S1}$ is a number of carriers in GaAs layer).

The main advantage of the RST diode is very high-speed operation. As it is known, the response time of the system is limited by the carriers' movement across the hetero-interface of two materials. In regular diodes, the transit time of carriers between the cathode and anode plays the dominant role. Since this mechanism is not present in RST diodes, they can perform much faster than the regular diodes.

1.2.2. Transferred-Electron Effect

The transferred-electron effect can be explained as the transfer of electrons from the high mobility band valley to the low mobility band valley in bulk materials. In order to understand the NDR mechanism, let us examine the energy-momentum (*E*-*k*) diagram of GaAs as depicted in Figure 1.4. As seen in Figure 1.4,the GaAs conduction band consists of a number of subbands. The very bottom of the conduction band, which corresponds to the *Γ*-valley, is positioned at k=0. The next higher subband is the *L*-valley, and another one is the *X*-valley. This is why the ordering of the subbands in GaAs is *Γ*-*L*-*X* [5].

The energy separation between *Γ* and *L* valleys is $\Delta E=E_L-E_g$. In GaAs, this energy is around 0.31eV. In the *Γ*-valley, the effective mass of electrons is $m_1^*$and the mobility is $\mu_1$. The same quantities for the *L*-valley are $m_2^*$ and $\mu_2$, respectively. The current density of GaAs can be characterized using the equation

$$J = q(\mu_1 n_1 + \mu_2 n_2)E = qn\upsilon, \tag{1.3}$$

where $n_1$ and $n_2$are carrier concentrations in high and low mobility valleys, respectively, $n=n_1+n_2$is the total carrier concentration, and the average drift velocity υ can be given as [6]

$$v = \left(\frac{\mu_1 n_1 + \mu_2 n_2}{n_1 + n_2}\right)E \approx \frac{\mu_1 E}{1+(n_2/n_1)}, \tag{1.4}$$

The last part of the Equation (1.4) is valid for $\mu_1 >> \mu_2$.

The origin of the NDR mechanism is different in transferred-electron effect devices, compared to RST diodes, because the drift velocity is field dependent. This field-dependent velocity results in the formation of domains, which were first observed by Gunn as current pulses.

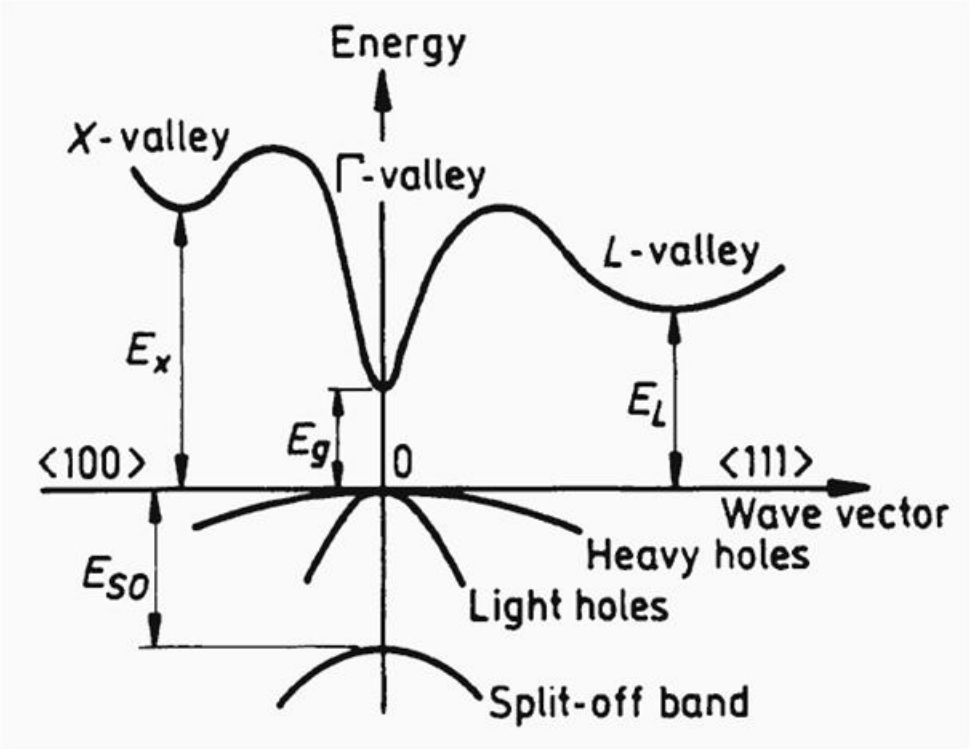


Figure 1.4. The energy-band diagram structure of the GaAs[11].

To understand the NDR phenomena in GaAs heterostructures, the differential mobility $\mu_d$ is introduced, and can be defined as

$$\mu_d = \frac{dv}{dE}. \tag{1.5}$$

This differential mobility is different from the regular low-field mobility, defined as $\mu=v/E$. As it can be seen from the last equation, the low-field mobility does not depend on the field. However, this is not the same with the differential mobility.

The differential mobility can be given as [5]

$$\mu_d = \frac{dv}{dE} = \mu_1(1-P) + (v_s - \mu_1 E)\frac{dP}{dE}, \tag{1.6}$$

where $P$ is the population fraction that can be defined as $P=n_2/(n_1+n_2)$. It can be shown that $\mu_d$ is negative under certain conditions [5]

$$\frac{dP}{dE} > \frac{1-P}{E-(v_s/\mu_1)}. \tag{1.7}$$

In order for the material to give rise to NDR, certain requirements have to be met. First, the lattice temperature has to be low enough, so all the electrons without the presence of an electric field are located in the lower conduction band valley. Second, in the lower conduction band valley, the effective mass has to be smaller and the mobility of the electrons has to be high. Also, in the satellite valley, the electrons must have large effective mass and low mobility. Third, the semiconductor bandgap energy must be larger than the separation between the two valleys to prevent the avalanche breakdown from happening before the electrons will start to be transferred into the higher valleys [6].

### 1.3. Gunn Effect Theory

In 1963, the Gunn Effect was first performed by Gunn at Bell Laboratories. Gunn observed that microwave current-pulses, which were repetitive in time, were generated when a DC voltage was applied to the n-type GaAs material [12]. After that, a lot of experimental and theoretical work was done to explain the origin and behavior of these oscillations. The common agreement was in favor of negative differential mobility as the reasonable explanation for the oscillations. The mechanism to explain this was the field-induced transfer of the electrons from the high mobility conduction band valley to the low mobility satellite valleys.

After its discovery in 1963, the Gunn diode became the most important microwave device and is extensively used as a local oscillator and power amplifier in the frequency range from 1 to 300GHz [5].

### 1.4. Gunn Oscillations Formation

The concept of the Gunn oscillations and the domain formation is demonstrated in Figure 1.5. The whole process of domain formation starts with a dipole, which consists of the region of negative volume charge and positive volume charge.

There are many possibilities for this dipole to appear, such as doping inhomogeneity, structure defects, or random noise. Let's consider the sample of some length $L$ with an electric field applied to this sample. In a uniform sample, the electric field distribution along the sample is the same. However, if the sample has some local nonuniformity with higher resistance, the electric field in that place of the sample will be a little bit higher (see Figure 1.5b). This means that the critical electric field ( $\mathscr{E}_T$) will appear at that place in the sample first of all. As soon as the field at that local nonuniformity reaches the $\mathscr{E}_T$, the electrons will start to transfer to the satellite valley. In that satellite valley with higher electric field, heavy electrons will appear. The mobility in that valley of electrons will decrease in comparison to the lower valley because of the larger effective mass. This will result in increasing resistance ($R=1/en\mu$). Consequently, the electric field in that part of the sample will be raised, resulting in more intensive electron transitions to the high valley. Because the voltage across the sample does not change, the local electric field intensity on the left and on the right of that area will be decreased.

Where the dipole grows, the electric field at that location starts to increase because of the field near the dipole. However, the field inside of the dipole remains always above $\mathscr{E}_0$. The carriers' velocity of that dipole decreases as the field decreases and the electric field outside the domain is always smaller than $\mathscr{E}_0$. With increasing of the field, the carriers' velocity goes up and reaches the peak value.

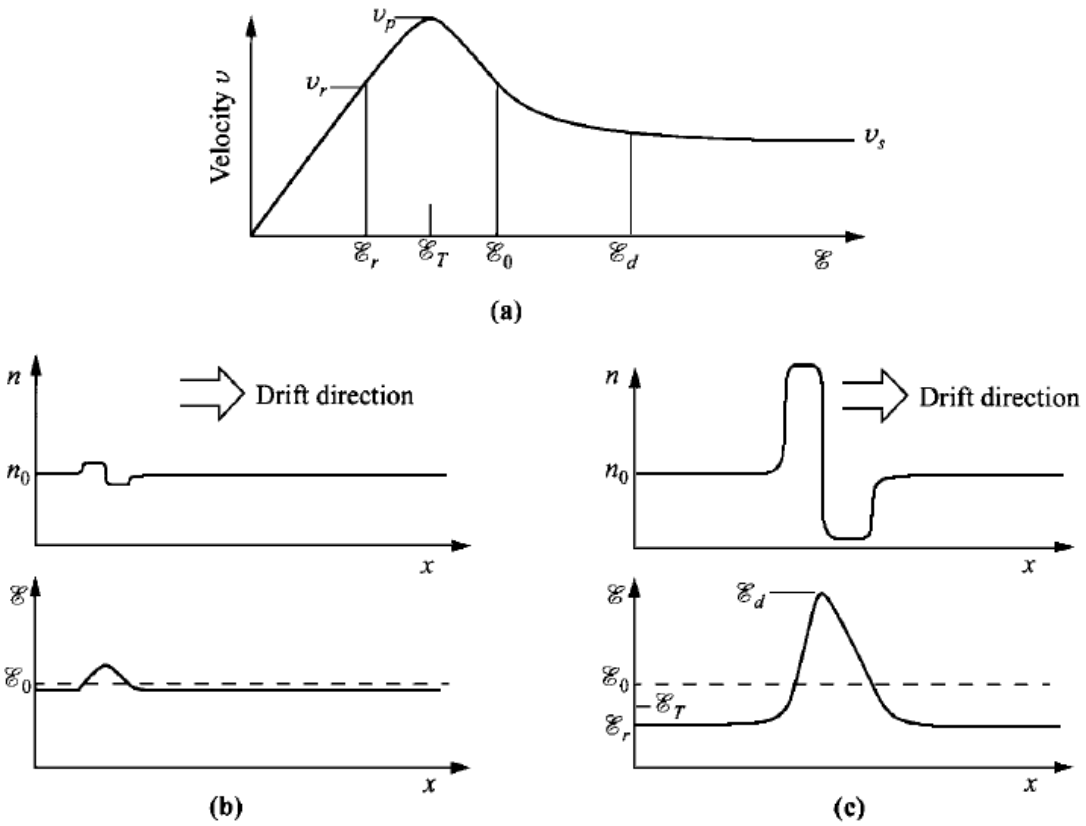


Figure 1.5. The process of domain formation: (a) typical *v*-*E* electrons behavior to achieve NDR and some relevant important points, (b) a small dipole formation, (c) a mature domain [5].

After the peak value is reached, the carrier velocity decreases because of the field decrease. The field outside the dipole will continue to decrease until it reaches some value, where the velocity of electrons inside and outside the dipole becomes the same (see Figure 1.5c). After that, it can be said that the dipole was transferred to the domain. Typically the domain forms near the cathode and moves from the cathode to the anode [6].

When the domain reaches the anode, the region of high field moves out of the sample and the current starts to increase. As soon as the current reaches the current that corresponds to the threshold voltage, the new domain will be formed and the current drops. As a result of the domain transition along the crystal under the external field, the pulse of current will be created.

The frequency of current impulses is determined by the time of the domain transition. For example, for a 50 μm long sample the frequency of current oscillations will be around 2 GHz.

Despite the fact that the crystal might have a few inhomogeneities, which can cause the domain formation, only one domain can exist in the crystal. In other words, the domain formation appears only on one inhomogeneity. After one domain will disappear a new domain can appear on some other inhomogeneity. Different positions of inhomogeneities in the crystal determine different periods of oscillations. Therefore, to achieve the Gunn effect, crystals of very high quality are needed. Also, it is very important that the distance between the minimum of the lowest valley and the satellite valley is not very large, as a high intensity electric field is needed to transfer electrons to the satellite valley.

## Chapter 2. Theory of Quantum Well Heterostructures with Remote Doping

Nowadays it is extremely difficult to imagine solid state physics without different types of semiconductor heterostructures such as quantum wells, quantum wires, and quantum dots. The conductivity of these semiconductor heterostructures can be controlled by adding dopants and other specific impurities. The dopants can be added precisely and placed as needed. Heterostructures with remote doping (doping that was introduced to the system far from the quantum well in order to reduce scattering on impurities) have attracted much attention because of their advantages, such as, high electron mobility and electron drift velocity due to reduced scattering on ionized impurities, intense photoluminescence, low noise, etc. [13]. One of the growth techniques which allows realization of extraordinary quality of the low-dimensional heterostructures is molecular-beam epitaxy.

### 2.1. Principles of Molecular Beam Epitaxy Growth

Molecular Beam Epitaxy (MBE) is a technique that takes place in ultra-high vacuum ($10^{-9}$ mbar) and allows epitaxial growth of thin films by combining different atomic beams directed to a heated substrate inside of the chamber [14]. In other words, MBE is a technique that allows the creation of new crystal structures on specific substrates (in most cases GaAs or Si) by depositing layers of atoms on top of single crystalline substrates with very high precision. In Figure 2.1, a schematic view of the MBE chamber is shown.

To monitor the growth of crystalline layers Reflection High Energy Electrons Diffraction (RHEED) is used. The thickness of each individual layer can be precisely controlled by means of closing and opening shutters in front of each effusion cell. By using this type of control, structures of different complexity, such as quantum wells, wires, or dots, can be created. These structures are very important elements for modern semiconductor devices.

In order to build one atomic layer on the substrate, beams of atoms or molecules have to be directed on the substrate. Depending on the structure of the crystal, different effusion cells are needed. The temperatures of the effusion cells are measured by thermocouples and can be precisely controlled with PID controller. The temperature of the substrate is measured by a thermocouple and/or calibrated infrared optical pyrometer.

Those atoms or molecules that were landed on the substrate which acts as a seed crystal (a single crystal based on which a large crystal of the same material will be grown) start to condense and as a result – build very thin layer of the desired crystal.

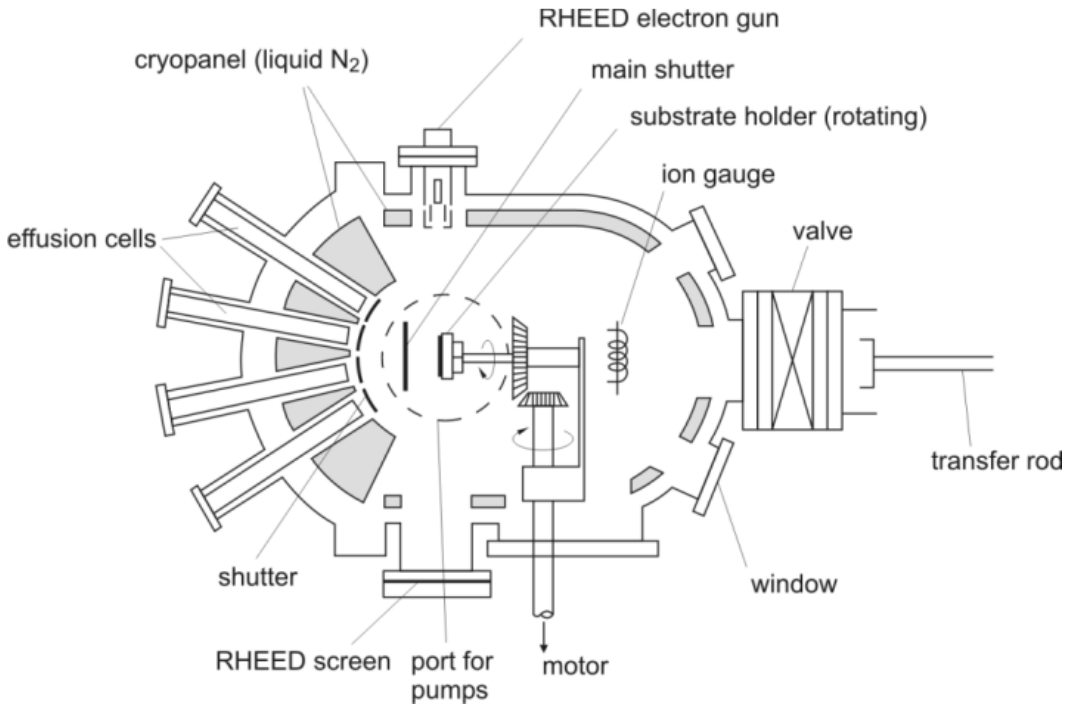


Figure 2.1. Schematic view of the MBE chamber for III-V semiconductor layers [15].

The MBE technique allows growth of one layer of atoms at a time. To control crystal growth the RHEED (Reflection High Energy Electron Diffraction) technique is usually used. By using an electron gun, which has a very well-focused electron beam, it is possible to penetrate into the surface of the substrate at different angles. The diffractive beam pattern can be seen on

the RHEED fluorescent screen. In Figure 2.2 a typical view of a pattern on a RHEED screen is shown.

When the composition of a crystal that has to be grown is the same as the substrate than the process of film deposition is called homoepitaxy. However, if the structure of the crystal is different from the substrate on which the crystal will be grown than the process in this case is called heteroepitaxy.

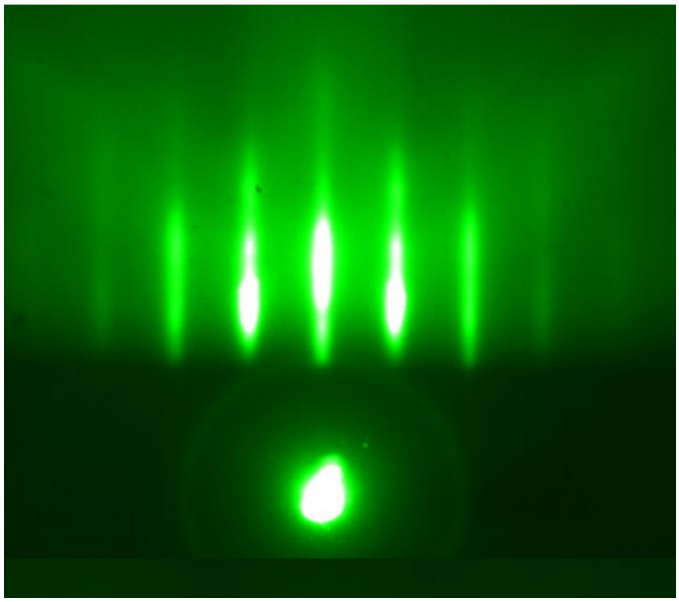

Figure 2.2. Typical view of RHEED screen while growing a crystalline material on top of GaAs [16].

## 2.2. Theory of Quantum Well Heterostructures (QWHs)

### 2.2.1. Theory of Heterostructures

To create a heterostructure between two different semiconductors, which must have different bandgaps, a contact of these semiconductors has to be made. For that reason, one semiconductor material should be grown on top of another using the MBE technique. Those two semiconductors have different physical properties that define the heterostructure as new artificial system. Lattice constant, doping concentration, and energy gaps are the most important properties of the heterostructure [17].

There are three main types of heterostructures which are presented in Figure 2.3. The most widely used type of heterostructures is type I that can be formed by combining AlGaAs material with a larger bandgap and GaAs material with a smaller bandgap (see Figure 2.3a). For this type of heterostructure, energy bandgap can be calculated using the equation

$$\Delta E_g = \Delta E_c + \Delta E_v, \tag{2.1}$$

where $\Delta E_c$ and $\Delta E_v$ are conduction and valance band energies, respectively.

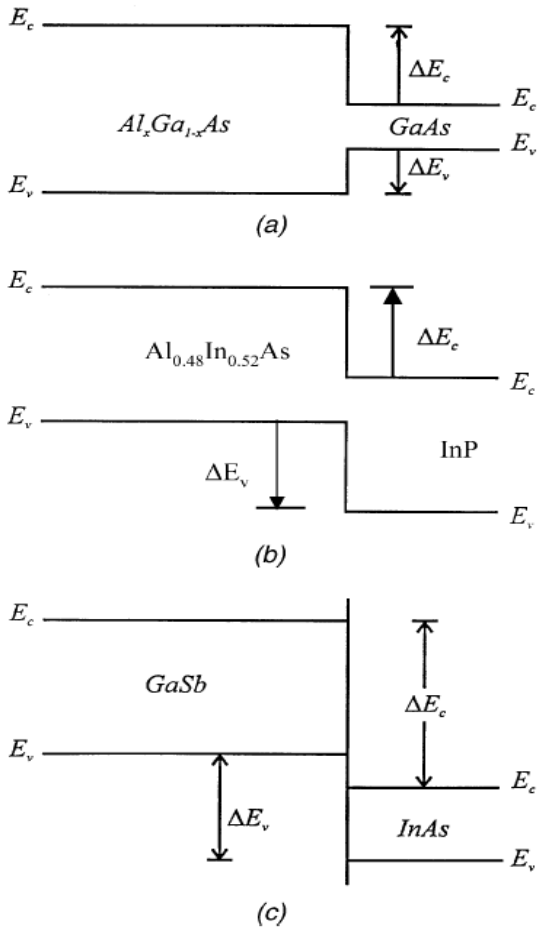


Figure 2.3.The main types of heterostructures: (a) – type I; (b) – type II; (c) – type III [17].

In type II heterostructures, the bandgap can be measured as the difference between conduction and valence bands energies of the materials that were used to form this

heterostructure. In Figure 2.3b, a type II heterostructure was formed using $Al_{0.48}In_{0.52}As$ and InP materials.

For type III heterostructures, the bottom of the conduction band of one material lies lower than the top of the valence band of another material. An example of a type III heterostructure can be seen in Figure 2.3c, where *GaSb* and *InAs* were used as combining materials.

To form a new heterostructure two cases can be used: (1) two intrinsic materials, one of which will be deposited one on top of another, or (2) add dopants into one or both materials in order to create p- or n-type. Using a second variant (p-n, p-p, n-n, etc.) junctions can be formed.

2.2.2. QWHs Advantages

Quantum wells (QWs) have a lot of advantages over other structures. First of all, the thickness of semiconductor that has to be placed between two other semiconductors in order to create a quantum well. The typical quantum well thickness is on the order of 10 nanometers. Due to the difference in bandgaps of those semiconductors, effective masses of electrons which are in the conduction band, as well as positively charged holes in the valence band are different from free electron mass [18]. Because of the very small size of the QW, electron and hole energy levels will be quantized and, as a result, the bandgap energy will be larger compared to bulk semiconductor materials.

Another advantage of QWs is that quantum well heterostructures have a great influence on carriers' propagation within some limits, and have inefficient influence on light because of large wavelength of light in compare to QWH thickness [19]. Based on those properties, quantum well waveguides can be created taking into consideration that carriers will not be influenced by the QW and for light a new guiding layer has to be grown. This is why scattering and reflection losses in the waveguides created using QWs can be very small.

2.2.3. Mechanisms of QWHs Formation

The combination of many heterojunctions forms a heterostructure. For example, if to get two types of materials, with different bandgaps, it will be possible to create a quantum well heterostructure using the MBE technique. Let us assume that $E_{gap}(A)$ is the bandgap of material A, which is smaller in comparison to $E_{gap}(B)$, the bandgap of the material B. If material A is placed between two sections of material B (see Figure 2.4a) the quantum well heterostructure will be achieved [20].

In the case when extra semiconductor layers will be included to form the heterostructure, such as when the new alloy say $A_{0.5}B_{0.5}$will be grown between *A* and *B* materials, a new type of the quantum well named stepped quantum well will be formed (see Figure 2.4b).

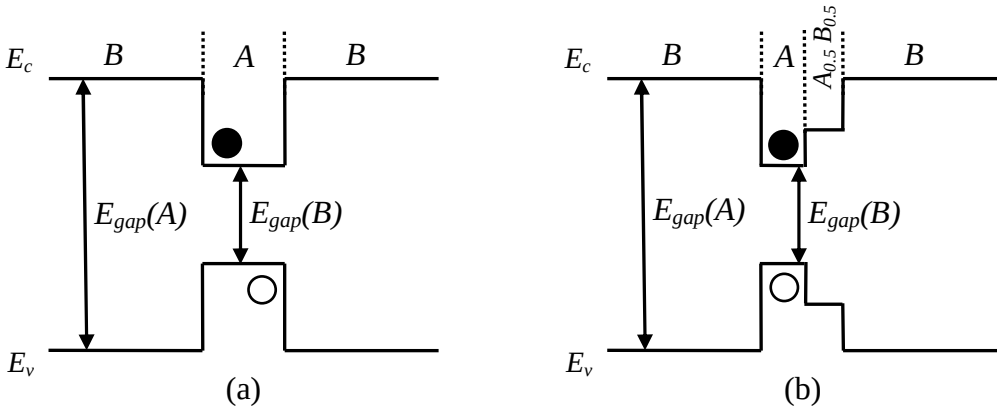


Figure 2.4. Bandgap diagrams for (a) single quantum well and (b) stepped quantum well [20].

For the quantum well systems that are shown in the Figure 2.4, any charge carriers present in those systems as a result of external excitations (for example, optical excitations) or by introducing dopants, will tend to move to the lowest energy in that system [21]. So any electron (solid black circle) or hole (open circles) will be confined in the quantum well.

In Figure 2.4 it can be seen that the structure of the stepped quantum well is more complicated to create, compared to a single quantum well. Furthermore, by using MBE

techniques even more complicated structures can be formed, such as asymmetric double quantum wells or multiple quantum wells can be formed used to form superlattices. By growing more complicated structures it is possible to modify the electronic and optical properties of those materials for application in some particular devices.

### 2.3. Applications of QWHs

The importance of QWHs is in their usability and wide range of applications in electronic and optoelectronic devices. Using technologies that are currently available and applying them to QWHs, a variety of advanced electronic devices that show major advantages of heterostructures can be created, such as: mid-infrared QW heterostructure lasers [8, 9], high-efficiency QW heterostructure LEDs [24], QW solar cells [25], bipolar transistors based on heterostructures [9, 10]. QWHs can also be used as part of electronic devices such as heterojunction based bipolar transistor, resonant tunneling devices, modulation-doped FET, and as an optical component in waveguides, microresonators, mirrors, etc. [18].

The systems that mainly use heterostructure based electronics have very broad areas of application and continued growth. It is hard to imagine today's life without telecommunications, fast internet connections, cell phones, satellite television systems, and other professional and recreational consumer products. For example, DH lasers can be found at almost every home as a component of CD, DVD, and Blu-ray disc players. Heterostructure based solar cell devices are widely used in different global and space oriented programs.

In conclusion, there are research and different investigations that can be done in the area of semiconductor physics in order to find better and more efficient ways to make and use QWHs, and also to understand their behavior in some specific conditions. All of that is because of the idea to use newly created QWHs more effectively and build new unique devices.

## Chapter 3. MBE Growth and Hall Effect Measurements

In this chapter the transport properties of MBE grown structures are discussed. Hall Effect measurements were performed, and the experimental results are discussed in order to explain different scattering mechanisms that are present in AlGaAs/GaAs quantum well heterostructures. The theory of the Hall Effect and of the main scattering mechanisms are briefly explained to give a better understanding of experimental results. Five different samples were analyzed and their results were compared. Two of the samples were used as references ($REF_U$ and $REF_\delta$) and the three other samples ($E_{1.0}$, $E_{0.8}$, and $E_{0.5}$) with different doping concentrations were used as a comparison to the reference samples.

### 3.1. AlGaAs/GaAs QW Heterostructure Growth

Using MBE technique five samples with different doping concentration were grown. The AlGaAs reference samples were grown using the structures shown in Figure 3.1 and Figure 3.2.

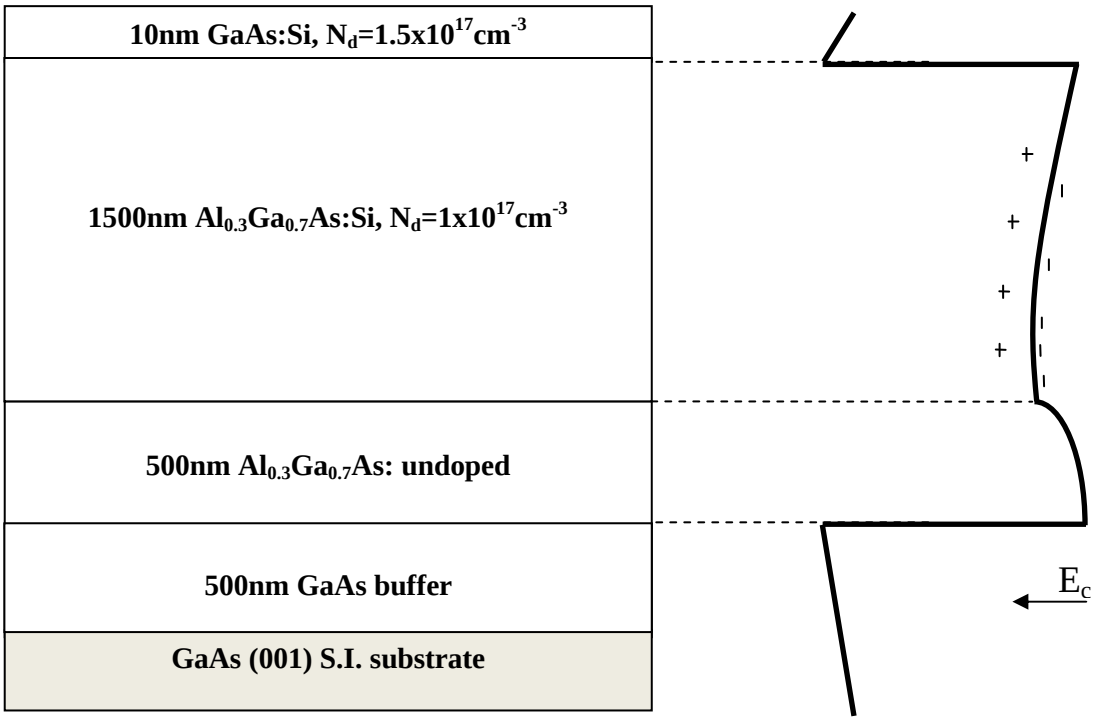


Figure 3.1.Schematic diagram of $Al_{0.3}Ga_{0.7}As$ epilayer uniformly doped by Si: growth (left), and its corresponding conduction band diagram (right) ($REF_U$ sample).

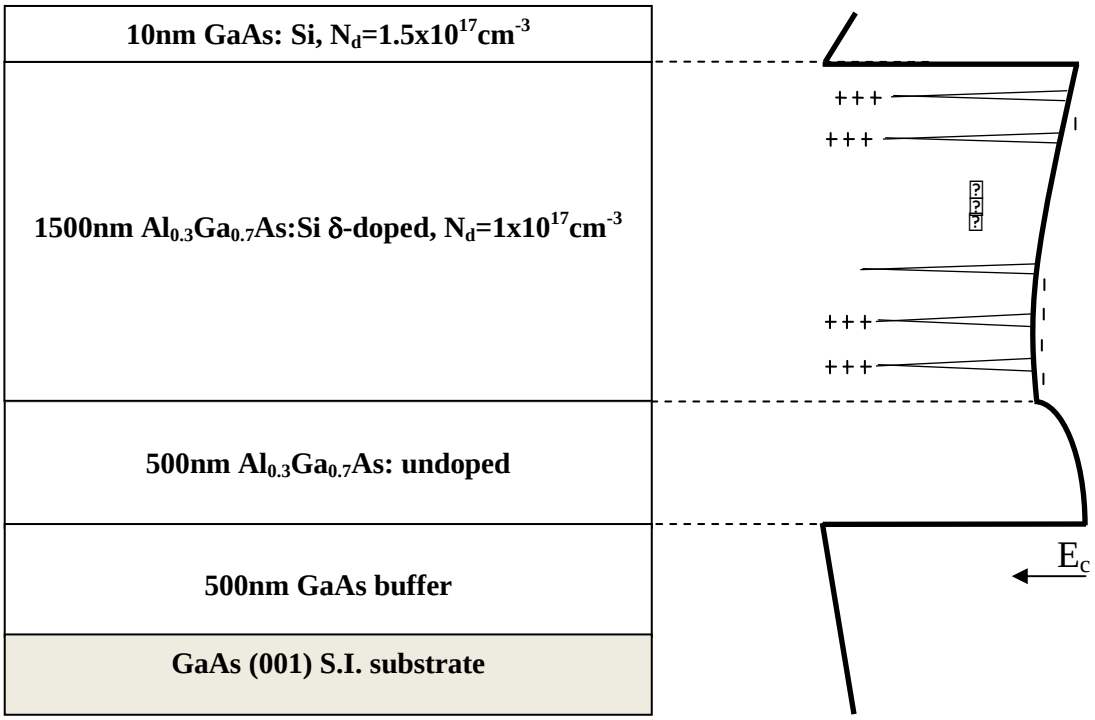


Figure 3.2. Schematic diagram of $Al_{0.3}Ga_{0.7}As$ epilayer with multiple Si δ-dopants growth (left), and its corresponding conduction band diagram (right) ($REF_\delta$ sample).

All samples were grown on a semi-insulating GaAs (100) substrate. The oxide layer on the substrate was removed by heating it to 610ºC with a constant background arsenic flux. After the oxide layer was removed, a 500nm thick GaAs buffer layer was grown to achieve high-quality epitaxial layers. The next layer was a 500 nm thick undoped layer of $Al_{0.3}Ga_{0.7}As$ to prevent the carrier transfer from the $Al_{0.3}Ga_{0.7}As$ with Si dopants into the GaAs buffer layer and to create the 2DEG gas at AlGaAs/GaAs interface. Then, 1500 nm of $Al_{0.3}Ga_{0.7}As$ doped with Si was grown with a doping level of 1x10$^{17}$ cm$^{-3}$ (see Table 3.1). For the $REF_U$ reference sample, the dopant in the AlGaAs layer was uniformly distributed. In reference sample $REF_\delta$, multiple layers of Si δ-dopants (in this case 20 of them) were deposited to achieve the same total doping concentration of $N_d$=1x10$^{17}$cm$^{-3}$, as in $REF_U$ sample. At the end of growth, the total structure was capped by GaAs doped with Si to ensure good ohmic contact for electrical measurements.

Also, this last layer is to prevent the oxidation of the $Al_{0.3}Ga_{0.7}As$ layer.

The quantum well heterostructures were grown as shown in Figure 3.3, and corresponding structure of preparation layer that was depicted in Figure 3.3 is shown in Figure 3.4. The oxide layer from the substrate was removed by heating the GaAs substrate up to 610ºC with a constant background arsenic flux. Then a buffer layer of 200nm was grown to achieve the high-quality growth. Then 20 periods of alternating 2 nm AlGaAs, 2 nm GaAs layers were grown to form a superlattice. This is necessary to reduce dislocations that might come from the GaAs substrate. Next, a 300 nm GaAs buffer layer was grown to achieve a very high-quality structure. After that, a 35 nm $Al_{0.4}Ga_{0.6}As$ layer was grown to prevent the formation of a two-dimensional electron gas at the AlGaAs/GaAs interface from the substrate side. The next layer was a 35 nm thick $Al_{0.3}Ga_{0.7}As$ layer with Si δ-doping, with theδ-doping introduced after the growth of a 30 nm of $Al_{0.3}Ga_{0.7}As$. After that, a 5 nm $Al_{0.3}Ga_{0.7}As$ spacer layer was grown. In order to form the quantum well, 10 nm of GaAs was grown. Then, a 35 nm thick $Al_{0.3}Ga_{0.7}As$ barrier with Si δ-doping was grown. For the cap layer, 5 nm of GaAs uniformly doped with Si ($N_d=2x10^{18}cm^{-3}$) was grown.

The main characteristics and dopant concentrations for the samples are presented in Table 3.1. A note: $N_d\ [cm^{-2}]= N_d\ [cm^{-3}]\cdot d$, where d is the thickness of the material that was grown.

Table.3.1. The main parameters of samples that were grown by MBE and used in further measurements.

| **Lab Sample Name** | **Doping concentration, $N_d$** | **Doping Type** |
|---|---|---|
| $REF_U$ | $1x10^{17}\ cm^{-3}$ | Uniform |
| $REF_\Delta$ | $1x10^{17}\ cm^{-3}$ | Multiple δ-dopants |
| $E_{1.0}$ | $1x10^{12}\ cm^{-2}$ | δ-dopant |
| $E_{0.8}$ | $8x10^{11}\ cm^{-2}$ | δ-dopant |
| $E_{0.5}$ | $5x10^{11}\ cm^{-2}$ | δ-dopant |

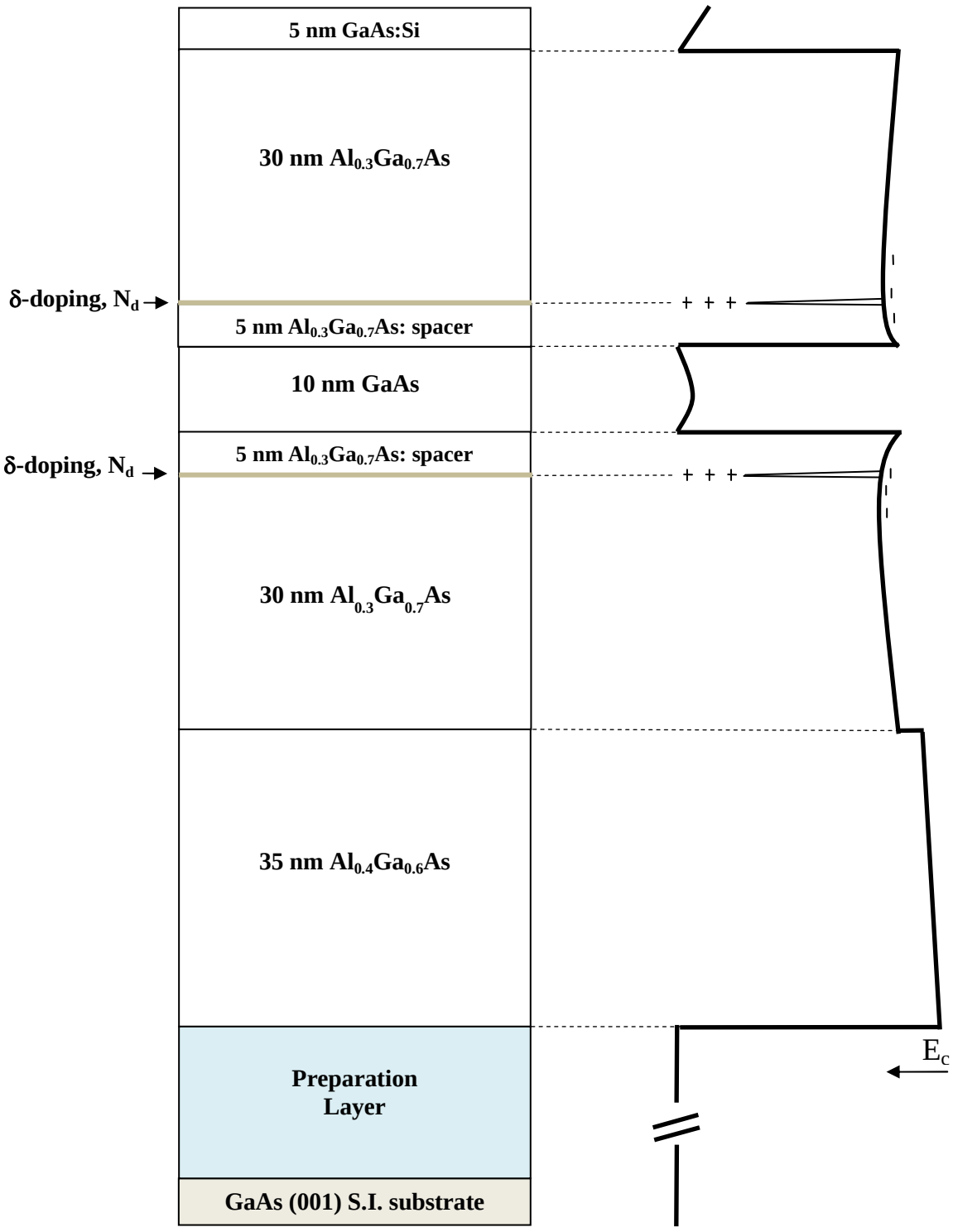


Figure 3.3. Schematic diagram of the GaAs quantum well heterostructure with Si δ-dopants in $Al_{0.3}Ga_{0.7}As$ barriers (left). The corresponding schematic diagram of the conduction band is shown (right). The growth conditions were kept the same for all samples $E_{1.0}$, $E_{0.8}$, $E_{0.5}$. The difference was only the doping level as it is shown in Table 3.1.

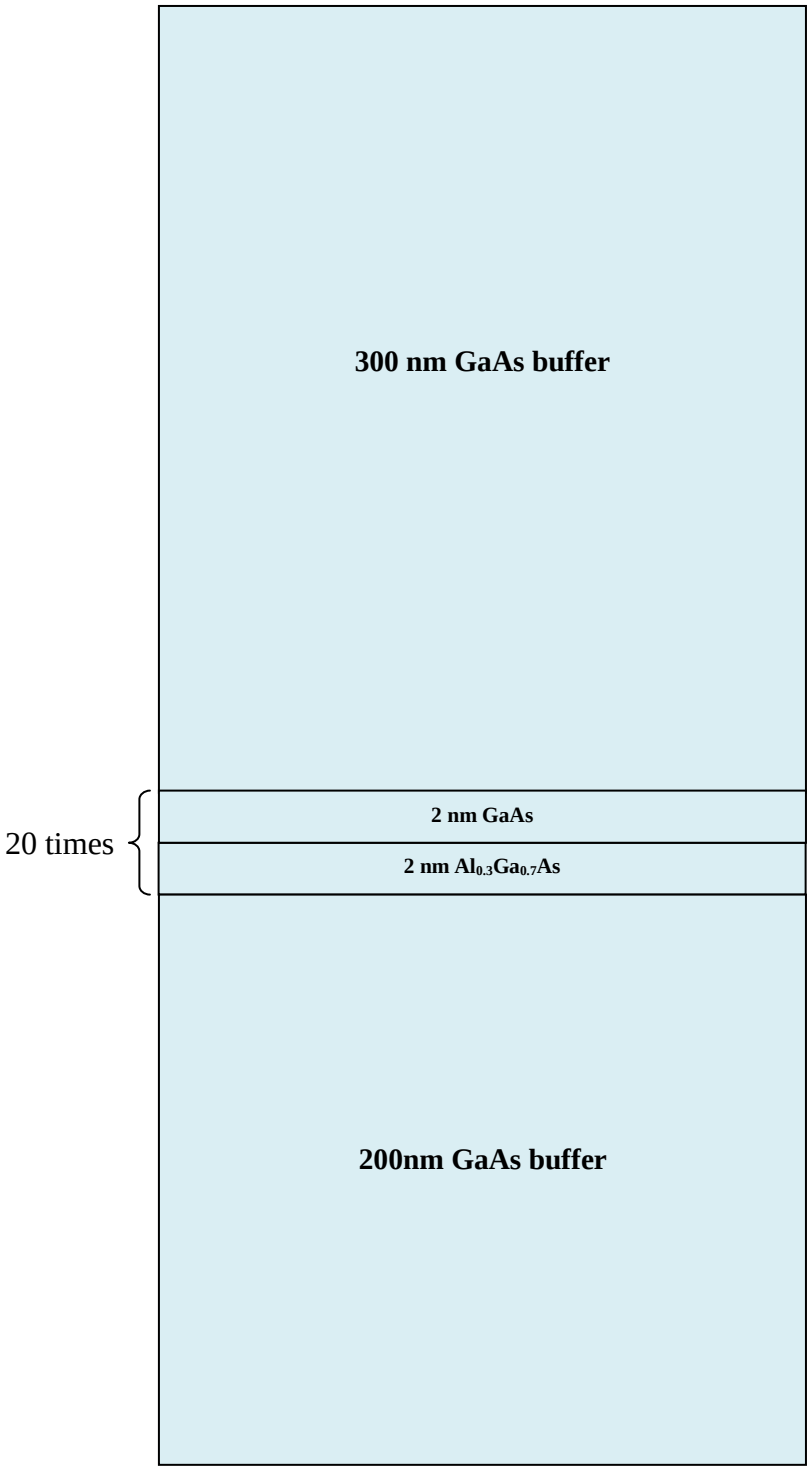


Figure 3.4. Schematic diagram of the preparation layer for the structure of the GaAs quantum well heterostructure with Si δ-dopants in $Al_{0.3}Ga_{0.7}As$ barriers.

It is worth to mention that the conduction for all these samples takes place in lateral surface, but not in vertical one. The example of current flow for the simple QW heterostructure, which was grown by MBE, is depicted in Figure 3.5.

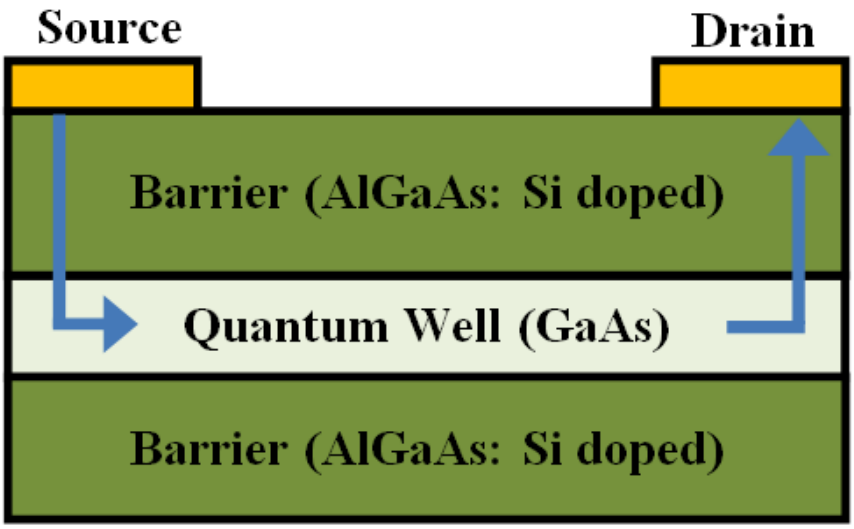


Figure 3.5. The simple quantum well heterostructure grown by MBE with ohmic contacts on top.

### 3.2. Mobility in Semiconductors

In semiconductors at room temperature (~300K), electrons can randomly move in any direction with the velocity of about $10^7$ cm/s. This random motion of electrons results in a zero net displacement of the electron for a very long period of time. However, when some electric field $E$ is applied to the sample, each electron will be influenced by the force $-eE$ and will be accelerated. So an additional velocity component, which is called drift velocity, will be introduced along with the thermal movement of electrons.

The momentum that the electron gained $m_n \upsilon_n$ and the momentum that was applied to the electron $-eE\tau_c$, the drift velocity $\upsilon_n$ can be calculated as

$$\upsilon_n = -\frac{e\tau_c}{m_n}E\,, \tag{3.1}$$

where $\tau_c$ is the mean free time (the average time between collisions), $e$ is the electron charge constant, and $m_n$ is the mass of the electron.

It can be seen from Equation (3.1) that the electron drift velocity $\upsilon_n$ is proportionally dependent to the applied electric field $E$ and some factor $e\tau_c/m_n$. This factor is called electron mobility $\mu_n$ and is expressed as

$$\mu_n = \frac{e\tau_c}{m_n}. \tag{3.2}$$

Using Equations (3.1) and (3.2), the electron drift velocity $\upsilon_n$ is given as

$$\upsilon_n = -\mu_n E\,. \tag{3.3}$$

The expression of mobility in Equation (3.3) provides information about how strongly the motion of the electron depends on the applied electric field.

The most convenient way to measure the mobility and some other semiconductor characteristics (density, resistivity, etc.) is to perform the Hall effect measurement.

### 3.3. Hall Effect Measurements

In order to measure the main parameters of the semiconductor materials, the Hall effect measurement technique can be applied. In Figure 3.6, the simple semiconductor plate-like device that is suitable for this type of analysis is shown.

With applying the electric field $E$, the current $I$ will flow through this sample. The density of this current $J$ is given as

$$J = -en\upsilon = \sigma E\,, \tag{3.4}$$

where $e$ is the electron charge, $n$ is the carrier density, $\upsilon$ is the velocity of the electrons, and $\sigma$ is the conductivity of this sample.

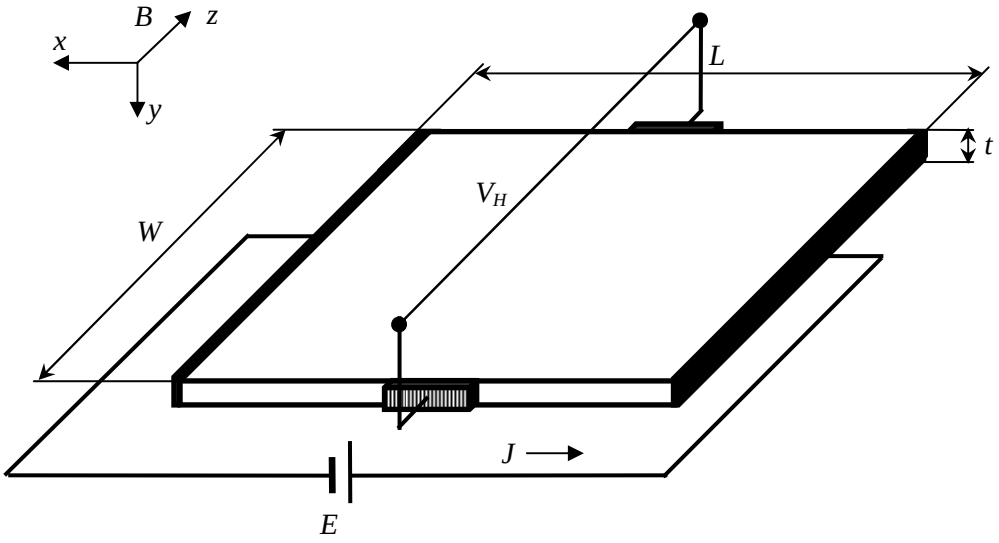


Figure 3.6. The sample of the special dimensionality to measure the Hall effect.

If to assume that this is an n-type sample, each electron will be influenced by electric force $\vec{F}_e$, which can be written as

$$\vec{F}_e = -e\vec{E}. \tag{3.5}$$

The minus sign in Equation (3.5) means that the electrons will move along the direction opposite to the direction of the electric force.

If this sample is exposed to a perpendicular magnetic field, all the electrons that move in the direction of current flow will be influenced by Lorentz force $\vec{F}_L$, which is given as

$$\vec{F}_L = e\left[\vec{\upsilon} \times \vec{B}\right], \tag{3.6}$$

where $\vec{B}$ is the magnetic induction.

The Lorentz force will tend to push the moving electrons in the direction of the force. As a result, the excess negative charges will move to one side of the semiconductor, while positive charges move to the opposite side. Due to this charge imbalance, an electric field $\vec{E}_H$ will appear and corresponding force $\vec{F}_H$, which is called the Hall force, will tend to compensate the Lorentz force.

In order to compensate the Lorentz force $\vec{F}_L$, the Hall force $\vec{F}_H$ has to be equal to the Lorenz force $\vec{F}_L$ ($\vec{F}_H = \vec{F}_L$). So, using Equations (3.5) and (3.6), the Hall electric field can be expressed as

$$\vec{E}_H = \left[\vec{\upsilon} \times \vec{B}\right]. \tag{3.7}$$

If to consider Equation (3.4), the velocity of electrons υ will be given as $\vec{\upsilon} = -\frac{\vec{J}}{en}$. Hence, the Equation (3.7) in terms of the density of current can be rewritten as

$$\vec{E}_H = -\frac{1}{en}\left[\vec{J} \times \vec{B}\right]. \tag{3.8}$$

The Hall electric field is the field across the hall device with width *W*. Therefore, the Hall electric field $E_H$ in terms of the Hall voltage $V_H$ can be expressed as

$$E_H = \frac{V_H}{W}. \tag{3.9}$$

The density of current *J* in terms of the current *I* and sample dimensions is given as

$$J = \frac{I}{Wt}. \tag{3.10}$$

Using Equations (3.8) – (3.10), and taking into consideration that the magnetic field is perpendicular to the sample, the Hall voltage can be expressed as

$$V_H = -\frac{1}{en}\frac{IB}{t} = R\frac{IB}{t}, \tag{3.11}$$

where $R = -\frac{1}{en}$ is the Hall coefficient.

As it can be seen from the Equation (3.11), it is easy to calculate the carrier concentration *n.* The Hall voltage also can be expressed in terms of voltage V across the bias t contacts as

$$V_H = \mu\frac{W}{L}VB\,. \tag{3.12}$$

Equation (3.12) can be applied to calculate the mobility of the sample.

### 3.4. Scattering Mechanisms in AlGaAs/GaAs Structures

In the previous section, the Hall effect was discussed providing the possibility to measure the main parameters of the semiconductor samples. In the frame of this thesis, the main attention was to measure and characterize the mobility and the density of the carriers. However, in order to make a reasonable analysis and give some correct conclusions, understanding of scattering mechanisms was very important. Therefore, the main scattering mechanisms, which are present in AlGaAs/GaAs structures, were discussed.

In Figure 3.7 different scattering mechanisms for semiconductors are presented.

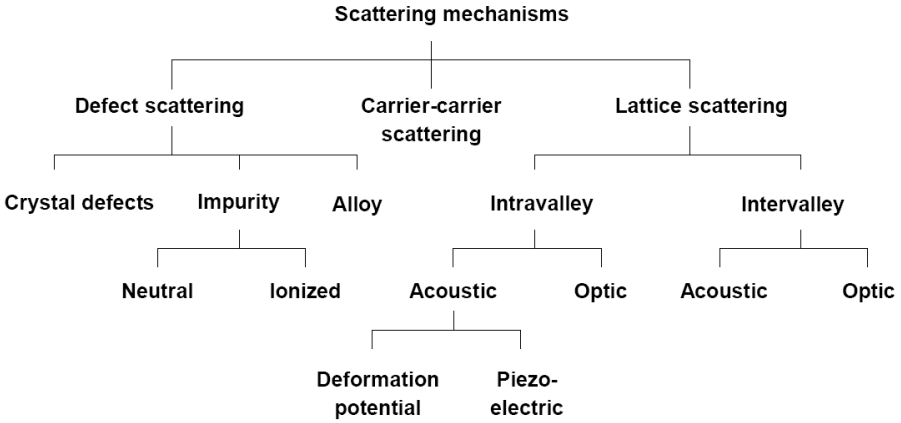


Figure 3.7. Different possible carrier scattering mechanisms in AlGaAs/GaAs structure [10].

The carrier-carrier scattering mechanisms were not considered because this type of carrier scattering is only important in materials with high carrier concentrations ($n>2x10^{18}cm^{-3}$).

### 3.5. Scattering in Bulk GaAs

By applying the Matthiessen's rule for all scattering mechanisms present in bulk GaAs sample, the total mobility can be presented as

$$\frac{1}{\mu} = \sum_i \frac{1}{\mu_i}, \tag{3.13}$$

where $\mu i$ corresponds to the specific scattering mechanism.

In order to calculate the total mobility for bulk GaAs, the most significant scattering mechanisms were discussed.

#### 3.5.1. Scattering on Ionized Impurities

Scattering on ionized impurities is an essential scattering mechanism in the bulk GaAs system. When a charge moves next to the ionized dopant impurity, this charge will be influenced by the Coulomb force. As a result of this interaction the direction of propagation, velocity, etc. can be changed. The probability of impurity scattering depends on the sum of the concentrations of negatively and positively charged ions.

Impurity scattering is more dominant at low temperatures. This is due to the fact that at high temperatures the carriers move faster in the semiconductor and, as a result, electrons have larger kinetic energy. Therefore they stay near the impurity atoms for a shorter period of time, which is not enough time to achieve sufficient scattering. However, at low temperatures the velocity of charge carriers decreases and they become more influenced by ionized impurities. This interaction results in a higher scattering processes and a decrease in mobility [5].

According to the theoretical analysis, variations in the mobility as a result of impurity scattering $\mu_i$ tend to be proportionally changed as $T^{3/2}/N_T$, where $N_T$ is the total impurity concentration.

3.5.2. Phonon or Lattice Scattering

Phonon scattering is another very important mechanism. The four main types of phonon scattering mechanisms were discussed for different conditions.

Phonon or lattice scattering is due to the thermal vibrations of lattice. At temperatures above absolute zero atoms in the crystal lattice will tend to be displaced from their original positions. However, because they are influenced by other atoms, the atoms will interact with each other causing some vibrations. Therefore, this mechanism of scattering is more dominant at high temperatures [26].

3.5.3. Acoustic Phonons Scattering: Deformation Potential

This type of scattering is due to the lattice deformation caused by phonons. The acoustic phonons cause changes in the lattice spacing, which changes the band gap from one point to another. Because of that, the crystal will be deformed and cause a deformation potential to be formed. The mobility dependence on temperature can be given as $n_{ac}/\upsilon$, where $n_{ac}$ is the density of acoustic phonons, and $\upsilon$ is the average electron velocity. The mobility contribution from this type of scattering mechanism is proportional to $T^{-3/2}$.

3.5.4. Acoustic Phonon Scattering: Piezoelectric Scattering

The atomic displacements produced by the acoustic phonons introduce a second potential if the atoms are partially ionized. This is called the piezoelectric effect and it occurs in crystals lacking a center of symmetry. The mobility change with temperature will have $T^{-1/2}$ behavior.

The summary of all available scattering mechanisms in GaAs sample and their influence on the mobility at different temperatures is depicted in Figure 3.7.

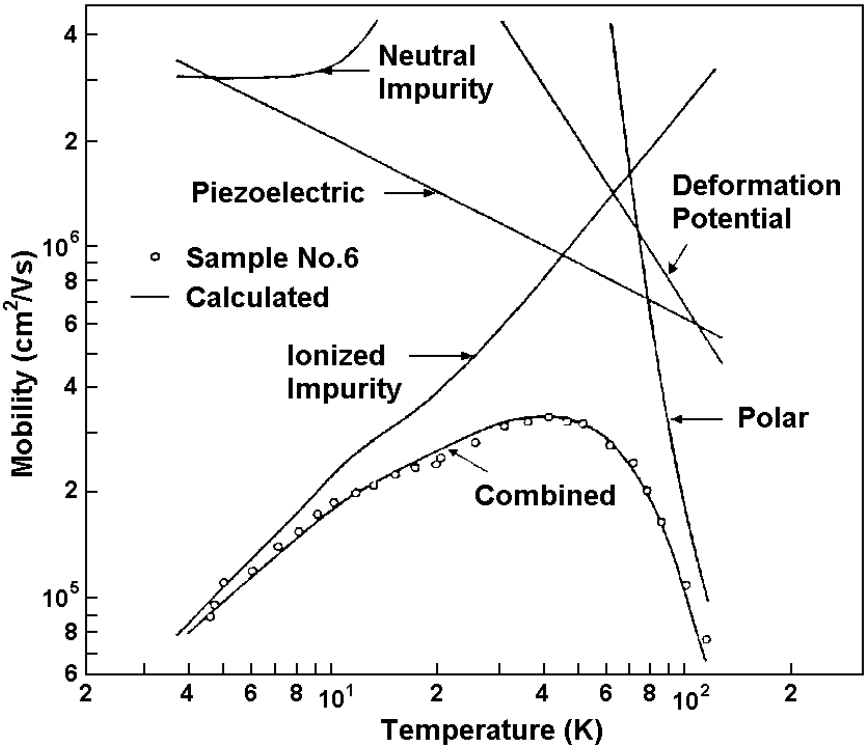


Figure 3.8. Different scattering mechanisms in GaAs sample and their influence on the mobility at different temperatures, where curves correspond to the calculated and circles to the measured mobility [28].

3.5.5. Optical Phonons Scattering: Polar Scattering

This type of scattering mechanism is dominant at 300 K in GaAs because of dipole moments that are formed due to the interaction of the ionic charges of the atoms with optical phonons. The resulting mobility varies with temperature as $T^{1/2}$[27].

## 3.6. Scattering in QW Heterostructures

When low band gap GaAs is placed between two AlGaAs layers with a larger band gap, a QW heterostructure will be created. In bulk GaAs the quantum size effects are negligible because the size of the electronic wave function is much smaller than any of the sample

dimensions. However, if the size of the material between the barriers is comparable to the de Broglie wavelength, given as

$$\lambda_{deB} = \frac{h}{p} = \frac{h}{\sqrt{2m^* E}}, \tag{3.14}$$

where $E$ is the kinetic energy of the electron, and $m^*$ is the effective mass of the electron, the quantum size effects start to play a very important role.

A typical example of the conduction band for the AlGaAs/GaAs interface is depicted in Figure 3.9, where the AlGaAs layer was remotely uniformly doped by Si atoms. Remote δ-doping means that a very thin layer of Si was grown to provide electrons for the quantum well. By using remote doping, the AlGaAs layer near the interface will be not doped and it corresponds to the spacer width in Figure 3.9.

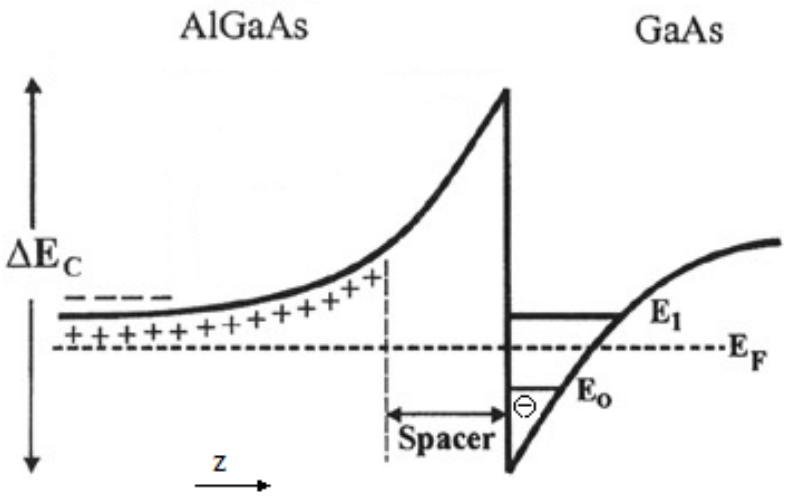


Figure 3.9. The schematic view of the conduction band diagram for AlGaAs/GaAs heterostructure junctions [29].

In Figure 3.9, it can be seen that the conduction band has a discontinuity of $\Delta E_c$ between the two materials. As a result, electrons will transfer from AlGaAs to the GaAs conduction band (lower electron energy). However, electrons created from ionized donors in AlGaAs that transfer

into GaAs will bend the conduction band of AlGaAs upward in the direction towards the interface. Because the electric field has to be continuous across the interface, the GaAs band will continue upward at the same slope. Furthermore, the GaAs band will gradually bend toward the horizontal because of the free electrons that were transferred from the AlGaAs. Hence, a roughly triangular well will be formed (see Figure 3.9). The electrons that are located in that triangular well will form a two-dimensional electron gas (2DEG). The motion in the z-direction, that corresponds to the direction of sample growth, is quantized; however, electrons are still free to move in the x- and y-directions [27]. As a result of these quantized movements, the scattering also occurs in two dimensions. Therefore, new scattering mechanisms that were not present in bulk GaAs arise due to the interface and remote impurities.

### 3.6.1. Scattering by Remote Ionized Impurities

The mechanism that was discussed earlier of scattering on ionized impurities can be applied to characterized scattering by remote ionized impurities if to take into consideration that ionized dopant impurities are situated at some distance from the 2DEG (see Figure 3.9). If the spacer in Figure 3.9 is very thin, scattering from remote ionized impurities can be significant.

The mobility increases as the third power of the distance between the 2DEG in the well and the doped layer [29]. Therefore, sometimes it is hard to say how scattering by remote ionized impurities depends on the temperature. However, if to consider the Coulomb interaction between ionized dopants and the 2DEG, it is reasonable to say that, even at some separation, those particles will interact. And because at low temperatures the kinetic energy of the electron is lower in comparison to higher temperatures, this Coulomb interaction will have a higher influence on electron scattering. The result of this interaction will lead to a decrease in the

mobility. Hence, it is reasonably to say that at low temperatures the mechanism of scattering by remote ionized impurities will start to dominate, and the mobility of electrons will decrease.

3.6.2. Scattering by Interface Roughness

The quantum well is formed as a combination of materials with different bandgaps. That is why interfaces between these materials have different degrees of roughness. In an ideal case, the interfaces should be sharp and have straight edges. However, in reality, there are fluctuations in the material thicknesses at the interfaces. The result of these fluctuations and interface roughness will cause the electrons to scatter.

In Figure 3.10 the schematic view of the interface roughness in AlGaAs/GaAs quantum well is depicted. The dotted line corresponds to the ideal QW interface.

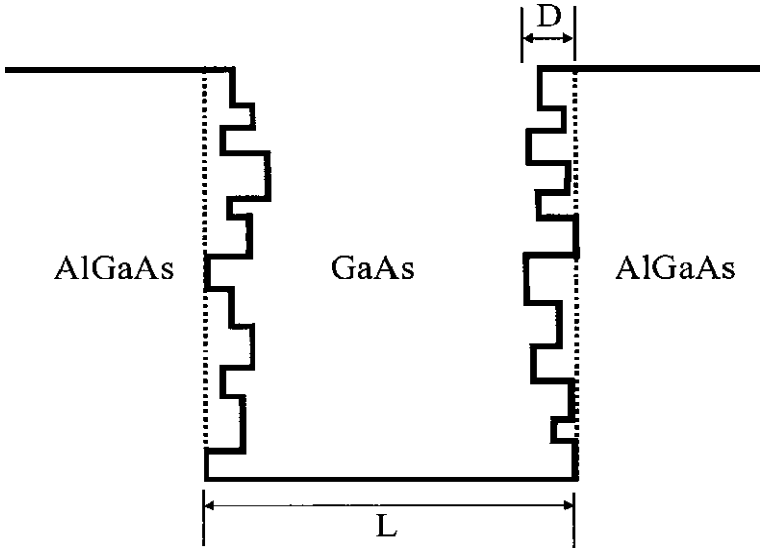


Figure 3.10.A schematic view of the AlGaAs/GaAs quantum well that shows variations of the well thickness, which is the source of the interface roughness [29].

Scattering by interface roughness in QW structures can dominate at low temperatures.

3.6.3. Alloy Scattering

In $Al_{0.3}Ga_{0.7}As$ semiconductor material, 30% of the Ga atoms are replaced by Al. However, these replacements occur in a random, disordered fashion, resulting in a non-periodic

potential. For a GaAs 2DEG, the electron wave function is almost entirely located in the crystalline GaAs and only a small tail of the exponential function goes into the AlGaAs.

The typical behavior of the electron mobility in semiconductors at different temperatures is depicted in Figure 3.11.

As it can be seen in Figure 3.11, the highest influence on electron mobility is scattering on phonons (or lattice vibrations) and ionized impurities, which are dominant at high and low temperatures, respectively.

From this point the experimentally achieved data for mobility and density at different temperatures were analyzed.

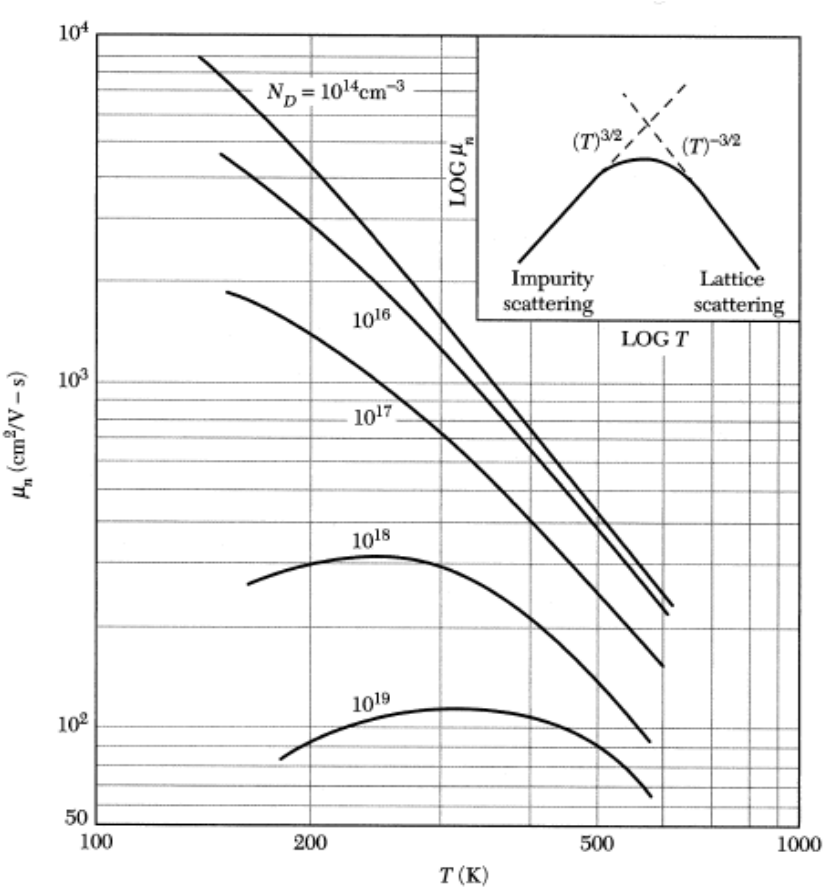


Figure 3.11. Typical electron mobility behavior of semiconductors at different temperatures for various dopants concentration. Insert presents the theoretical temperature dependence of electron mobility [5].

### 3.7. Experimental Mobility and Density Data Discussion

To study the mobility and density for all unpatterned experimental samples, the Hall Effect measurements were performed in the temperature range of 8 K to 300 K. The plot of temperature dependent measurements of the electron mobility and density for AlGaAs/GaAs samples with various Si dopants are depicted in Figures 3.12–3.16.

3.7.1. Mobility

In bulk GaAs semiconductors, charged impurities are very significant scattering centers. Hence, the large doping concentration results in lower mobility because of the reduced mean free path of the electrons through the semiconductor. This mobility will increase as the temperature goes up due to the increased thermal velocity (see Figures 3.12 and 3.13).

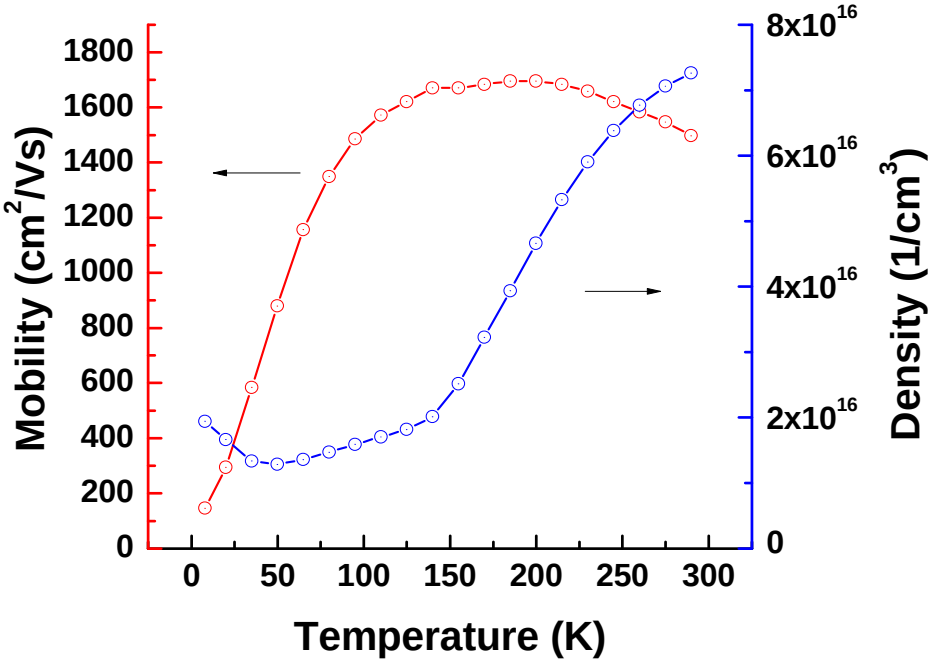


Figure 3.12. A plot of temperature dependent measurements of electron mobility and density for $Al_{0.3}Ga_{0.7}As$ sample doped Si uniformly ($REF_U$).

The difference in mobility for these reference samples is caused by higher scattering rate of electrons on ionized impurities in $REF_\delta$ sample with δ-doping than for uniformly doped $REF_U$

sample. That is why, when the doping concentration increases, the mobility decreases due to the ionized impurity scattering process that was discussed above.

As it was depicted in Figures 3.12 and 3.13, at high temperatures the absolute value of the mobility was limited because of phonon scattering. However, by lowering the temperature of the sample, this scattering mechanism became less significant and, as a result, the mobility of samples increased. At low temperatures scattering by ionized impurities started to dominate and mobility was mostly driven by impurity scattering.

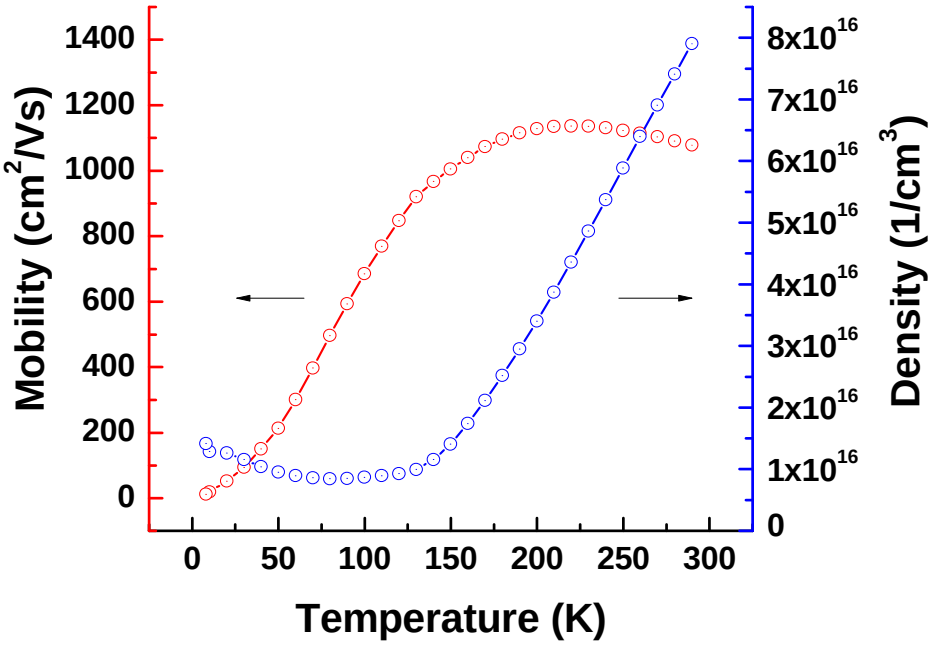


Figure 3.13. A plot of temperature dependent measurements of electron mobility and density for $Al_{0.3}Ga_{0.7}As$ sample with multiple Si δ-dopants ($REF_\delta$).

For both these referenced samples ($REF_U$ and $REF_\delta$) at room temperature the same carrier density was measured, as expected. As it is known from the previous chapter, the $REF_U$ sample was uniformly doped with Si dopants $N_d$=1x10$^{17}$cm$^{-3}$ and the $REF_\delta$ sample used Si δ-doping was used to achieve the same doping concentration $N_d$. However, the experimentally measured electron mobilities were different. The proposed explanation was that the measured difference in

mobility was because of the higher scattering rate of electrons on ionized impurities for δ-doped samples in comparison with the uniformly doped sample.

In QW heterostructures, because the two-dimensional electrons (2DEG) are separated from their parent ionized Si atoms, the process of scattering on ionized impurities at high and low temperatures can be significantly reduced. As a result, very high mobilities of the 2 DEG can be achieved [30]. As a proof of this concept, the experimental mobility data for QW heterostructures (shown in Figures 3.14–3.16) were much higher compared to the reference samples.

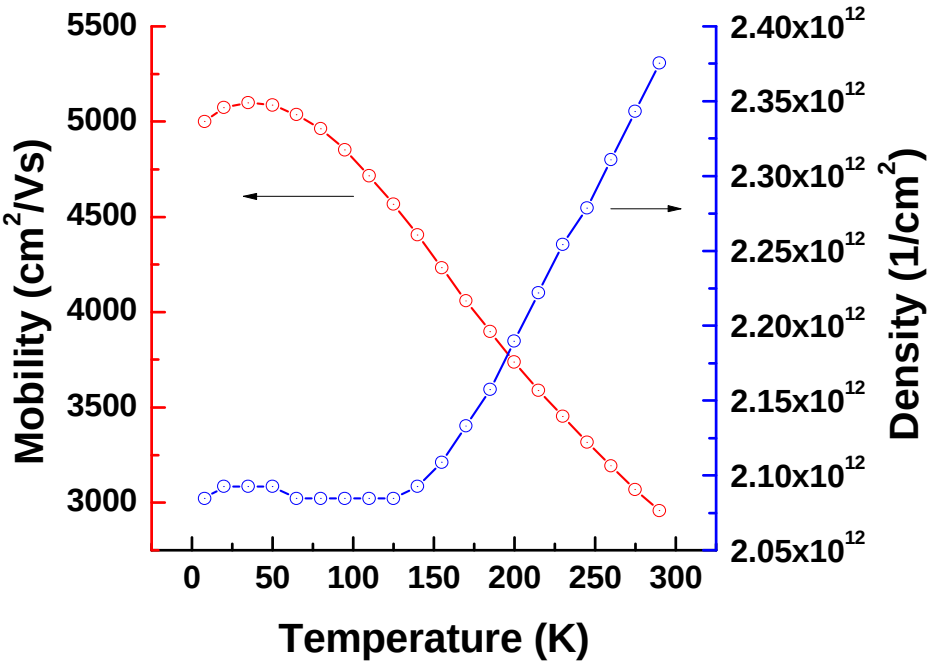


Figure 3.14. A plot of temperature dependent measurements of electron mobility and density for GaAs QW (sample $E_{1.0}$) with Si δ-dopants of $N_d=1x10^{12}cm^{-2}$ in AlGaAs barriers.

For temperatures higher than 60 K, the scattering in the 2DEG is dominated by polar optical phonon scattering.

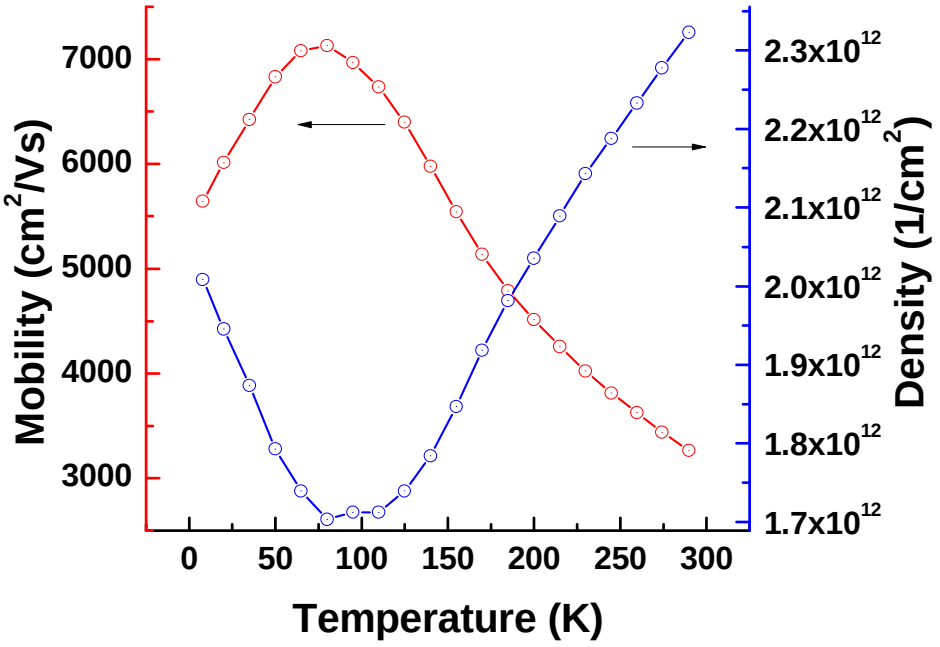


Figure 3.15. A plot of temperature dependent measurements of electron mobility and density for GaAs QW ($E_{0.8}$, $N_d$=8x10$^{11}$cm$^{-2}$).

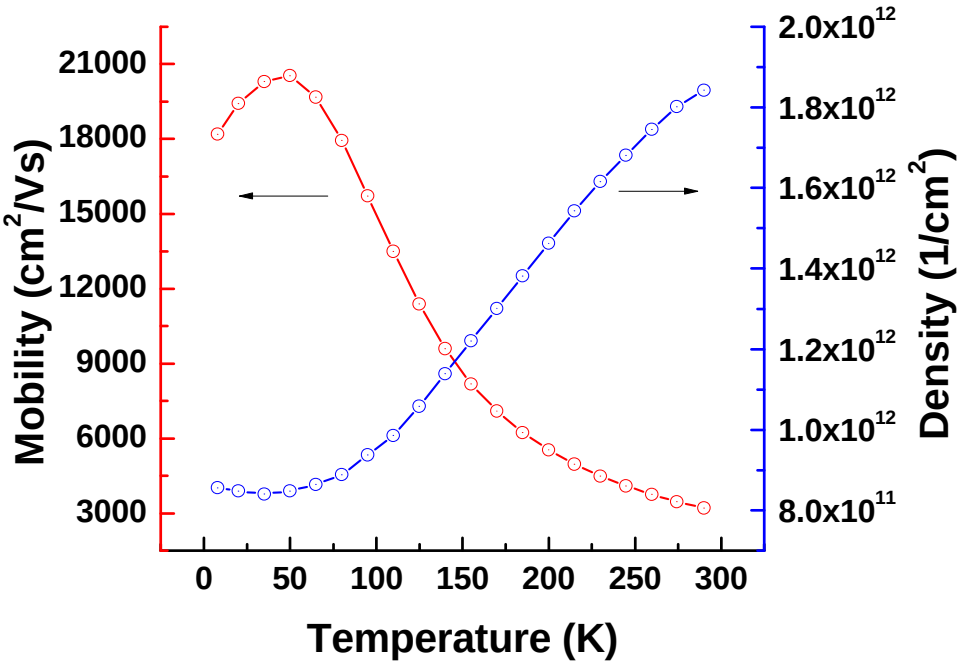


Figure 3.16.A plot of temperature dependent measurements of electron mobility and density for GaAs quantum well ($E_{0.5}$, $N_d$=5x10$^{11}$cm$^{-2}$).

At lower temperatures, other contributions to the 2DEG become important that cause the mobility to decrease. The most significant scattering mechanisms that influence the mobility at low temperatures are remote ionized impurity scattering and alloy scattering [30].

When considering the whole temperature range for the experimentally achieved data of the electron mobility depicted in Figure 3.17, at high temperatures the mobility was dominated by phonon scattering. However, when decreasing the temperature somewhere around 60 K the scattering on phonons started to be not as dominant as it was at high temperatures. Hence, the scattering on remote ionized impurities and alloy scattering start to dominate electron mobility.

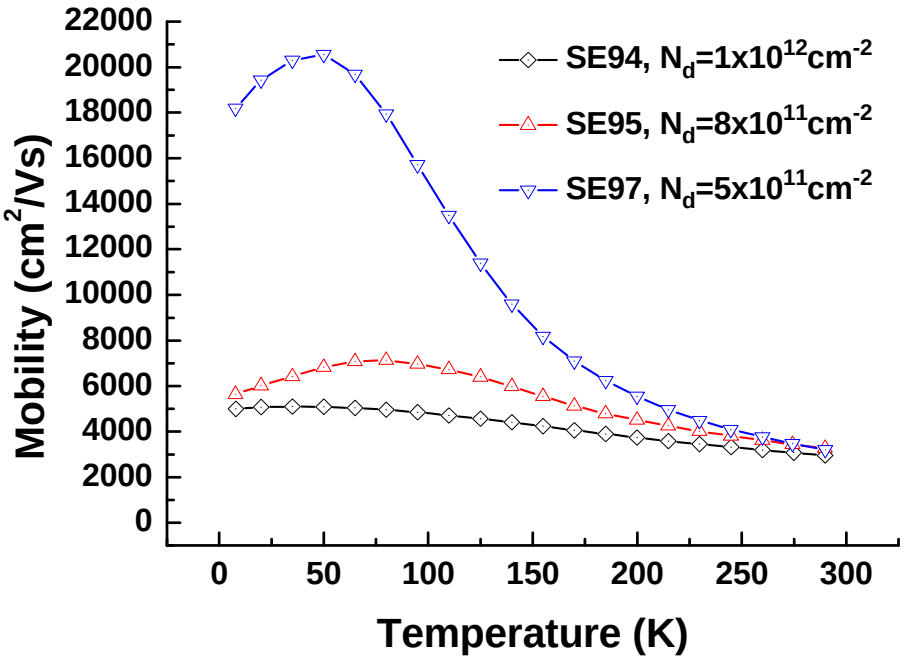


Figure 3.17. A plot of temperature dependent measurements of electron mobility for all GaAs quantum well samples ($E_{1.0}$, $E_{0.8}$, $E_{0.5}$ samples).

3.7.2. Carrier Concentration

As it was previously described, the carrier density in a remotely doped semiconductor equals to the net activated doping of the material at moderate temperatures and decreases with

temperature lowering because of the carrier freeze-out effect. At high temperatures, the carrier density increases, approaching the total doping of the material.

In Figure 3.18, a comparison of the electron density for all quantum well samples is depicted. At temperatures higher than 100 K, an increase of the carrier concentration with increasing temperature was measured. This increase occurred because more Si atoms became ionized with increasing temperature.

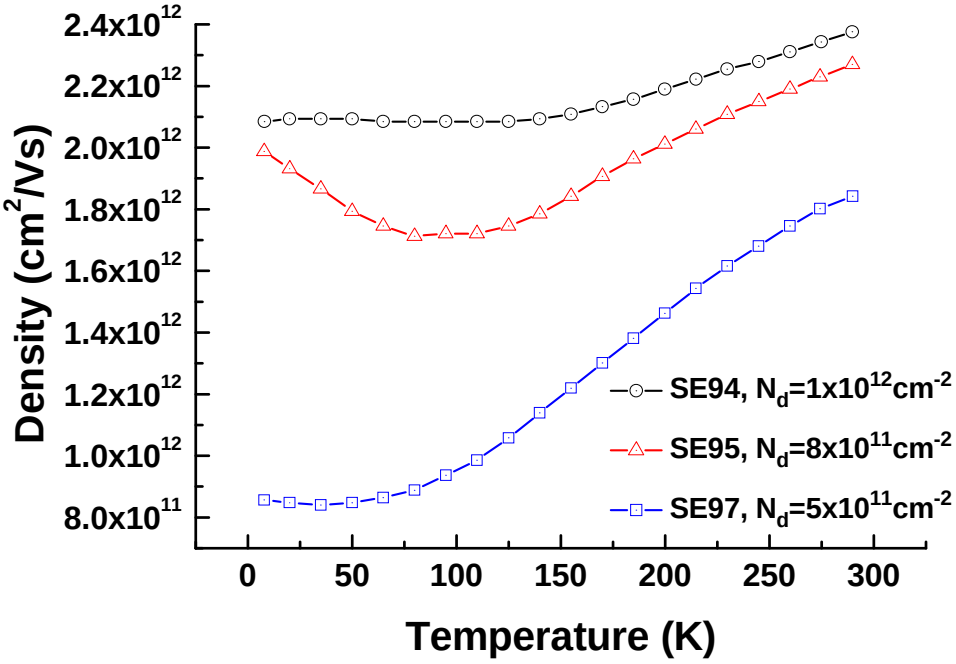


Figure 3.18. A plot of temperature dependent measurements of electron density for GaAs quantum wells with Si δ-dopants ($E_{1.0}$, $E_{0.8}$, $E_{0.5}$ samples).

On the other hand the carrier concentration in all QW samples decreases with decreasing temperature, and then saturated or began to increase (as in case of $E_{0.8}$), with further decrease of temperature. The saturation of density with temperature decrease is normal for a degenerate electron gas. The overband measured for $E_{0.8}$ was due to the multi-band conduction effect [4, 8].

Considering QW samples as an electric circuit of three parallel conductors (see Figure 3.19), the total conductivity $\sigma$ of the circuit can be expressed as

$$\sigma = 2\sigma_1 + \sigma_2 , \tag{3.15}$$

where $\sigma_1$ is the conductivity via the Si donor-impurity band, and $\sigma_2$ is the conductivity of the n-type semiconductor GaAs. When the analysis that was described in [31] was applied, it was reasonable to make the conclusion that at lower temperatures the conductivity of Si donor-impurity band started to play an important role and contributed to total conductivity of the samples. As a result, the total number of carriers increased with lowering temperature because of extra channels available for carriers to move. Hence, continued lowering the temperature of the sample resulting in an increase in carrier concentration as seen from measurements using the Hall effect.

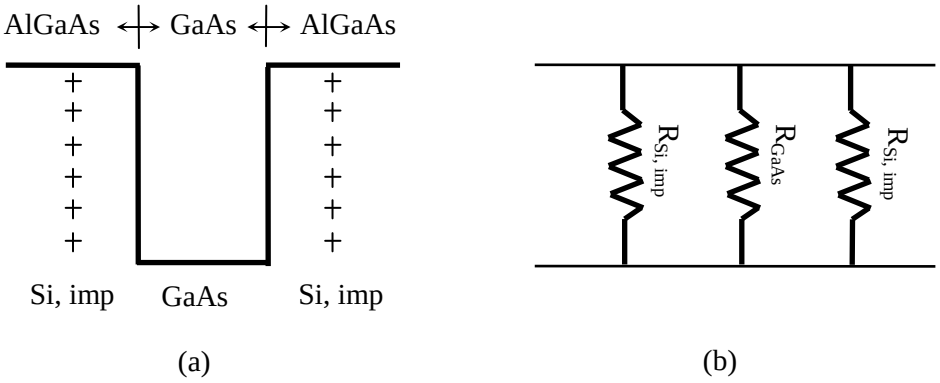


Figure 3.19. A schematic structure of QW Si δ-doped sample (a), and the equivalent circuit consisting of three resistors (b).

# Chapter 4. Experimental Device Fabrication

In order to create the experimental devices that were used for measurements that are presented in this thesis, a number of steps had to be made. A series of specific processes were applied to achieve a desired pattern device structures on wafer. In this chapter a brief overview and detailed explanation of all processes that were used to fabricate experimental devices is presented.

## 4.1. Processes for Experimental Device Fabrication

### 4.1.1. Photolithography Technique

Photolithography is the ability to print high-resolution patterns of different complexity with micron-sized features on a specific substrate. The principle of photolithography technique is very clear. A layer of photoresist of some certain thickness is spun onto the wafer. A mask with the necessary pattern is applied on the wafer. After that the wafer is exposed to UV light, dipping of wafer into the developer will complete the process of transferring the mask pattern to the wafer [32].

Looking at more details on device fabrication process, processing stated with all samples grown on the GaAs substrate. In order to spin photoresist, the wafer had to be cleaned. In this thesis, combinations of cleaning with acetone and methanol were used to remove all organic or inorganic contaminations that could be present on the wafer surface. After that, a layer of photoresist was applied on the sample.

There are two types of photoresist that can be used in photolithography: positive and negative (see Figure 4.1). The difference between them is that positive photoresist, in the areas which were exposed to UV light, will be damaged, and thus those areas will dissolve and rinse away in the appropriate developer. Negative photoresist, after exposure to UV light, becomes

immune and thus remains during development. In order to protect areas of photoresist and to create a special pattern on the sample, different types of masks can be used.

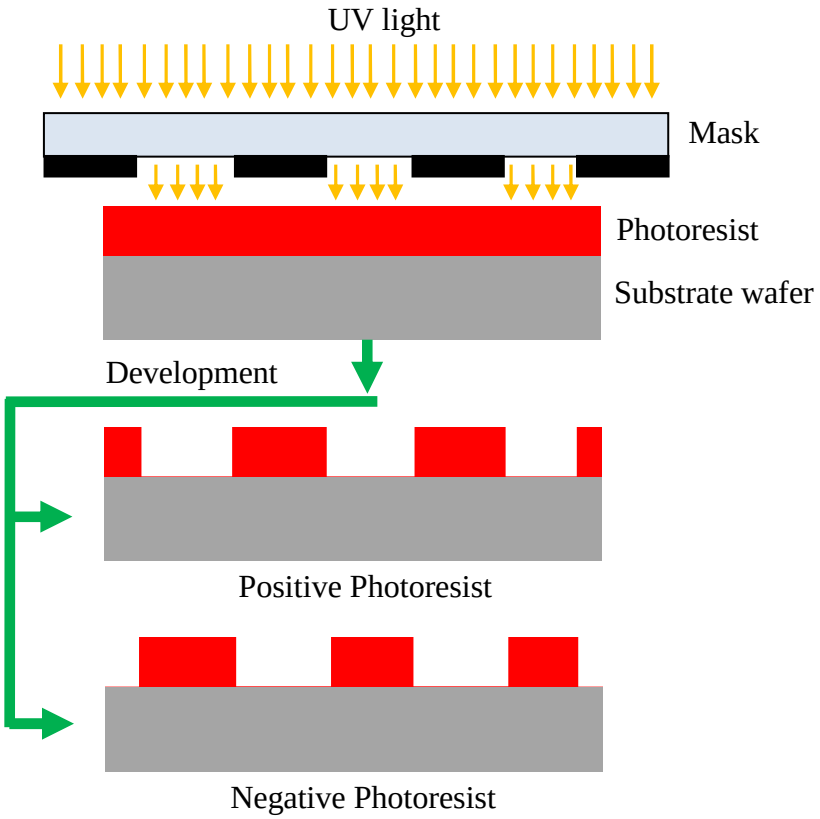


Figure.4.1. A pattern of positive and negative photoresist after exposure to UV light and their development.

A typical tool used to apply photoresist on the substrate is called a spin coater. To get a certain thickness of a photoresist the spin coater has to be specially programmed. For these sets of experiments a programmable spin coater was used with the program steps that are shown in Table 4.1. In addition, a positive photoresist (AZ4330) that gave a thickness up to 5 μm was used. The thickness of the photoresist depended on final spin speed.

To measure the exact thickness of the photoresist that was spun onto the wafer the Dektak profilometer was used. In order to measure the photoresist thickness a small scratch on the photoresist using a special blade was done. After that, the depth of the scratch was measured that

represents the thickness of the photoresist that was applied on the wafer. The average thickness for all the samples was 4900 nm.

Table 4.1. The recipe for spin coater that was used to apply a photoresist.

| | **Step Description** | **Parameters** | |
|---|---|---|---|
| | | **Spinning Speed,** rpm | **Time**, sec |
| 1. | Coat | 0 | 10 |
| 2. | Spread | 500 | 2 |
| 3. | Coverage | 1000 | 2 |
| 4. | Settle | 500 | 2 |
| 5. | Final Spin | 5000 | 30 |
| 6. | Dry Out | 1000 | 5 |

The next step after photoresist was applied was sample baking. For that purpose, a Lindberg/Blue oven preheated to 110°C (383 K) was used. The sample was kept inside of the oven for 3 min. The main reason for using this type of oven instead of the hot plate, a traditional variant to bake a photoresist, was because the sample has to be heated up not very rapidly in order to avoid solvent burst effects.

After the sample was taken out of the oven, the next step was to create a pattern on the photoresist. For that purpose, the Karl-Suss mask aligner and specific device structure masks were used.

There are different methods that can be used to expose the wafer. First, contact printing, when the mask is placed on top of the sample and has direct contact with the photoresist. The alignment of the mask has to be done before the exposure using a microscope to align the wafer and mask patterns. In order to not damage the photoresist, the mask has to be separated from the wafer during the alignment by some distance. Second, proximity printing, is a modified contact printing method, where the mask and the wafer are separated by 5 – 25 µm through the whole

process of wafer exposure. Third, projection printing, where mask is separated from the wafer and special optical system is used to focus the mask pattern on the wafer in a specific place [32]. The contact printing method was used to align the mask for all the samples in this work.

Based on the thickness of the photoresist (4900 nm) and intensity of light (12.54 mJ/cm$^2$) a time for the exposure was estimated to be 15 sec, which was enough to achieve the desired pattern.

The next step was to develop the samples. For AZ4330 photoresist the combination of developer (AZ440K) and water in ratio 1:3 was used. The development time was estimated experimentally based on full removal of exposed photoresist areas and was 1 min 5 sec for all samples.

The very last step in the photolithography process is usually the postbake. This step is designed to complete polymerization of the resist and to make it more resistant for etching. However, during this process the photoresist may flow in different directions and as a result can modify the profile edges. That is why this step was skipped to keep the structure more consistent.

4.1.2. Etching Technique

After the pattern was transferred from the mask to the sample using photoresist, the next very important step was to etch this pattern in order to achieve the desired device structure of the material for further measurements. There are two possible ways to etch the sample: wet and dry etching. Dry etching involves the gas-phase etchants in a plasma. The etching process usually takes place by a combination of chemical and physical process, and because the plasma is involved, dry etching is called plasma etching. Wet etching involves the use of the liquid etchants. In order to perform the wet etching the sample is immersed in the etchant solution and the material is etched by chemical processes. Those areas that were not covered with the

photoresist pattern will be etched away and regions that were masked with photoresist will remain unetched. Wet etchants will react with the film in order to form water-soluble byproducts [32].

In this thesis only wet etching was used to etch the samples because it was the only available technique in the lab. The etchant solution was made by mixing $H_3PO_4$, $H_2O_2$, and $H_2O$ in ratio 1:1:3. This solution was calibrated on GaAs wafer by measuring the time that was needed to etch the GaAs wafer for a necessary depth. Using this data, the graph (time vs. depth) was plotted and approximated by a linear equation: Thickness [nm] = 0.6522*Time [sec]. This approximation was done in order to predict the desired time that a sample has to be placed in the solution to achieve the desired etching depth.

4.1.3. Ohmic and Schottky Contacts Theory and Formation

The most important part of the device fabrication in order to prepare it for further experimental measurements was to make good contacts. “Good contact” means low-resistance (~20 Ohm) connections between the metal and active device regions. However, there is no standard recipe or recipes which can be applied to produce a really good contact on any kind of GaAs. A few reasons can cause this: (1) depending on dimensions, the requirements for contacts are different; (2) different sample structures require different recipes; and (3) one ohmic contact is different for different applications [27].

There are two different types of contacts that are most commonly used, ohmic and Schottky contacts. A typical Schottky contact barrier that is formed on interface between metal and semiconductor can be described by conduction-band diagram that is shown in Figure 4.2.

As can be seen in Figure 4.2, if the electron moves from the metal to the semiconductor it should overcome an energy barrier $e\varphi_B$. However, if the electron is going the opposite way, it

should go over a barrier $eV_{bi}$, where $V_{bi}$ is the diffusion potential. At equilibrium, the electron currents $j_{1e}$ and $j_{3e}$ will have equal but opposite magnitudes because the net current must vanish (see Figure 4.2a). A depletion region of width $w_d$ will be created.

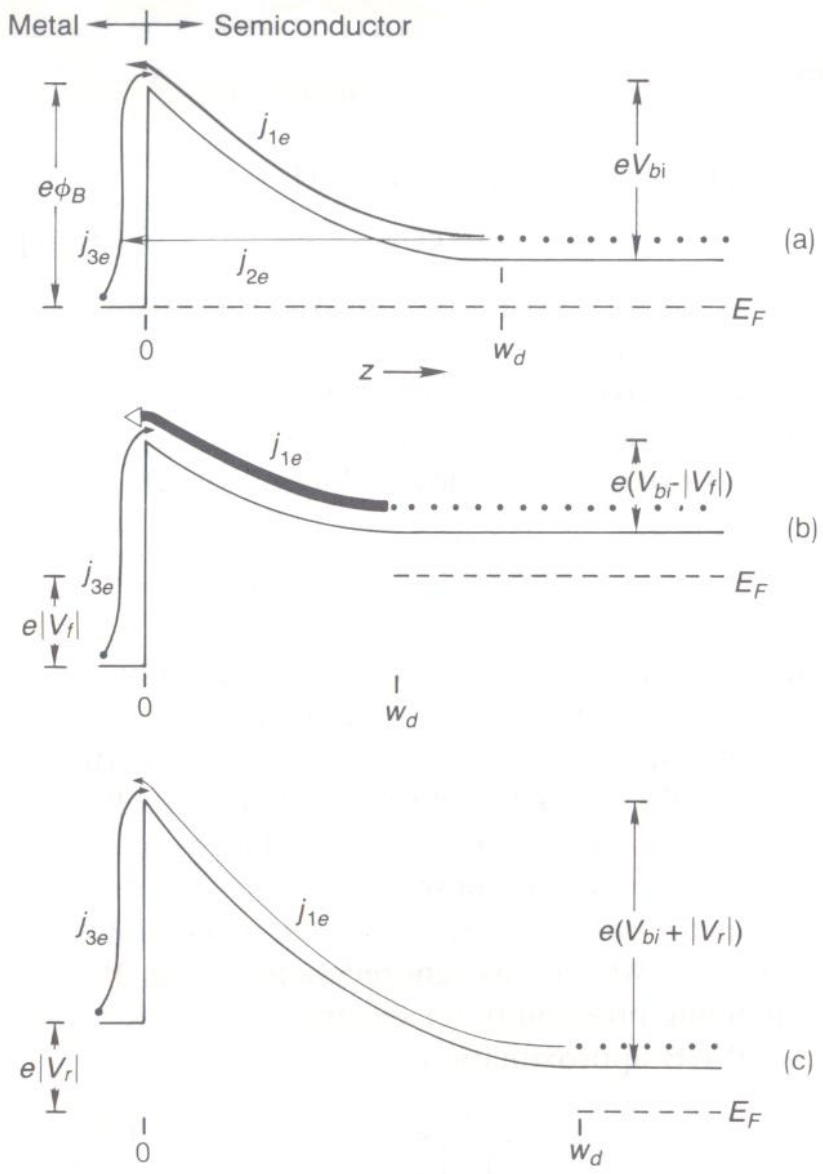


Figure 4.2. A typical Schottky contact barrier that is formed on metal-semiconductor interface under unbiased and biased conditions: (a) no bias; (b) forward bias; (3) reverse bias. $j_{1e}$and $j_{3e}$ are injection current, and $j_{2e}$ is a tunneling current [27].

If a positive voltage $V_f$ is applied to the metal, which is the forward bias for an n-type semiconductor, the metal Fermi level will be lowered by $e|V_f|$ in comparison to the semiconductor (see Figure 4.2b). As the result of applying the forward voltage, the metal-semiconductor barrier will decrease to $e(V_f-|Vf|)$ and the depletion region will be decreased. Hence, the injection current $j_{1e}$ will be increased, but the $j_{3e}$ will stay the same.

When a negative bias is applied to the metal contact, which is the reverse bias for n-type semiconductor, the Schottky barrier will rise by $e|V_r|$, and the depletion region will become larger. Consequently, the current $j_{1e}$ will be decreased, and $j_{3e}$ remains unchanged (see Figure 4.2c).

Another way for carriers to pass the barrier is to tunnel through it (Figure 4.2a), where $j_{2e}$ represents a tunneling current. If the material is heavily doped, the width of the barrier, which is defined by the depletion region width $w_d$, becomes thin enough for the carriers to tunnel through the barrier. If the current can flow in both directions without being influenced by the contact, ohmic behavior can be achieved [32]. In Figure 4.3 the ideal I-V curves for ohmic and Schottky contacts are depicted.

For all the experiments in this thesis, there was no need to create the Schottky contacts and only good ohmic contacts were used. However, in order to understand the ohmic contact behavior, a theory of Schottky contacts was described too.

To create ohmic contacts the Edwards e-beam evaporator was used. To achieve good ohmic contacts, three layers of different metals were evaporated on the sample. The metal contact structure consists of Au/Ge (75nm), Ni (20nm), and Au (200nm), with corresponding thicknesses given in parenthesis.

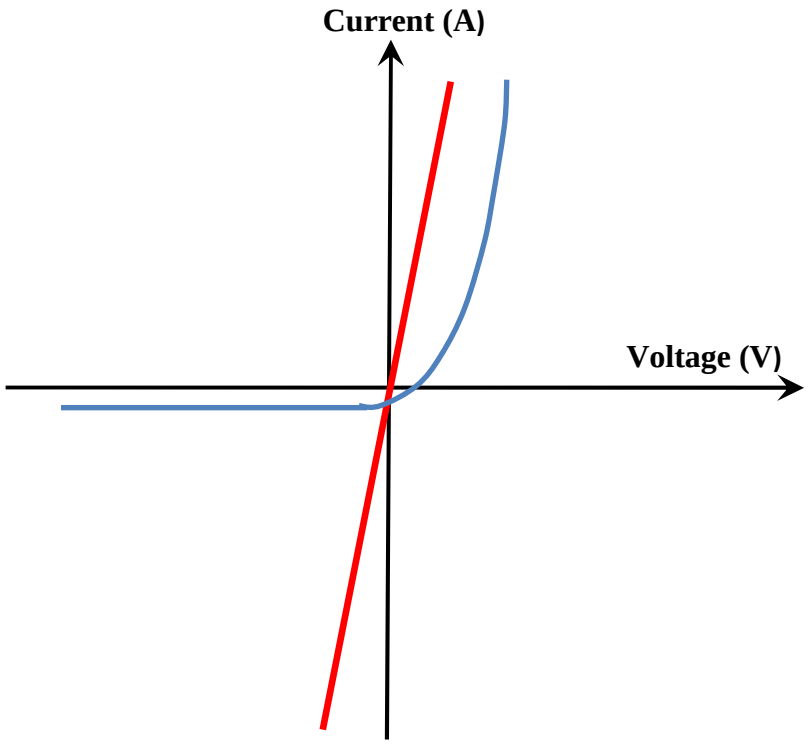


Figure 4.3. Ideal I-V curves for ohmic (red) and Schottky (blue) contacts.

4.1.4. Lift-off Technique

Lift-off technique is very easy method for making metallic contacts on the substrate, especially for those noble metals such as Pt, Ni, Au which are difficult to be etched by regular etching techniques. In general, the lift-off process consists of few steps. First a pattern is transferred from the mask to the substrate using photoresist. A metallic film of desired thickness is deposited all over the substrate, covering the photoresist and those areas where photoresist was removed. After that the substrate placed into the beaker filled with acetone or some other solvents. During the actual lift-off process, the photoresist will be removed, taking the film with it. The metal that was deposited directly on the substrate will stay. As a result, metal contacts will be created [33].

This technique was applied to all the samples to create contacts. The samples were placed in the beaker filled with an acetone. This beaker was mounted in the ultrasonic bath and kept

there until the metal with photoresist underneath of it visually starts to dissolve. After that the samples were taken out of the beaker and the pattern was viewed using the optical microscope. If the pattern was good enough to perform further electrical characterization measurements (the contact were not shorted), the sample was placed in the box for further preparation steps. If not, the sample was returned into the beaker for a longer time and then tested again using optical microscope. This process was repeated as many times as necessary to achieve the desired pattern quality.

4.1.5. Annealing Technique

In order to fabricate good ohmic contacts very often a high temperature step is required. The deposited metals can alloy with the semiconductor and, thus, the high-temperature annealing reduces the Schottky barrier at the metal/semiconductor interface and makes contacts ohmic.

When this work's series of metals were deposited on the GaAs substrate it was rather easy to obtain reasonable ohmic contacts. However, when the sample was annealed at 480ºC in an ambient environment of $N_2$ gas, the contacts were improved. Annealing time is important and was found experimentally to provide optimal contact quality (see Figure 4.4).

The temperature of 480ºC was chosen below the temperature of the GaAs/AuGe/Ni/Au eutectic composition. Annealing at this or higher temperatures will cause the formation of GaAs/AuGe/Ni/Au alloy, which will result in creating pits in the GaAs. This effect is also known as spiking. Hence, when these spikes penetrate though an underling p-n junction they influence the quality of the p-n junction, and as a result, decrease the barrier between them. The use of a reduced atmosphere avoided any further oxidation of the metals during the annealing process. Also, it reduced any oxide creation on the interface between the metal and semiconductor.

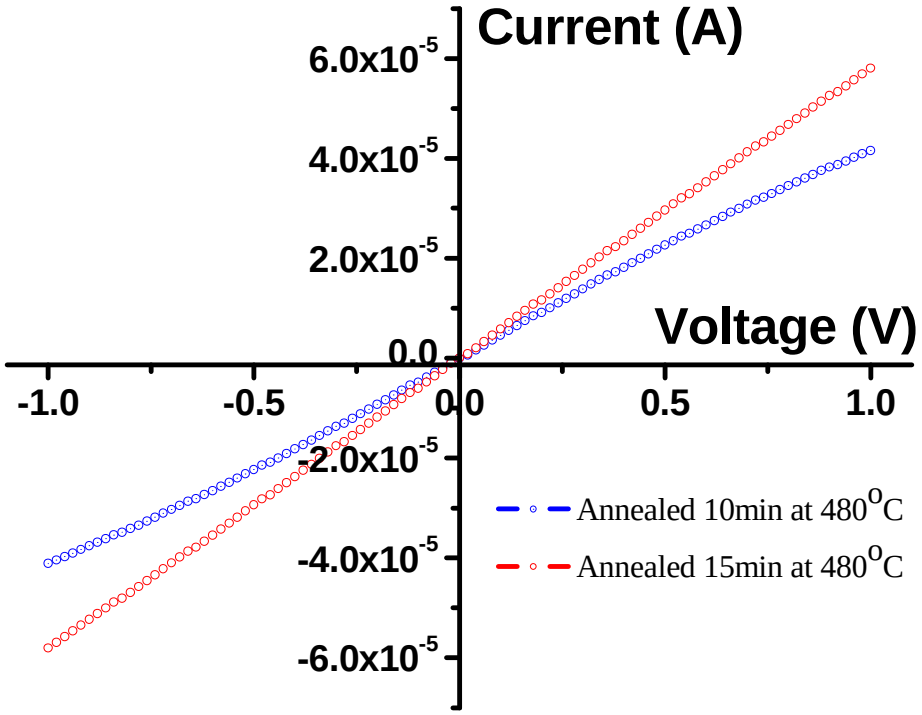


Figure 4.4. Experimentally measured I-V characteristics of ohmic contacts for different annealing time at ambient environment of $N_2$ gas

### 4.2. Contact Resistance Optimization

As discussed earlier, the contacts were annealed for 15 min at 480ºC in presence of nitrogen gas to achieve good quality ohmic contacts. To measure the contact resistance and bulk sheet resistance, the pattern in Figure 4.a was used. The analysis of different effects that take place in the whole metal-semiconductor system was carried out using the transmission line model (TLM). Using the TLM model, contact resistance and sheet resistance of the bulk material can be measured.

The TLM structure consisted of identical ohmic contacts of width $W$ and length $L_c$, (see Figure. 4.5a), which were spaced at distances $L_i$ of 7.8, 10.8, 14.1, 19.9, and 25.6 μm in the device structure that is shown in Figure 4..

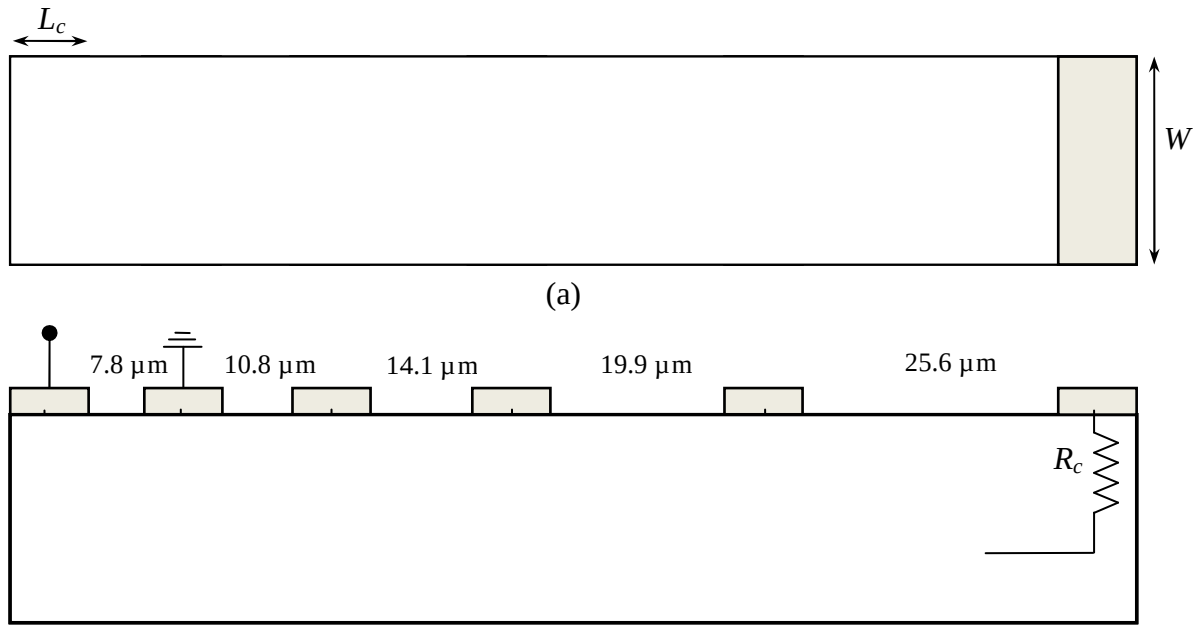


Figure 4.5. (a) A standard TLM contact-resistance pattern with corresponding contact width and length, (b) a transmission-line-model equivalent circuit for current flow in a thin-layer semiconductor device.

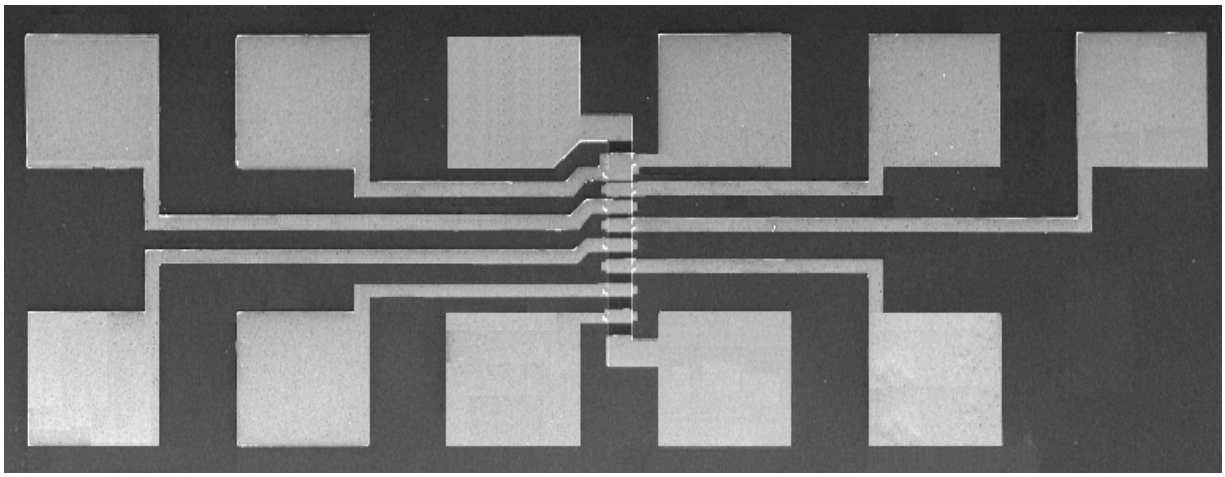

Figure 4.6. An experimental TLM structure that was used to perform measurements of the contact resistance.

To perform the current-voltage measurements, the total resistance will consist of two components (see Figure 4.5b) and is determined by [27]

$$R = 2R_c + r_s \frac{L_i}{W}, \tag{4.1}$$

where $R_c$ is the contact resistance and $r_s$ is the sheet resistance of the semiconductor material between the contacts. For these materials $R_c$ was at least 20x times lower than $r_s$. By plotting the total resistance $R$ versus the separation distances $L_i$ and applying a linear fit, the slope of the resulting line will be $r_s/W$, and the intercept $2R_c$ (see Figure 4.7).

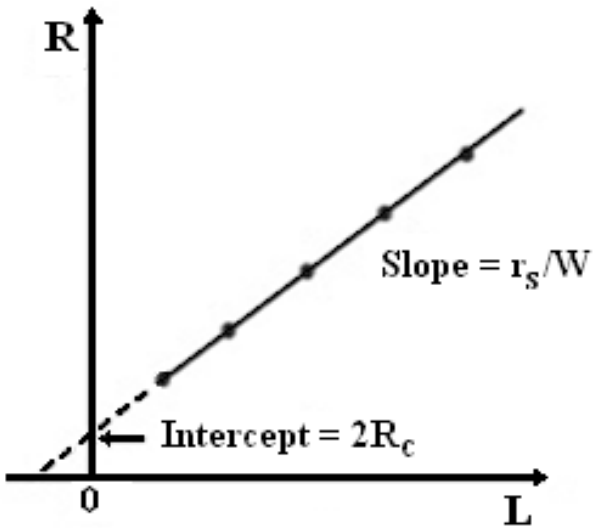


Figure. 4.7. The expected resistance $R$ as a function of contact-spacing $L_i$ for the pattern depicted in Figure 4.5a [27].

For all three QW samples the TLM technique was applied in order to estimate the contact resistance. In Figure 4.8 it can be seen how contact resistance $R_c$ for each samples depends on the doping concentration $N_d$. As it can be seen from Figure 4.8 the sample with the highest $N_d$ has the lowest $R_c$.

To estimate the contact resistance at different temperatures and how it depends on temperature, the TLM technique was applied. The corresponding graph is shown in Figure 4.9. The measured value of total resistance $R$ at room temperature was 6.125 kOhm. Those results were used for further precise calculation of the electric field applied across the devices.

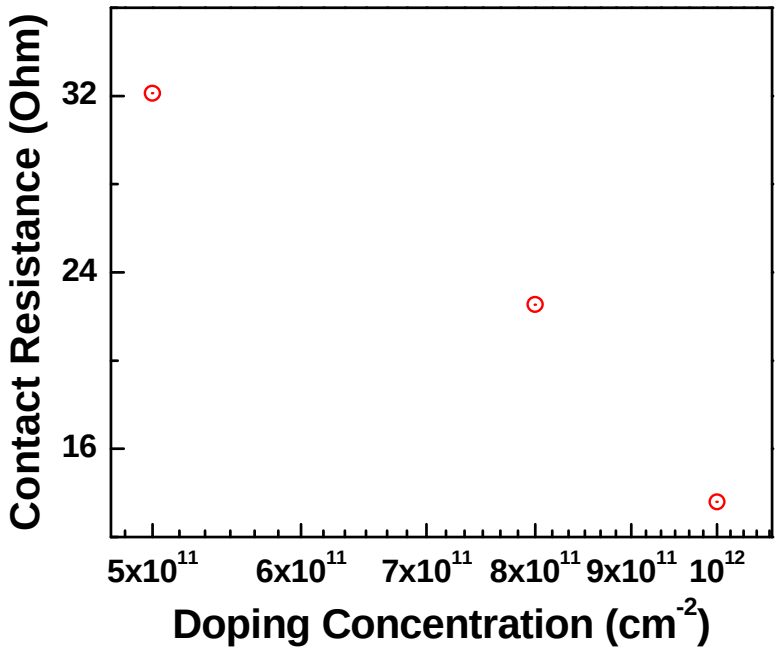


Figure 4.8. A plot of contact resistance versus doping concentration at room temperature for QW heterostructure samples.

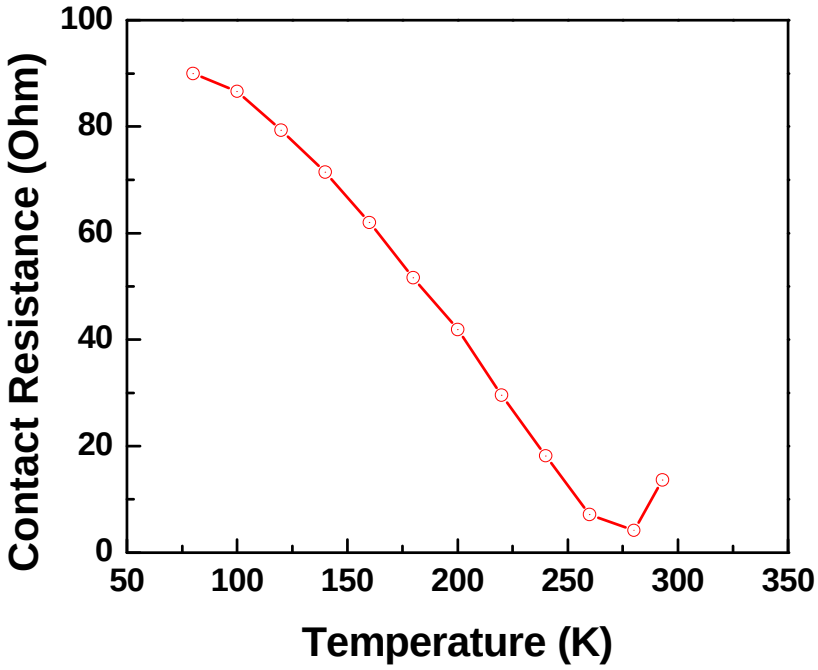


Figure 4.9. A plot of contact resistance versus temperature for $E_{1.0}$ sample.

### 4.3. Completed Experimental Device

At the end of the fabrication process structure that is shown in Figure 4.10 for each sample under investigation was achieved. As it can be seen, there were eight different structures for different types of electrical measurements. However, only three of them were used for the experiments presented in this thesis and are shown by boxes in Figure 4.10. The large structure that was used for TLM measurements is shown only in Figure 4.6, while the other two device structures are shown in Figure 4.11 in more details. The structure depicted in Figure 4.11a was used for pulsed I-V measurements that are described in Chapter 6, and the structure that is shown in Figure 4.11b was used for noise (Chapter 5) and Hall effect measurements (Chapter 3).

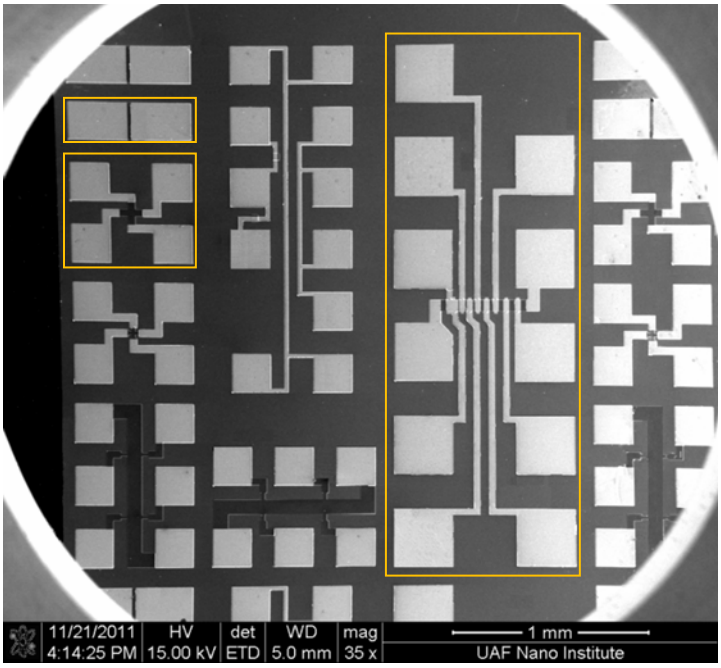


Figure 4.10. The SEM image of different device structures that were achieved at the end of the device fabrication process.

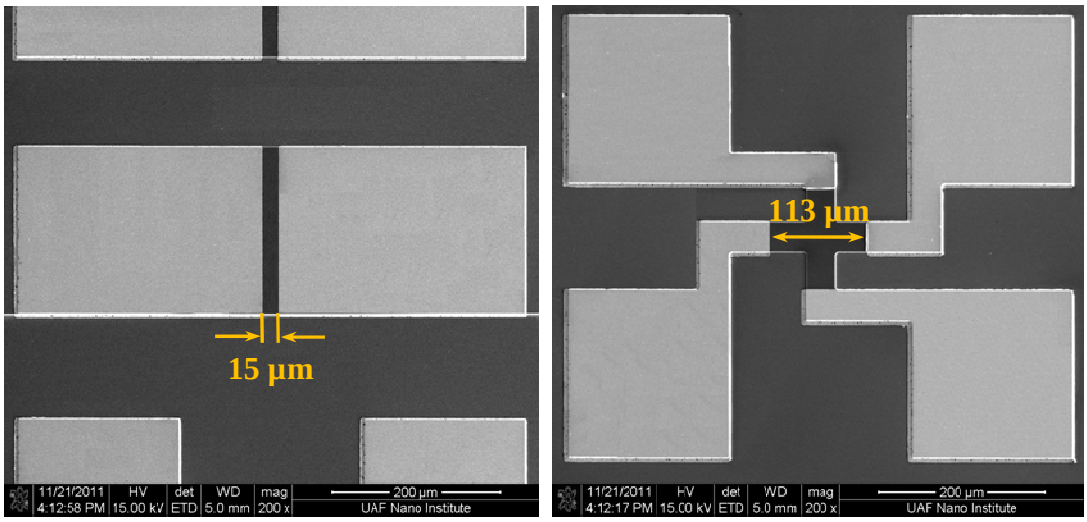


Figure 4.11. The SEM images of the devices that were used in (a) pulsed I-V measurements, (b) low-frequency noise spectra measurements.

# Chapter 5. Methodology of Noise Measurements

Different types of noise in semiconductors are associated with a variety of physical processes that determine device performance. By studying noise in solid state devices, i.e. low-frequency fluctuations, one can learn about different physical processes. Thus, the low-frequency noise measurement technique is a very important and sensitive tool in material characterization.

Noise measurements provide a challenge as one is dealing with very low signals in the nano-Volt range. Hence, consideration for outside interferences, such as electromagnetic shielding, should be accounted for in the experiment design, data acquisition, and data analysis. In this work, the noise studies were performed for bulk layers of AlGaAs and AlGaAs/GaAs heterostructures. Different types of low-frequency noise were considered and analyzed accordingly.

## 5.1. Types of Noise in Semiconductor Devices

Any random fluctuation in the measurement process is noise. In the frame of this thesis, the noise was associated with materials and device characteristics and was studied at low frequencies (1 Hz – 100 kHz). Fluctuations in semiconductor materials are usually considered as some restriction in device sensitivity and device operation [34]. This is why all previous measurements in the area of low-frequency noise studies were oriented around device operation and device performance for different applications. Furthermore, the main goal of the research was to understand the origins and behavior of different fluctuations in order to lower the noise signals and increase the stability and sensitivity of devices.

There are four dominant types of noise in modern semiconductor devices: shot noise, thermal noise, 1/f noise, and generation-recombination noise. Depending on certain conditions, one or more types of noise can dominate.

5.1.1. Shot Noise

Shot noise can occur in a system when the current flows across a potential barrier. This current can be expressed as the number of carriers that cross the barrier during some period of time. When electrons cross the potential barrier in some random period of time, the shot noise current takes place. A typical example for this type of noise is the noise measured in the collector current of a transistor. The current noise spectral density of shot noise $S_{NI}$ can be presented as [35]

$$S_{NI} = 2qI, \tag{5.1}$$

where $q$ is charge of the electron, $I$ is the device current.

5.1.2. Thermal Noise

Thermal noise, or Johnson-Nyquist noise, is due to random carrier movement caused by Brownian motion. It can be described by a white noise spectrum. Also, this type of noise can be observed in all semiconductor devices possessing a resistance when current passes through [36].

The thermal noise can be described by a voltage noise spectral density as [2, 3]

$$S_{NV} = 4k_bTR, \tag{5.2}$$

where $k_b$ is Boltzmann's constant, $T$ is the temperature, $R$ is the resistance of the noise source. Usually, thermal noise is frequency independent and called "white noise".

5.1.3. 1/f Noise (Flicker Noise)

Flicker noise, or 1/f noise, has been under extensive investigation for many decades. Flicker noise is characterized as inversely proportional to frequency $f$ and dominates the noise spectrum at low frequencies. A number of theoretical and experimental studies have been presented to help understand the origins of the flicker noise [1, 3–6].

In 1969, Hooge presented an empirical relation for flicker noise in homogeneous samples [37]

$$\frac{S_G}{G^2} = \frac{\alpha}{fN}, \tag{5.3}$$

where $S_G$ is the noise spectral density, $G$ is the conductivity, $N$ is the total number of charge carriers in the device, $\alpha$ is a dimensionless parameter (the Hooge parameter), and $f$ is the frequency. The parameter $\alpha$ is used as a normalized measure of 1/f noise in semiconductor materials and devices and was considered a constant in previous studies. However, later it was found to be temperature dependent. Currently, the crystal quality can be defined [38–45] in terms of the Hooge parameter.

The flicker noise is caused by fluctuations of the conductivity. The conductivity in semiconductors is given by [46]

$$\sigma = q(\mu_n n + \mu_p p), \tag{5.4}$$

where $q$ is the elementary charge, $\mu_n$ and $\mu_p$ are the electron and hole mobilities, respectively, and $n$ and $p$ are the concentration of free electrons and holes, correspondingly.

According to Equation (5.4), the conductivity fluctuations can be caused by fluctuations in the number of free carriers or by fluctuations in mobility. However, there is no current, comprehensive theory describing 1/f noise in semiconductors that would is accepted by all scientists in the semiconductor field.

There are a number of different models that suggest an explanation for the 1/f noise. According to first model proposed by McWhorter in 1955 [47], the 1/f noise is a result of trap-induced carrier fluctuations. He suggests the fluctuations in the number of free carriers are due to the trapping and de-trapping processes at the semiconductor/oxide interface. These traps are

localized in the oxide layer at short distances from the bulk semiconductor. The mechanism of carrier trapping and de-trapping caused by these traps may result in the generation-recombination processes that lead to the 1/f noise.

The second model to explain 1/f noise is based on carriers scattering on the lattice vibrations [6, 15, 16]. In other words, the 1/f noise is due to mobility fluctuations in the volume of the semiconductor. Despite the fact that this model does not need any traps to be considered, it implies that even without traps 1/f noise can still be present [6, 17].

A third approach to understand the theory of 1/f noise is to take into account the number of defects that are present in semiconductor material and any type of electron scattering. This assumption was made by Handel in [51]. He says that the 1/f noise is related to electromagnetic effects resulting from any type of electron scattering mechanism. It will cause the fluctuations of mobility, and, thus low-frequency 1/f noise. Handle's model has agrees well with Hooge's relation given by Equation (5.3). However, his model predicts Hooge's parameter is much lower than presented previously by van der Ziel [52]. Future modifications of the $\alpha$ value were mainly done to agree with calculated and experimental values [53].

As previously mentioned, the mobility fluctuations are related to different scattering mechanisms. By applying Matthiessen's rule for different scattering mechanisms, the measured mobility is given by

$$\frac{1}{\mu_{meas}} = \frac{1}{\mu_{Latt}} + \frac{1}{\mu_{imp}}, \tag{5.5}$$

where $\mu_{Latt}$ is the mobility related to lattice scattering, and $\mu_{imp}$ is the mobility due to impurity scattering. Taking into consideration Equation (5.5), the mobility fluctuations can be expressed as

$$\Delta\mu_{meas} = \left(\frac{\mu_{meas}}{\mu_{Latt}}\right)^2 \Delta\mu_{Latt} + \left(\frac{\mu_{meas}}{\mu_{imp}}\right)^2 \Delta\mu_{imp} . \tag{5.6}$$

For 1/f noise, the noise spectral density measured as fluctuations of voltage $S_V$, resistance fluctuations $S_R$, or mobility fluctuations $S_\mu$, is given as

$$\frac{S_V}{V^2} = \frac{S_R}{R^2} = \frac{S_\mu}{\mu^2} = \frac{\alpha}{Nf} . \tag{5.7}$$

Using Equations (5.6) and (5.7), it can be shown that the measured Hooge parameter will depend on ionized impurities and lattice vibrations as

$$\alpha_{meas} = \left(\frac{\mu_{meas}}{\mu_{Latt}}\right)^2 \alpha_{Latt} + \left(\frac{\mu_{meas}}{\mu_{imp}}\right)^2 \alpha_{imp} , \tag{5.8}$$

where $\alpha_{Latt}$ and $\alpha_{imp}$ are the material constants that have a temperature dependent behavior. Equation (5.8) shows that both types of scattering mechanisms play a role in the 1/f noise.

5.1.4. Generation-Recombination (GR) Noise

The generation-recombination noise is a result of fluctuations due to the number of free carriers in the semiconductor material. Any semiconductor material has a certain amount of traps and recombination centers. The process of spontaneous trapping and re-emitting carriers will lead to fluctuations of the number of carriers participating in the conductivity process (see Equation (5.4)). These fluctuations are called generation-recombination noise.

The noise current spectral density of generation-recombination noise for a particular type of generation-recombination process is given as [35]

$$S_{NI} = AI^2 \frac{4\tau_r}{1 + (2\pi f \tau_r)^2} , \tag{5.9}$$

where $A$ is a parameter that depends on device performance and generation-recombination processes, I is a current that flows through the device, $\tau_r$ is the carrier lifetime for this process, $f$ is a frequency.

The carrier lifetime for the generation-recombination process can be expressed taking into account the capture time $\tau_c$ and the emission time $\tau_e$. The dependence is given by

$$\frac{1}{\tau_r} = \frac{1}{\tau_e} + \frac{1}{\tau_c}. \tag{5.10}$$

This type of noise will have a significant impact on the device performance at low frequencies.

In this work only three types of noise were measured in our samples: 1/f noise, generation-recombination noise and thermal noise. The short noise was not measured. Figure 5.1 presents these three different types of low-frequency noises for a GaAs sample.

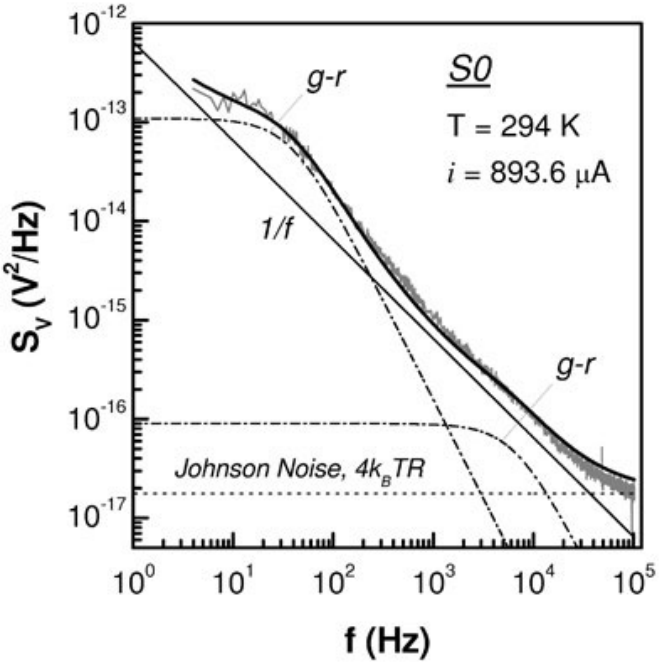


Figure 5.1. An example of three types of noise measured in noise voltage fluctuations of the GaAs sample [54].

## 5.2. Noise Spectroscopy of Deep Traps

Deep level noise spectroscopy (DLNS) is used to understand the origins of generation-recombination noise in semiconductor structures. DLNS is a powerful technique which allows the characterization of deep trap states in semiconductors. This technique is based on the fact that the generation-recombination process is temperature dependent. That means that different generation-recombination processes occur at certain temperatures in the device and have a different contribution to the device performance. This technique is competitive with another experimental technique known as Deep Level Transient Spectroscopy (DLTS).

Noise spectroscopy has some advantages over transient spectroscopy. DLTS fails when the Fermi level is positioned below the energy level of investigation over the whole range of temperatures. Also, with DLTS it is not able to detect levels with very small cross sections ( $\sigma \leq 10^{-20} cm^2$ ). Additionally, when the cross section depends exponentially on the temperature, it is very difficult to calculate the trap parameters with DLTS [55].

There are two ways to present experimental noise data (see Figure 5.2): first, dependence of noise density *S* versus frequency *f* at a wide range of temperatures [56–58]. Second, noise density *S* versus temperature *T* for number of frequencies [59–62]. These two types of forms are equivalent.

An accurate method for extracting the local level parameters from noise spectroscopy data was suggested by Levinshtein and Rumyantsev[55]. When the electron capture cross section $\sigma_n$ has exponential dependence on temperature ( $\sigma_n = \sigma_0 \exp(-E_1/k_bT)$ ), the energy position of the deep level in the band gap $E_0$, the activation energy $E_1$, the trap density, and the electron capture cross section can be calculated.

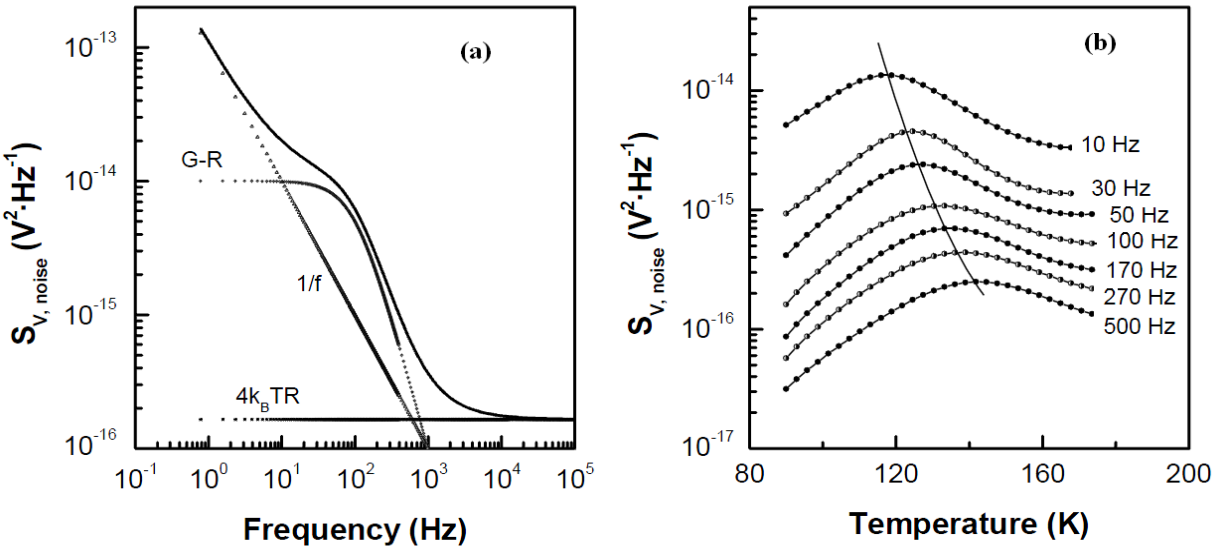


Figure 5.2. Two different ways to display noise data [63].

First consider the n-type semiconductor crystal with a shallow donor level of a concentration $N_d$ that is fully ionized ($n_0 \cong N_d$). The position of the Fermi level will be determined by

$$E_F = k_b T \ln\left(\frac{N_c}{N_d}\right), \tag{5.11}$$

where $k_b$ is the Boltzmann constant, $T$ is the absolute temperature, and $N_c$ is the effective density of states for electrons.

The relative noise spectral density $S$ is given by [64]

$$S = \frac{S_R}{R^2} = \frac{S_U}{U^2} = \frac{S_I}{I^2} = A\frac{\tau F(1-F)}{1+(\omega\tau)^2}, \tag{5.12}$$

where $\omega = 2\pi f$ , $R$ is the sample resistance, $U$ and $I$ are voltage and current, respectively. $S_R$, $S_U$, and $S_I$ are the noise spectral densities of the resistance, the voltage, and the current, respectively. The factor $A = 4N_t / VN_d^2$ depends on the sample volume $V$ and deep level concentration $N_t$. The time constant $\tau$ is given as

$$\tau = \tau_c F \ , \tag{5.13}$$

where $\tau_c = 1/\sigma v_T n_0$ is the capture time. Occupancy of the level *F* is given by

$$F = \frac{1}{1+\exp\left[\left(E_F - E_0\right)/kT\right]} . \tag{5.14}$$

Since $\sigma$ has an exponential dependence on the temperature, the capture time is given as

$$\tau_c = \tau_{c0} \exp\left(\frac{E_1}{k_b T}\right), \tag{5.15}$$

where $\tau_{c0} = \left(\sigma_0 v_T n_0\right)^{-1}$.

Taking into consideration Equations (5.13)-(5.15), the Equation (5.12) can be rewritten as

$$S = A\frac{\tau_{c0}\exp\left(E_1/kT\right)F^2(1-F)}{1+\omega^2\tau_{c0}^2\exp\left(2E_1/kT\right)F^2} . \tag{5.16}$$

There are two cases that have to be considered while performing the noise spectrum analysis. The first case is when the Fermi level is located much higher than the trap level for the whole range of temperatures in the experiment [ $(E_0 - E_F >> k_b T)$ ]. The second case is when the Fermi level lies much lower than the trap level for the whole range of temperatures [ $(E_F - E_0 >> k_b T)$ ]. For these two cases, it is necessary to plot $1/k_b T_{\max}$ versus $\ln(\omega)$, and $\ln(S_{\max})$ versus $\ln(\omega)$ (see Figure 5.3). Based on these slopes, the activations energy $E_1$ and the energy position of the deep level traps $E_0$ can be determine.

For the first case, $(E_0 - E_F >> k_b T)$, the activation energy and the deep level trap energy can be calculated using equations [55]

$$E_1 = \frac{1}{\tan\theta_T} , E_0 = \frac{1-\tan\theta_S}{\tan\theta_T} . \tag{5.17}$$

When $\tan\theta_S \approx 1$, it is difficult to estimate the deep level trap energy because the theory reaches its limitation, and in that case, some additional experiments are required [55], [65].

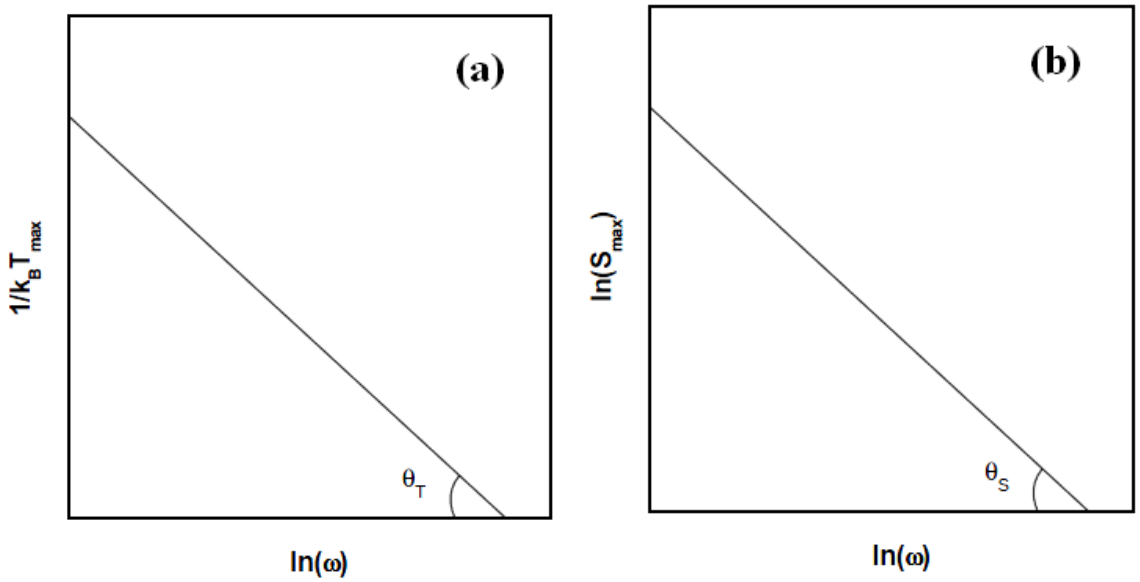


Figure 5.3.The plots to determine the slope $\theta_T$ and $\theta_S$ .

For the second case, both energies can be calculated using equations

$$E_1 = \frac{2 - \tan\theta_S}{\tan\theta_T}, \qquad E_0 = \frac{\tan\theta_S - 1}{\tan\theta_T}. \tag{5.18}$$

Once the activation energy and the deep level energy position are calculated, the capture cross section is given as

$$\sigma_0 = \frac{1}{\tau_{c0} v_T n_0}. \tag{5.19}$$

The trap density can be estimated using equation

$$N_t = \frac{1}{4} AVN_d^2. \tag{5.20}$$

After the activation energy, the position of deep level trap energy, the capture cross section, and the trap density have been calculated, the behavior of traps in the device can be evaluated.

## 5.3. Experimental Setup and Measurement Results

The big part of this thesis deals with noise measurements to investigate deep traps present in our samples. As mentioned earlier, noise spectroscopy is a powerful tool for material studies; however, noise measurements are a complicated task due to the very low signals that have to be measured. The presence of any other interfering, external signals coming from other electronic devices might contribute to a measured noise signal. That is why the measurement setup has to be designed very carefully, taking into consideration the shielding and low noise power supplies (batteries).

### 5.3.1. Installation and Setup Calibration

To perform low frequency measurements, a very low noise preamplifier with a differential input was used.

Figure 5.4 presents the low-frequency noise measurement setup that was used in this work's measurements. Most of the parts of the noise measurement setup were placed inside of the Faraday cage to avoid external, interfering noise sources, such as electrical transmission lines. The main parts of this setup were:

(1) A cryostat with the device under test inside. In these studies a low noise cryostat manufactured by MMR technologies was used.

(2) A low noise preamplifier SR560 from Stanford Research Systems that was used to amplify the signals by a 1000.

(3) Battery and set of load resistors were used to bias the device under investigation. The load resistor was at least 10 times larger than the resistance of the test device.

(4) A two channel dynamic signal analyzer SR785 (Stanford Research Systems) was used to acquire and analyze the amplified noise signal. All measurements were done in four-probe geometry to avoid noise of contacts. A Greek cross geometry as shown in Figure 4.11b was used. The main principle of the noise analyzer is to collect data, digitize them and, by applying a Fast Fourier Transformation, convert them from the time domain to the frequency domain.

(5) A K-20 (MMR technologies) temperature controller was used to control the temperature of the sample.

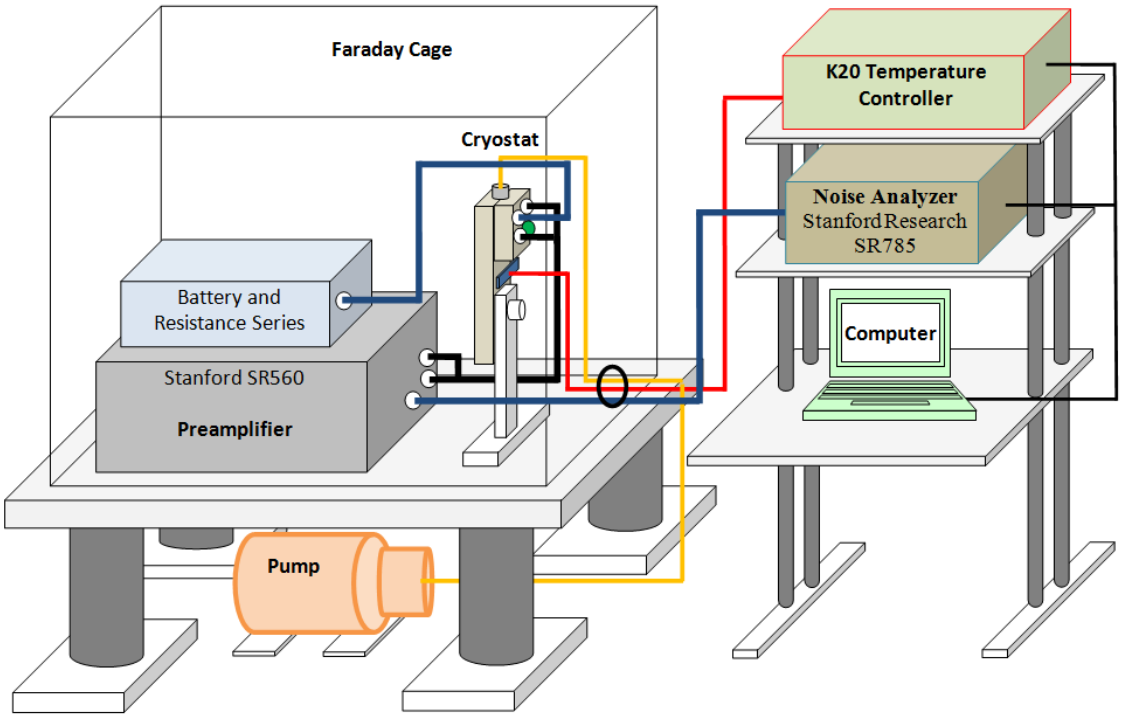


Figure 5.4. Schematic presentation of noise measurement setup for extracting of noise spectra.

A standard PC was used to acquire data and to control the experimental setup via a General Purpose Interface Bus (GPIB interface) and a specially developed LabView program.

For this setup the measurements were done in the frequency range from 10 Hz to 100 kHz at fixed temperatures from 82 K to 390 K in steps of 10 K.

To study the noise signal of the sample, one has to take into consideration other sources of noise coming from measuring apparatus such as noise spectrum analyzer, preamplifier, wires, power supplies, etc. Therefore, to measure the real voltage noise spectral density of the device, certain calibration procedures that were described in this section had to be done.

The voltage noise spectra density of the device can be calculated using the equation from [63]

$$S_{V,noise}(f) = \frac{\Delta V_{noise}^2}{\Delta f} = \frac{P_1 - P_2}{K^2 \Delta f}, \tag{5.21}$$

where $P_1$ is the total noise power spectrum, $P_2$ is a joint noise power of preamplifier and inputs that were shortened, $K$ is the preamplifier gain, $\Delta f$ is the noise bandwidth.

The voltage noise spectral density of the calibration resistor $R_{calib}$ is given by

$$S_{V,R}(f) = 4k_b T_{calib} R_{calib}. \tag{5.22}$$

By performing measurements of the total noise power with a calibration resistor loaded on the input of the preamplifier, the result can be expressed as

$$P_3 = P_2 + K^2 \Delta f \, 4k_b T_{calib} R_{calib}. \tag{5.23}$$

Using Equations (5.23) and (5.21), the real noise of the device can be estimated as

$$S_{V,noise} = \frac{P_1 - P_2}{P_3 - P_2} 4k_b T_{calib} R_{calib}. \tag{5.24}$$

Taking into consideration experimentally measured noise densities for different noise power spectrums and using Equation (5.24), the real noise of the device can be presented as

$$S_{V,noise} = \frac{S_{V,total} - S_{V,short}}{S_{V,R} - S_{V,short}} 4k_b T_{calib} R_{calib}, \quad (5.25)$$

where $S_{V,R}$ is the total noise power with a calibration resistor loaded on the input of the preamplifier, $S_{V,short}$ is the total noise power with shorted input of the preamplifier, $S_{V,total}$ is the total noise density spectrum that was measured.

If we subtract the thermal noise from the device noise, the excess noise can be estimated as

$$S_{V,excess} = S_{V,noise} - 4k_b T_{sample} R_{sample}. \quad (5.26)$$

Therefore, in order to determine the real voltage noise spectral density $S_{v,noise}$ of the device only, calibration measurements were done.

5.3.2. Low Frequency Noise Measurements

The low frequency noise spectrum was measured in the 10 Hz to 100 kHz frequency range for samples with Greek cross geometries. The active area of the device was 113 $\mu m^2$ (see Figure 4.11b). The noise measurements were performed for the same geometry and device size for all samples for comparison. Additionally, the measurements were done at the same current of 10 µA, with the same experimental conditions for all samples.

The noise spectrum was measured using the four probe method in the temperature range from 82 K - 390 K. LabView developed software was used to acquire data from the Noise Spectrum Analyzer and to extract the real noise signal of the device, with taking into account setup calibrations (see Equation 5.25).

The measured voltage noise spectral density of the device was fit using following equation

$$S_{V,noise} = \frac{A}{f} + \frac{B}{1+\left(f/f_0\right)^2} + 4k_bTR\,, \tag{5.27}$$

where $A$ is the amplitude of flicker noise, $f$ is a frequency, $B$ is the amplitude of generation-recombination noise, $f_0$ is the characteristic frequency for generation-recombination noise, $k_b$ is the Boltzmann constant, $T$ is the sample temperature, and $R$ is the sample resistance.

The example of the noise spectrum fit using Equation (5.27) is depicted in Figure 5.5.

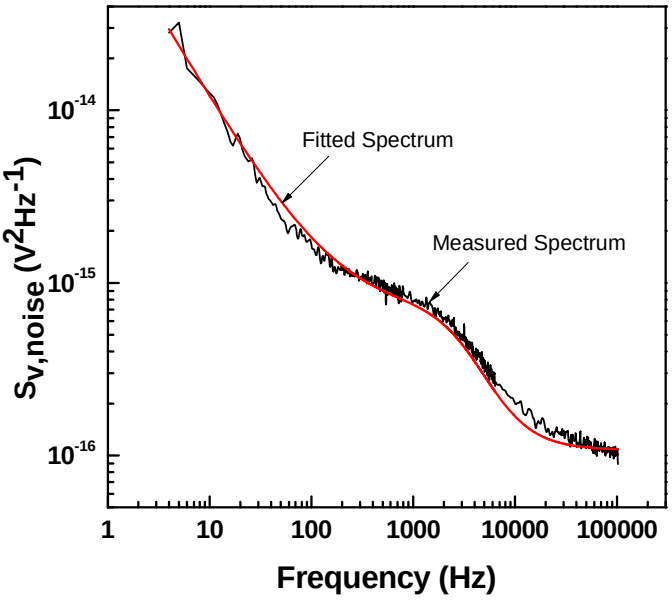


Figure 5.5. An example of a fitted spectrum for $E_{1.0}$ sample with 220 kOhm load resistor at T = 294 K.

With increasing load resistance in the circuit from 27 kOhm to 860 kOhm, the device bias current can be varied and, thus, the voltage noise spectral density can be measured as a function of bias current. At very high bias currents the amplitude of thermal noise can rise as result of the hot electron phenomena in the sample. At high bias currents or high electric field across the device, the electron gas can be heated and the lattice temperature will increase accordingly. As a result, the thermal noise will increase.

5.3.3. 1/f Noise and Hooge Parameter

In early studies of 1/f noise, the Hooge parameter $\alpha$ was believed to be a constant ~$2x10^{-3}$ [37]. But further investigations showed that the Hooge parameter depends on the crystal quality and the scattering mechanisms [66–68].

The results of the analysis done for all samples in this work indicated that 1/f noise was a predominant source of low-frequency noise in these samples. Studies of 1/f noise as function of the number of dopants and the mobility for these samples were performed. Three samples with different dopant concentrations $N_d$ were chosen: $E_{1.0}$ ($N_d$= $1x10^{12}$ $cm^{-2}$), $E_{0.8}$ ($N_d$= $8x10^{11}$ $cm^{-2}$), $E_{0.5}$ ($N_d$= $5x10^{11}$ $cm^{-2}$).

Using the first term of fitting Equation (5.27), the $A$ parameter of the 1/f noise can be given as [36]

$$A = \frac{\alpha V^2}{N}, \tag{5.28}$$

where $\alpha$ is the previously defined Hooge parameter, $V$ is the bias voltage, and $N$ is the total number of carriers in the device.

The total number of carriers can be calculated using

$$N = \frac{L}{eR\mu}, \tag{5.29}$$

where $L$ is the distance between the opposite contacts of the Greek cross geometry, $e$ is the electron charge, $R$ is the sample resistance, and $\mu$ is the mobility of the sample.

In order to determine the Hooge parameter $\alpha$, a number of experiments and modeling were completed: First, the noise spectra were measured as function of different bias current in the ohmic region of the I-V curve. Second, using Equation (5.27) each individual spectrum was fitted. For this step, the temperature $T$ of the sample, the resistance $R$, and the characteristic

frequency of generation-recombination noise $f_0$ were kept as constant values. Third, a plot of the amplitude of 1/f noise, $A$, versus $V^2$ ($V$ is the bias voltage across device terminals) was created. Forth, the plotted data was fitted linearly according to Equation (5.28). From a linear fit, the slope was calculated. Using the value of the slope, the Hooge parameter $\alpha$ was calculated using the following equation

$$\alpha = slope \cdot N \ . \tag{5.30}$$

The same procedure was repeated for all three samples at room temperature. Measured noise spectra for different bias currents and corresponding plots of the parameter $A$ versus the square of voltage $V$ applied across the device are presented in Figures 5.6- 5.8.

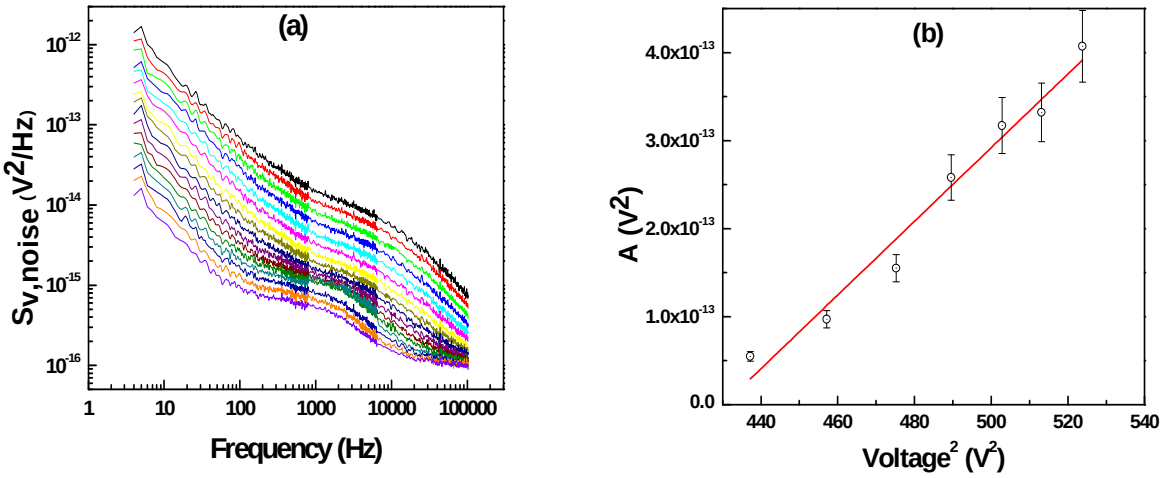


Figure 5.6. (a) Noise voltage spectra for $E_{1.0}$ sample for various biases. The bias current increases from bottom curve (I = 29 μA) to top curve (I = 450 μA); (b) Plot of the amplitude of 1/f noise $A$ versus $V^2$ for $E_{1.0}$ sample.

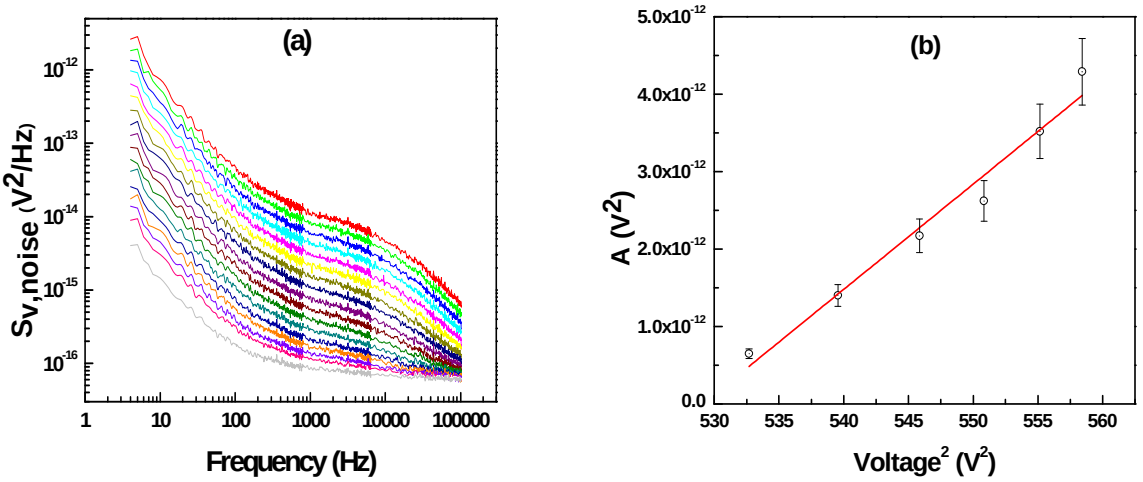


Figure 5.7. (a) Noise voltage spectra for $E_{0.8}$ sample for various bias currents. The bias current increases from bottom curve (I = 29 μA) to top curve (I = 660 μA); (b) Plot of the amplitude of 1/f noise *A* versus $V^2$ for $E_{0.8}$ sample.

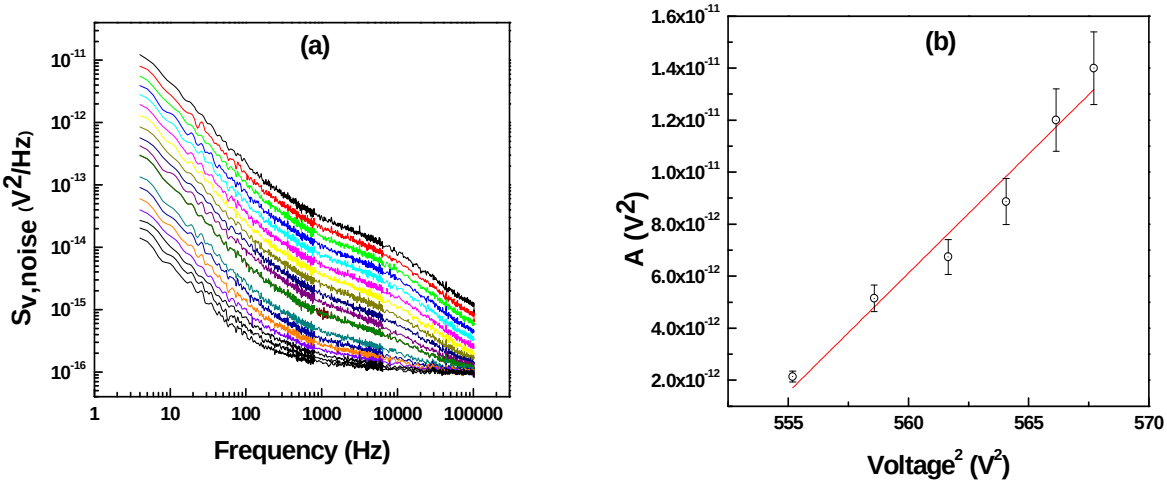


Figure 5.8. a) Noise voltage spectra for E0.5 sample for various bias currents. The bias current increases from bottom curve (I = 29 μA) to top curve (I = 1.05 mA); (b) Plot of the amplitude of 1/f noise *A* versus $V^2$ for $E_{0.5}$ sample.

Figure 5.9 presents Hooge parameter as function of measured electron mobility.

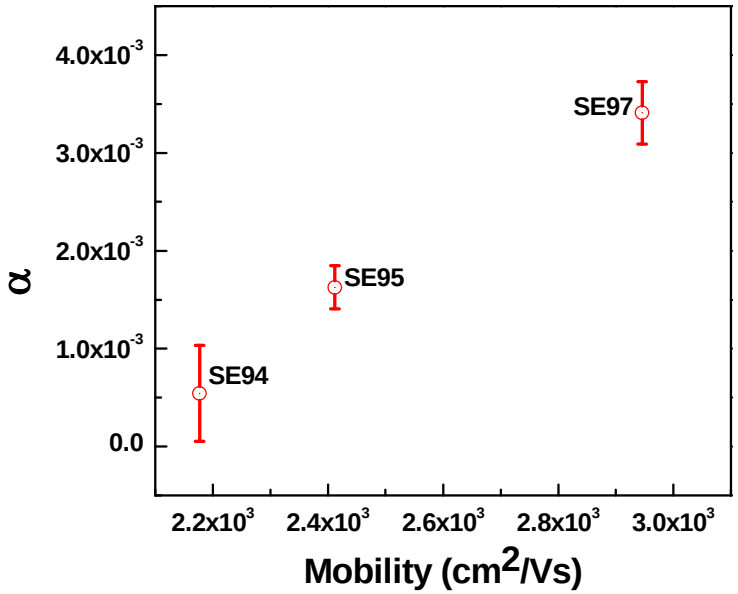


Figure 5.9. Dependency of the Hooge parameter versus the electron mobility for three GaAs QW samples with different doping in the barriers.

The dependence of the Hooge parameter versus measured free carrier concentration (by the Hall effect) is shown in Figure 5.10. There was a clear decrease of the Hooge parameter with the increasing number of free carriers in the device. The Hooge parameter was expected to be about the same for all three samples assuming the same crystal quality. However, the opposite behavior was observed. In order to clarify this question further, detailed studies were required. It was assumed that the measured difference in the Hooge parameter was caused by contact resistance, as is known that the noise from the contacts is much higher compared to the bulk noise. The studies of contact resistance in Section 4.2 indicated that the contact resistance for the lowest doped sample is the highest, while it is the lowest for the highly doped sample (see Figure 4.8). Even after applying the four-probe technique for measurements, the noise of the contacts was believed to have an additional influence on the measured total noise. This could explain the 2 to 3x difference in the measured Hooge parameter from sample to sample. More detailed

studies of this question are required using the transmission line model (TLM) and is considered in the discussion of future work.

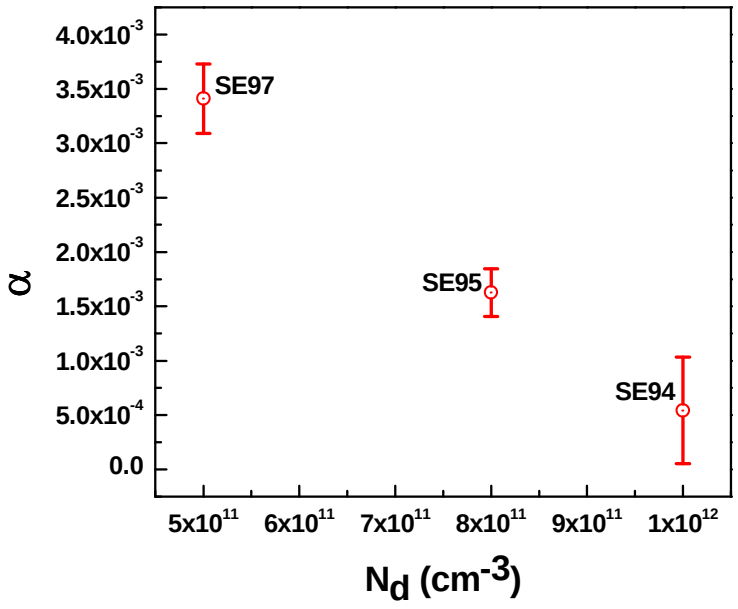


Figure 5.10. Dependency of the Hooge parameter versus the dopant concentration for three GaAs quantum well samples.

5.3.4. Generation-Recombination Noise and Impurity States in AlGaAs Barriers

The measurements to investigate the generation-recombination noise were done at the temperature range of 390 K to 82 K. These measurements allowed characterization of materials on the presence of traps, find their activation energies, and energy location in the band gap of the semiconductor. The analysis used the process described in Section 4.2.

As it was previously mentioned in Section 5.2, there are two possible forms of how to present the noise spectrum (see Figure 4.4); and, as previously stated, these two forms of the noise spectrum are equivalent.

The first step to analyze the noise data of the trap and impurity states was to plot the data in two forms. From the experiment it was possible to directly obtain the dependence of the voltage noise spectrum density $S_{v,noise}$ versus the frequency $f$ for each specific temperature.

After that, the experimentally measured spectrum $S_{v,noise}(f)$ was transformed into the normalized noise spectrum density $S_{,noise}(T)$, where $S_{noise} = S_{V,noise} / V^2$ .In order to do that, a number of procedures were performed:

(1) Fourteen different frequencies were chosen from the whole measurement frequency range.

(2) For each frequency, the voltage noise spectral density was extracted at each temperature.

(3) The noise voltage spectral density was divided by the voltage $V$ across the device [$V=24*R_s/(R_L+R_s)$, where $R_s$ is the sample resistance at certain temperature, $R_L$ is the value of the load resistor (24 is the measured voltage of the battery).

(4) These data sets were plotted as $S_{noise}(T)$ versus temperature and frequency.

This step was repeated for each sample in order to achieve two types of spectra for further analysis. The results of this analysis are shown in Figures 5.11 – 5.15.

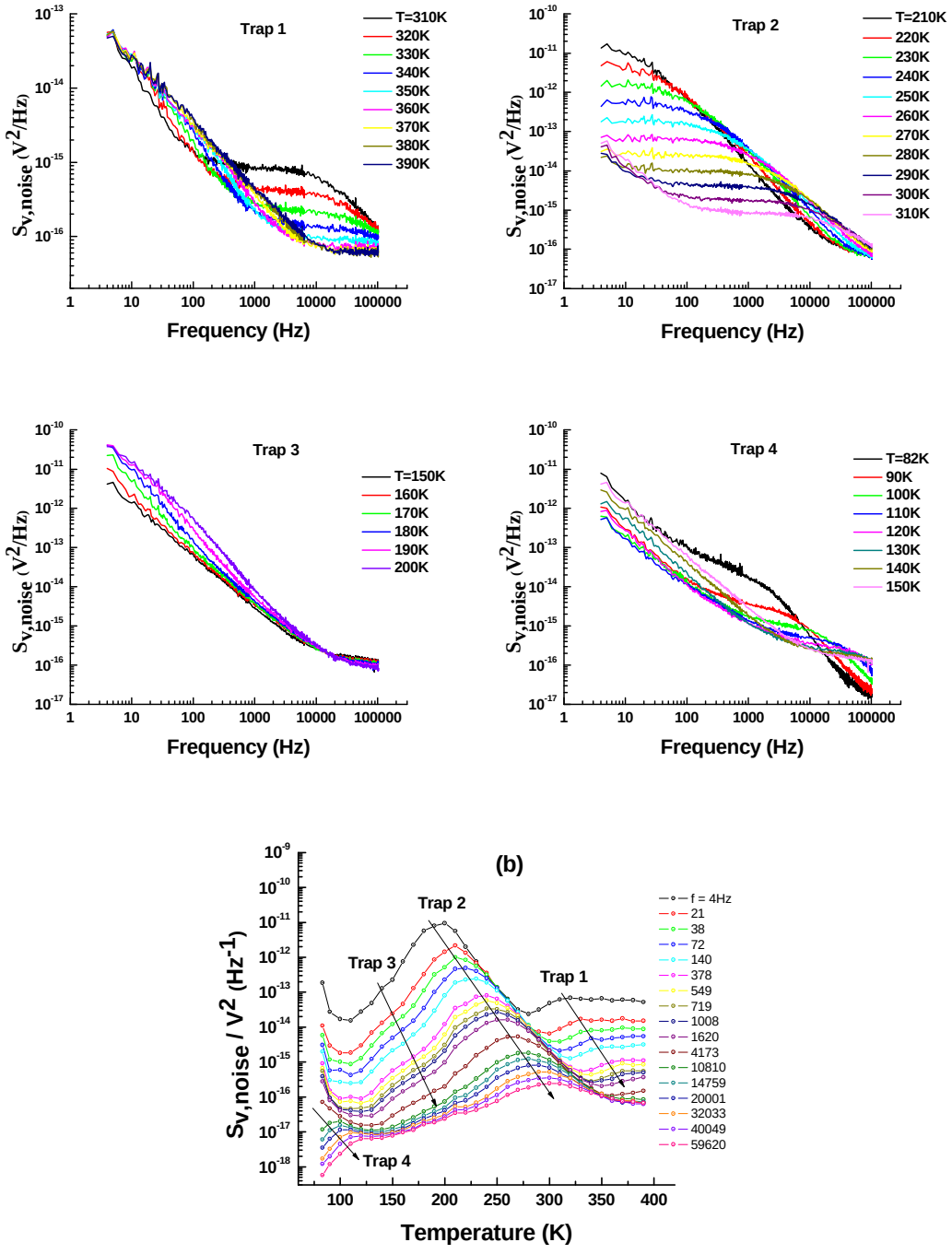


Figure 5.11. (a) Measured voltage noise spectral density for $REF_U$ sample. The spectra are shown in different temperature ranges as four separate graphs to distinguish presence of four different traps. Each trap is detected as unique generation-recombination process in for certain temperature range, (b) noise spectral density $S_{noise}$ versus temperature $T$ and frequency.

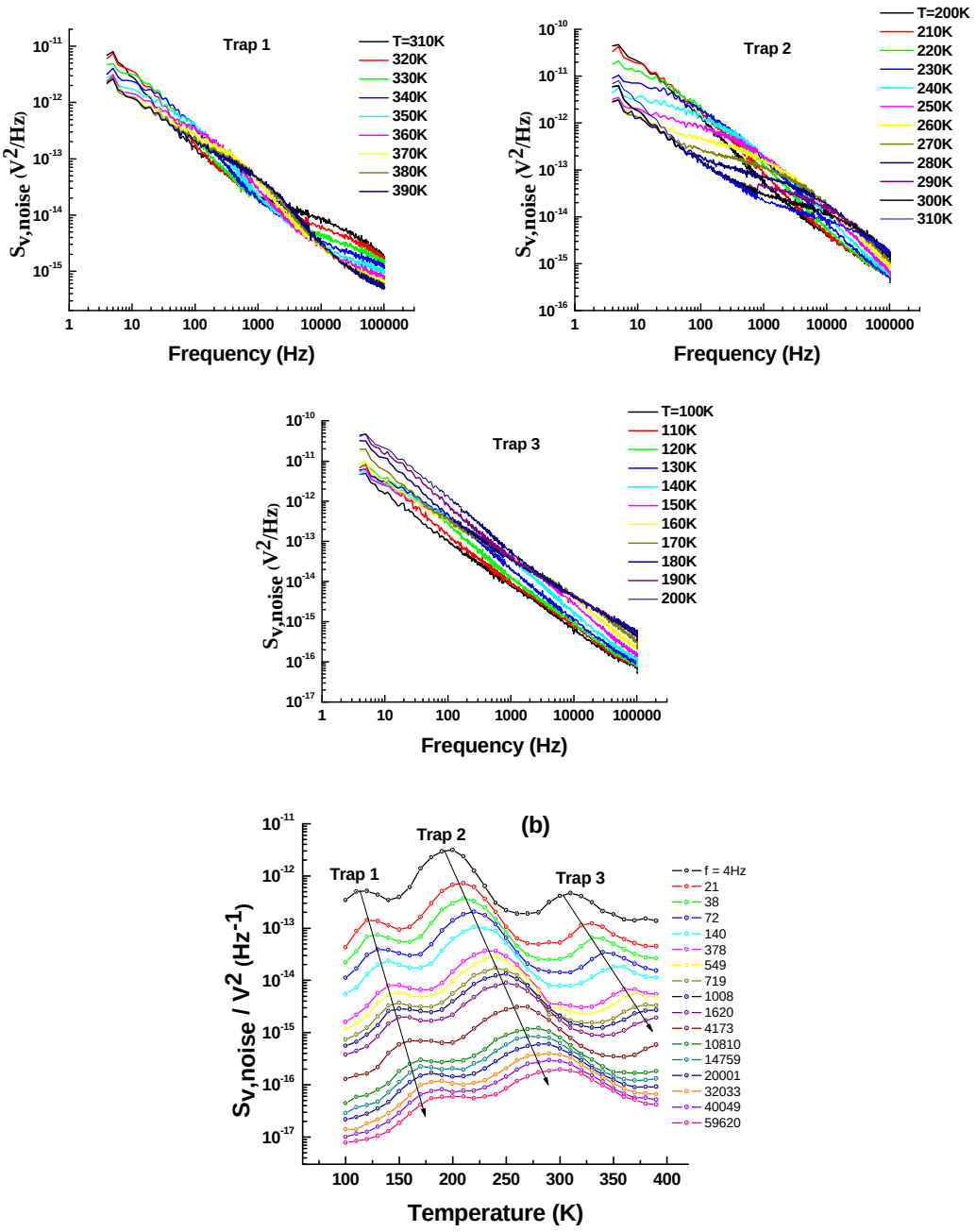


Figure 5.12. a) Measured voltage noise spectral density for $E_{1.0}$ sample. The spectra are shown in different temperature ranges as four separate graphs to distinguish presence of three different traps. Each trap is detected as unique generation-recombination process in for certain temperature range, (b) noise spectral density $S_{noise}$ versus temperature $T$ and frequency.

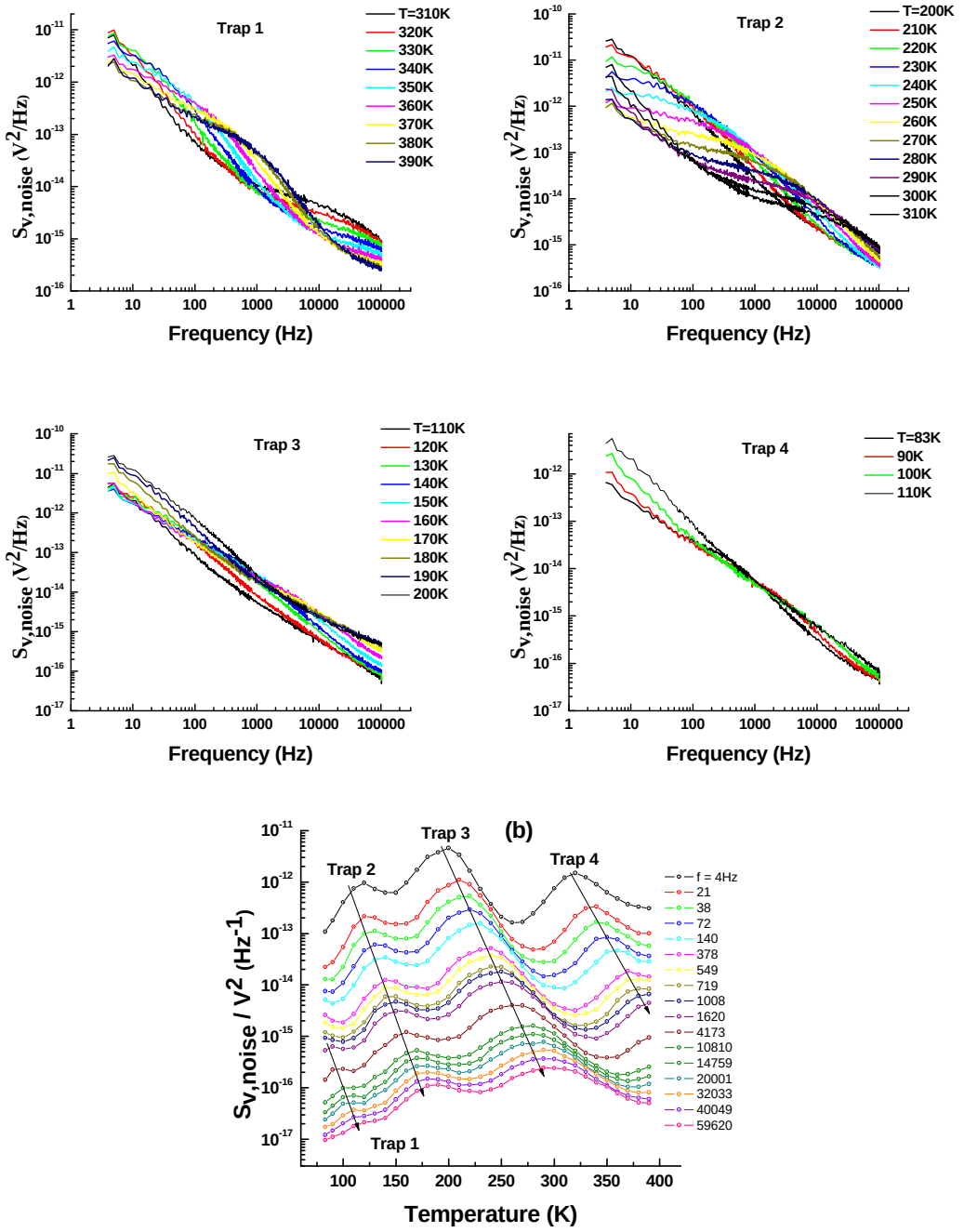


Figure 5.13. a) Measured voltage noise spectral density for $E_{0.8}$ sample. The spectra are shown in different temperature ranges as four separate graphs to distinguish presence of four different traps. Each trap is detected as unique generation-recombination process in for certain temperature range, (b) noise spectral density $S_{noise}$ versus temperature $T$ and frequency.

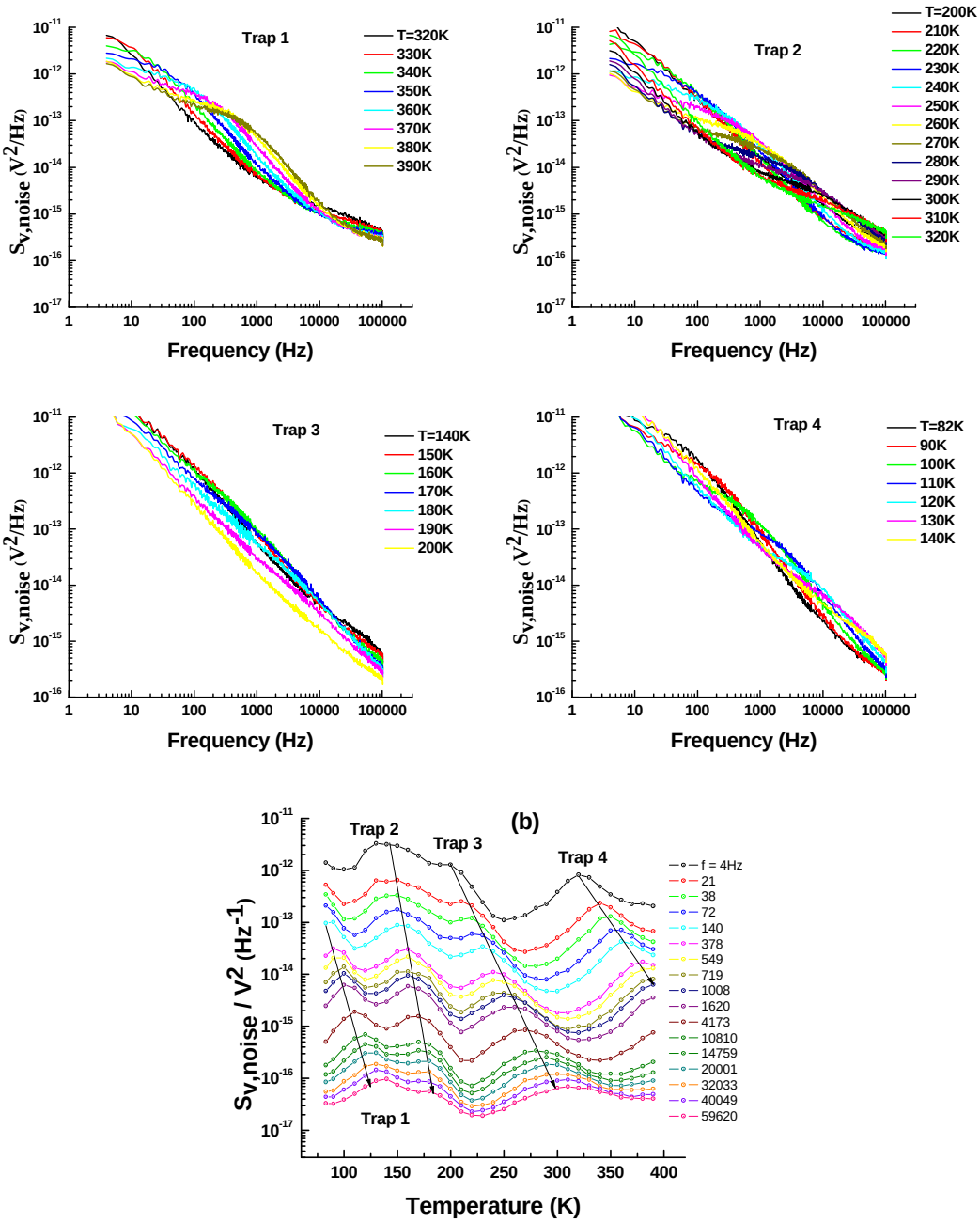


Figure 5.14. a) Measured voltage noise spectral density for $E_{0.5}$ sample. The spectra are shown in different temperature ranges as four separate graphs to distinguish presence of four different traps. Each trap is detected as unique generation-recombination process in for certain temperature range, (b) noise spectral density $S_{noise}$ versus temperature $T$ and frequency.

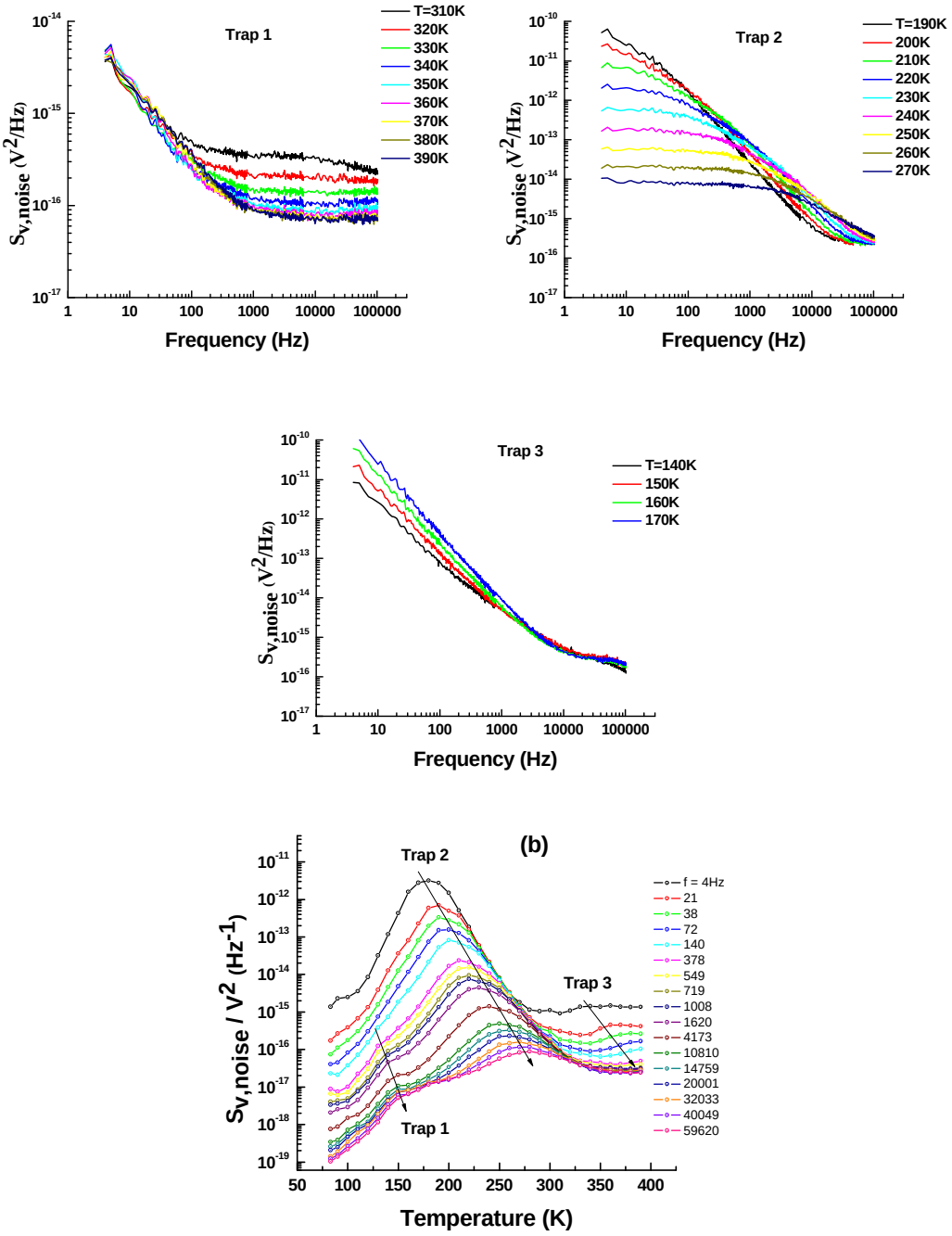


Figure 5.15. a) Measured voltage noise spectral density for $REF_{\delta}$ sample. The spectra are shown in different temperature ranges as four separate graphs to distinguish presence of three different traps. Each trap is detected as unique generation-recombination process in for certain temperature range, (b) noise spectral density $S_{noise}$ versus temperature $T$ and frequency.

Despite the fact that both of the forms presented in the figures above are based on the same data set, the figure (b) in each graph visually gives more information about the sample and

number of traps in the structure. Also, figure (b) is more interference resistant [55], and the maxima in the graph, which corresponds to different defects, can be detected.

The next step was to analyze the $S_{noise}(T)$ spectra to determine the activation energy of each deep level. This analysis was done as a number of different steps:

(1) Each curve $S_{noise}(T)$ for each frequency was plotted individually.

(2) The amplitude of the noise signal was extracted for each maximum and the temperature at which the maximum occurs was determined (this procedure was done for each curve individually).

(3) Based on this data, for the noise signal $S_{max}$ and temperature $T_{max}$, two different graphs were plotted. The first one was the dependence of $1/k_bT_{max}$ versus the natural logarithm of the frequency $\ln(2\pi f)$. The second one was the dependence of the natural logarithm of the noise signal $\ln(S_{max})$ versus the natural logarithm of the frequency $\ln(2\pi f)$.

(4) The technique described in Section 4.2 was applied.

The details of the analysis of the $S_{,noise}(T)$ spectra to determine the physical parameters of deep states are presented in Appendix A.

Table 5.1 presents the summarized data on calculations of the activation energy $E_1$ and the energy location of the deep state in the band gap $E_0$.

Table 5.1. Trap characteristics for all samples used in this study.

| | **$REF_U$** | **E1.0** | **E0.8** | **E0.5** | **$REF_\delta$** |
|---|---|---|---|---|---|
| $N_d$ ($cm^{-3}$) | $1x10^{17}$ | $1x10^{12}$ | $8x10^{11}$ | $5x10^{11}$ | $1x10^{17}$ |
| *Structure Type* | Uniformly doped | δ-doped | δ-doped | δ-doped | Multiple δ-doping |
| **Trap1(High Temperature)** | | | | | |
| $tan(\Theta_S)$ | 0.91 | 0.94 | 0.99 | 0.85 | 0.82 |
| $tan\ (\Theta_T)$ | 1.02±0.11 | 1.19±0.05 | 1.09±0.08 | 1.27±0.19 | 1.17±0.15 |
| $E_1$ (meV) | 994±95 | 849±35 | 917±24 | 785±33 | 843±88 |
| $E_0$ (meV) | 81 | | 12 | 115 | 160 |
| **Trap2** | | | | | |
| $tan(\Theta_S)$ | 1.11 | 1.02 | 1.04 | 1.03 | 1.12 |
| $tan\ (\Theta_T)$ | 2.16±0.02 | 2.02±0.05 | 1.97±0.06 | 2.21±0.04 | 2.54±0.01 |
| $E_1$ (meV) | 463±5 | 494±15 | 507±12 | 455±14 | 395±7 |
| **Trap3** | | | | | |
| $tan(\Theta_S)$ | 1.06 | 0.97 | 0.95 | 1.18 | 0.98 |
| $tan\ (\Theta_T)$ | 2.75±0.45 | 3.98±0.2 | 3.86±0.31 | 2.51±0.23 | 2.62±0.41 |
| $E_1$ (meV) | 358±49 | 253±7 | 259±11 | 399±17 | 384±48 |
| **Trap4 (Low Temperature)** | | | | | |
| $tan(\Theta_S)$ | 0.66 | – | 0.89 | 1.15 | – |
| $tan\ (\Theta_T)$ | 15.68±1.01 | – | 10.64±1.15 | 7.64±0.98 | – |
| $E_1$ (meV) | 62±7 | – | 94±12 | 131±21 | – |
| $E_0$ (meV) | 23±6 | – | | | – |

5.3.5. Generation-Recombination Noise Results Discussion

As stated earlier, samples $REF_U$ and $REF_\delta$ were used as the reference samples in this work. The other samples, $E_{1.0}$, $E_{0.8}$, and $E_{0.5}$, which were QWs heterostucture samples, were compared to the reference samples in order to identify defects and their spatial location in the

volume of the device. In other words, the goal was to experimentally probe defect states in the AlGaAs barrier where a real space charge transfer from the high mobility GaAs quantum well to the impurity/defect band was expected.

For the uniformly doped $REF_U$ reference sample, the results of the noise studies are presented in Figure 5.11. Four distinct peaks were detected. These four peaks corresponded to four different traps that were present in the bulk AlGaAs layer. The temperature ranges of 310K – 390K, 200K – 310K, 150K – 200K, and 83K – 150K corresponded to traps 1, 2, 3 and 4, respectively. The technique that was described in Section 4.2 of this chapter was used to characterize these traps and to find their energy location $E_0$. The results of this analysis are presented in Table 5.1. By analyzing the slope extracted from the plots of the natural logarithm of the noise signal $\ln(S_{max})$ versus the natural logarithm of the frequency $\ln(2\pi f)$, the slopes were found to be equal to 0.91, 1.11, 1.06, and 0.66 that correspond to traps 1, 2, 3, and 4, respectively. According to the theory presented in [55], for trap 4 it was possible to find both energies $E_0$ and $E_1$. For this trap, the Fermi energy was above the trap level according to our Hall effect measurement results. This meant that condition $E_1 > E_0$ was satisfied. As it can be seen in Table 5.1, the energy $E_1$ was found to be 62 meV and $E_0$ was equal to 23 meV. For traps 2 and 3 the slope was about 1 and, according to [22], only energy $E_1$ could be calculated. The energy $E_1$ was found to be equal to 463 meV for trap 2, and 358 meV for trap 3. For trap 1, the Fermi level was located above the trap level, based on Hall effect measurements performed for high temperatures. Hence, it was possible to calculate the activation energy, $E_1$ = 994 meV, and energy of the deep level, $E_0$ = 81 meV.

For another reference sample $REF_\delta$, the same measurements were performed, and the results of the analysis are presented in Figure 5.15 and in Appendix A. Only three traps were

detected for this sample. For trap 2 and trap 3, the slopes of the dependencies of the natural logarithm of the noise signal ln($S_{max}$) versus the natural logarithm of the frequency ln($2\pi f$) were found to be ~1 and only the activation energies $E_1$ could be calculated. For trap 2 it was found that the activation energy $E_1$ was equal 384 meV, and for trap 3 the activation energy was $E_1$ = 395 meV. The estimated activation energies for trap 3 in sample $REF_U$ and sample $REF_\delta$ were very close to each other. However, for trap 2 the activation energy for $REF_\delta$ sample was about 15% smaller compared to the activation energy of $REF_U$ reference sample. This trap dominated over the same wide temperature range (above 100 K) for both samples. The difference in activation energies measured for these two samples could be due to different doping designs (multiple δ-doping vs. uniform doping). Trap 1 was detected at high temperatures for both sample REFU and REFΔ. However, for sample $REF_\delta$ this trap was detected only at low frequencies. At high frequencies, detection of this trap was obscured by dominant white noise. The activation energy $E_1$ was found to be equal to 843 meV, and this energy was lower than the activation energy $E_1$ measured for the REFU sample. This discrepancy was believed to be due to the limited accuracy of the measurements (Table 5.1) for this high temperature peak. However, the physical origin of this defect was believed to be the same. The measurement accuracy of $E_1$ explains the difference in estimation of $E_0$ for the same trap.

After analyzing the reference samples $REF_U$ and $REF_\delta$, those results were compared to the data received after analysis of the noise measurements that were performed for the AlGaAs/GaAs QW heterostructures ($E_{1.0}$, $E_{0.8}$, and $E_{0.5}$ samples). The noise spectra are shown in Figures 5.12– 5.14 and the results of the analysis are given in Table 5.1. Also, plots of the dependence of the natural logarithm of the noise signal ln($S_{max}$) versus the natural logarithm of

the frequency ln($2\pi f$), and $1/k_bT_{max}$ versus the natural logarithm of the frequency ln($2\pi f$) are shown in Appendix A.

From Figure 5.12, it can be seen that sample $E_{1.0}$ had three traps. These three traps were detected as the generation-recombination noise at different temperatures. The same generation-recombination noise was also detected in reference samples for the same temperature ranges. Based on the noise spectra analysis and the comparison of this data to the data analysis performed for reference samples, it was concluded that all these traps were located in the $Al_{0.3}Ga_{0.7}As$ barriers. By comparing these results to previously published data in [69], it was concluded that trap 2 was the DX center that is located in the AlGaAs barrier. The activation energy of trap 1 was in good agreement with the reference sample REFδ (see Table 5.1). At low temperature, trap 4 was not observed in $E_{1.0}$ and $REF_{\delta}$ samples. However, as it will be shown in the next chapter, this trap plays an important role in the real-space charge transfer and can be detected by noise spectroscopy when the Fermi level is at resonance with the trap 1.

The noise spectra for the other two QW samples ($E_{0.8}$ and $E_{0.5}$) were also analyzed and compared to the reference samples. Four traps were detected, as in case of the reference sample $E_{1.0}$. The details of the analysis are presented in Table 5.1 and the corresponding plots are given in Appendix A.

# Chapter 6. Pulsed I-V Measurements

In this chapter the pulsed current-voltage experiments are described that resulted in the negative differential resistance phenomena measurements. To understand better the origins of NDR, additional experiments were performed with a light excitation and with exposure to high temperatures of the quantum well heterostructure. All pulsed I-V measurements were performed at 82 K. Experiments with light and temperature proved that present system is reversible, and after the real space charge transfer happened, the system can be returned to its initial state by light excitation using band-to-band illumination or by exposure to high temperatures.

In addition, in this chapter noise measurements executed using lock-in technique before and after the real space charge transfer happened are presented. This technique allowed direct insight on impurity states in AlGaAs barriers before and after real space carrier transfer. In addition it allowed ideas about carrier kinetics between deep states in the AlGaAs layer to be proven.

## 6.1. I-V Measurements in the Dark

The pulsed I-V measurements were done using experimental setup shown in Figure 6.1. The FET like device structure (see Figure 4.11a) was used for it.

The voltage pulses with length of 1 ms were applied to avoid heating effects of the sample. Therefore, according to [70] heating effects would be negligible.

After the sample was mounted into the cryostat the system was cooled to 82 K. At this temperature I-V measurements were done, and the experimental results are depicted in Figure 6.2a. As it is seen in Figure 6.2a, with applying of low voltage the linear behavior was measured as it was expected for ohmic region. However, at voltage around 1.3 V the current reached its maximum, and with further applying of higher voltages this current went down and the region of

NDR was observed. At around 2.9 V the decrease in current had stopped, as the majority of electrons in the quantum well were transferred to AlGaAs barriers.

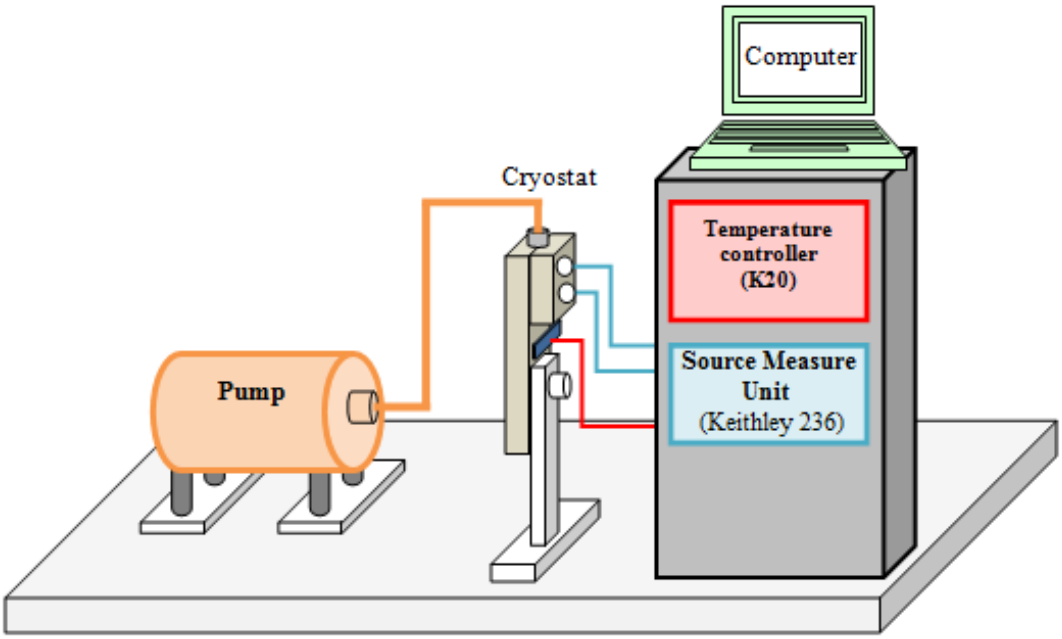


Figure 6.1. The experimental setup for pulsed I-V measurements.

Hence, with further increasing of voltage the increase in current was observed but with lower speed (smaller slope of the curve) that can be explained because of lower mobility of the layer where the real space charge transfer effect occurred. After that, the same experiment at same conditions was repeated (see run 2, I-V curve in Figure 6.2a). It can be seen that the maximum current in the device channel was reached at about 4 V, which is very different from the first run. The linear behavior of the current with voltage increase at low biases was not observed at this time. Nevertheless, it was possible to see that the value of current where the peak was detected was within 0.1% difference, and with further increasing of voltage the NDR was achieved (not shown in this figure). This change in I-V behavior is believed to be a result of the electron transfer, where some number of electrons got trapped into the available states of the AlGaAs barriers. As a result of this decrease in number of electrons available for conduction, the channel

resistance increased. On the other hand, the same value of current peak and NDR were observed. That suggested that electron transfer occured from the high-mobility GaAs channel into the impurity states of the AlGaAs barrier.

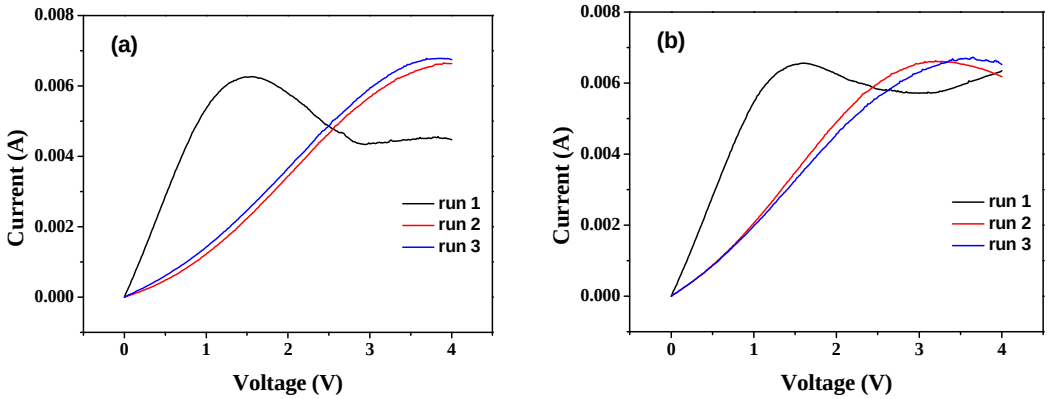


Figure 6.2. I-V measurement curves for $E_{1.0}$ sample (a) at 82 K after the sample was cooled down; and (b) after temperature of device was increased up to 390 K and then cooled down to 82 K.

At this point, the experimental data demonstrated that the electron transfer took place. However, in order to prove that electrons were transferred into the available states in the AlGaAs barriers experiments with temperature change and with exposure of the sample to light were performed separately.

After the third run at 82K, the temperature of FET like device was increased to 390 K and was kept for 20 min. The heating cycle was done in order to recharge the quantum well / impurity system by freeing the electrons from the shallow trapped states of the AlGaAs and to collect free electrons in the GaAs quantum well. Afterwards, the sample was cooled back to 82 K and I-V measurements were performed. The results of I-V measurements after the thermal cycle were depicted in Figure 6.2b. It was seen that the system returned to the original state, but with some difference in the peak value of current saturation peak and smaller NDR region. The other two runs exhibited the same behavior as was observed previously. This experiment suggested

that the present system could be recharged and could be brought into the original state with one temperature cycle. So, it was concluded that the thermal energy of 34 meV ($k_bT$ at 390 K) was high enough to recharge the system. Based on that, it was suggested that real space charge transfer happened mainly into the shallow states in the AlGaAs barriers. According to this system design, the shallow states were the shallow donor states due to Si δ-doping in AlGaAs barriers.

In addition to temperature cycling experiments, the band-to-band light excitation was applied to the present system.

### 6.2. I-V Measurements with Exposure to Light

The pulsed current-voltage measurements were repeated after exposure of the quantum well heterostructure to light. These measurements were done in a similar manner as the measurements performed in the dark. In this set of experiments the system was recharged using the light with λ = 514 nm. The schematic of the experimental setup for I-V measurements with exposure to light is shown in Figure 6.3.

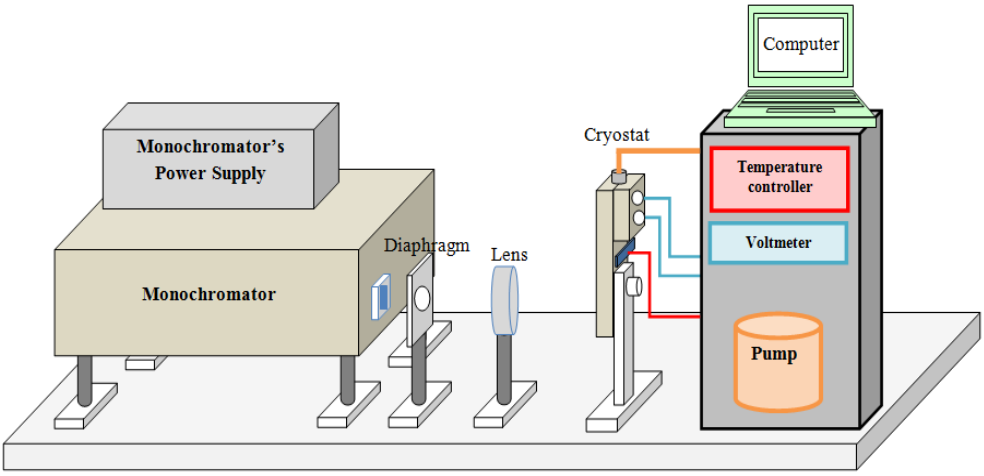


Figure 6.3. The experimental setup for I-V measurements with exposure to light.

In this setup, the computer controlled 9055 Czerny-Turner monochromator, the power supply for the monochromator, an adjustable diaphragm, and the focusing lens to concentrate the light onto the device pattern were used.

After the sample was cooled down to the 82 K and high electric field was applied (4 V corresponds to an electric field across the device of about 2.5 kV/cm), in order to recharge the system, the light excitation with $\lambda$ = 514 nm was done. To control the system response to the light excitation, the device channel resistance was measured. The sample was exposed to band-to-band light until the resistance of the sample reached the minimum stable value. After the resistance saturated, the light was turned off and the window on the cryostat was closed. After waiting until the resistance of the device saturated after slow increase, the pulsed I-V measurements were executed again. These I-V measurements are shown in Figure 6.4.

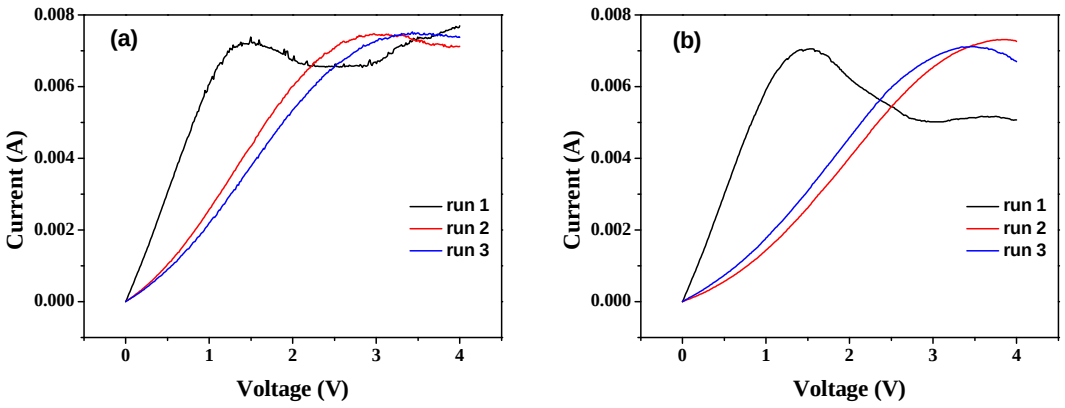


Figure 6.4. I-V curves for $E_{1.0}$ sample after exposure to light ($\lambda$ = 514 nm): (a) after first exposure, (b) after second exposure.

According to these data the quantum well system was brought to the initial state. I-V measurements for this sample for runs 2 and 3 are depicted as well. Similar behavior was measured as it was before light excitation (see Figure 6.2b). A second light exposure at the same wavelength and intensity is shown in Figure 6.5b. Again, the device returned to its initial state.

As it can be seen in Figures 6.4a and 6.4b, the voltages at which current saturated and reached its maximum value were the same. Nevertheless, the value of current saturation was different. The density of the current in the device channel can be expressed as $J=en\upsilon_d$, where $e$ is the elementary electron charge, $n$ is the number of carriers, and $\upsilon_d$ is the drift velocity. It was reasonable to assume that the maximum value of current in the device could be achieved with maximum $n$ in the quantum well channel, where the quantum well was considered as the main channel of conduction. By exposure of the quantum well heterostructure to high temperature or band-to-band illumination, the charges trapped on the shallow donor levels and/or deep levels were released and returned back to the quantum well. Taking into consideration that the energy of the light was much higher than the thermal energy that electrons could receive from a heating cycle, it became evident that higher value of channel current after light excitation was measured simply because of higher number of released carrier from deep traps into the GaAs quantum well (see Figures 6.2 and 6.4).

However, in order to explain where the electrons were transferred the noise measurements were made using a lock-in technique. The $E_{1.0}$ sample was chosen for these types of experiments because of its good experimental characteristics based on the previous experiments.

### 6.2.1. Lock-in Technique

The main idea of the noise measurements using lock-in technique was to detect traps under certain excitation conditions by measuring the noise signal as a function of temperature at constant frequency across the Greek cross device. The noise signal was measured between two contacts and a small bias current was applied to another pair of contacts. These measurements were done for $E_{1.0}$ sample, which happened to have the best I-V curves with the most significant

NDR region that was observed among all samples. The experimental setup for noise signal measurements using lock-in technique is shown in Figure 6.5.

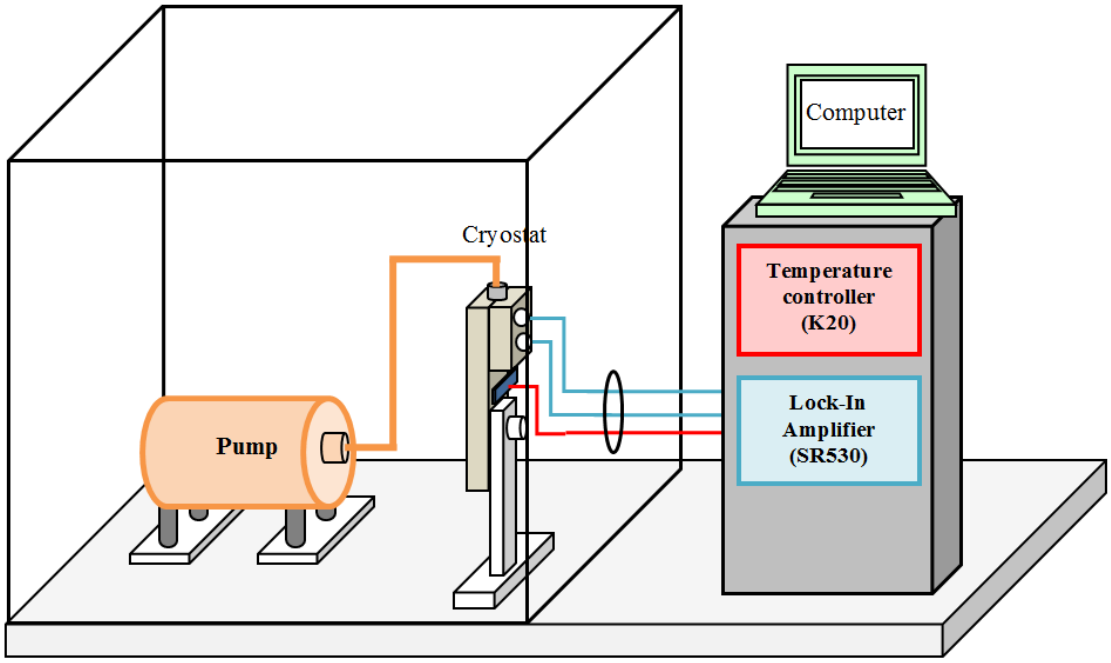


Figure 6.5. The experimental setup for noise signal measurements using lock-in amplifier.

All measurements were performed at constant frequency of 135Hz and the results can be seen in Figure 6.6.

The very first step, the results of which are depicted in Figure 6.6a, was to measure the noise signal as a function of temperature after the sample was cooled to 82 K. Three traps were detected in $E_{1.0}$ sample, which were the same as were previously found for the same sample using DLNS technique.

The second step was to cool the sample again from 400 K to 82 K and perform the same experiments as they were done in the first step. However, before performing the noise signal measurements the voltage across the device was pulsed from 0 to 5.5 V with 0.01 V step size. The experimental results are shown in Figure 6.6b. As it was expected, three traps were

observed. Furthermore, one additional peak that corresponded to trap 4 was also observed. From comparison data in Figures 6.6a and 6.6b, it was seen that the amplitudes of trap 2 and trap 3 remained the same. Also, it was noted that the amplitude of trap 1 decreased almost by 30%.

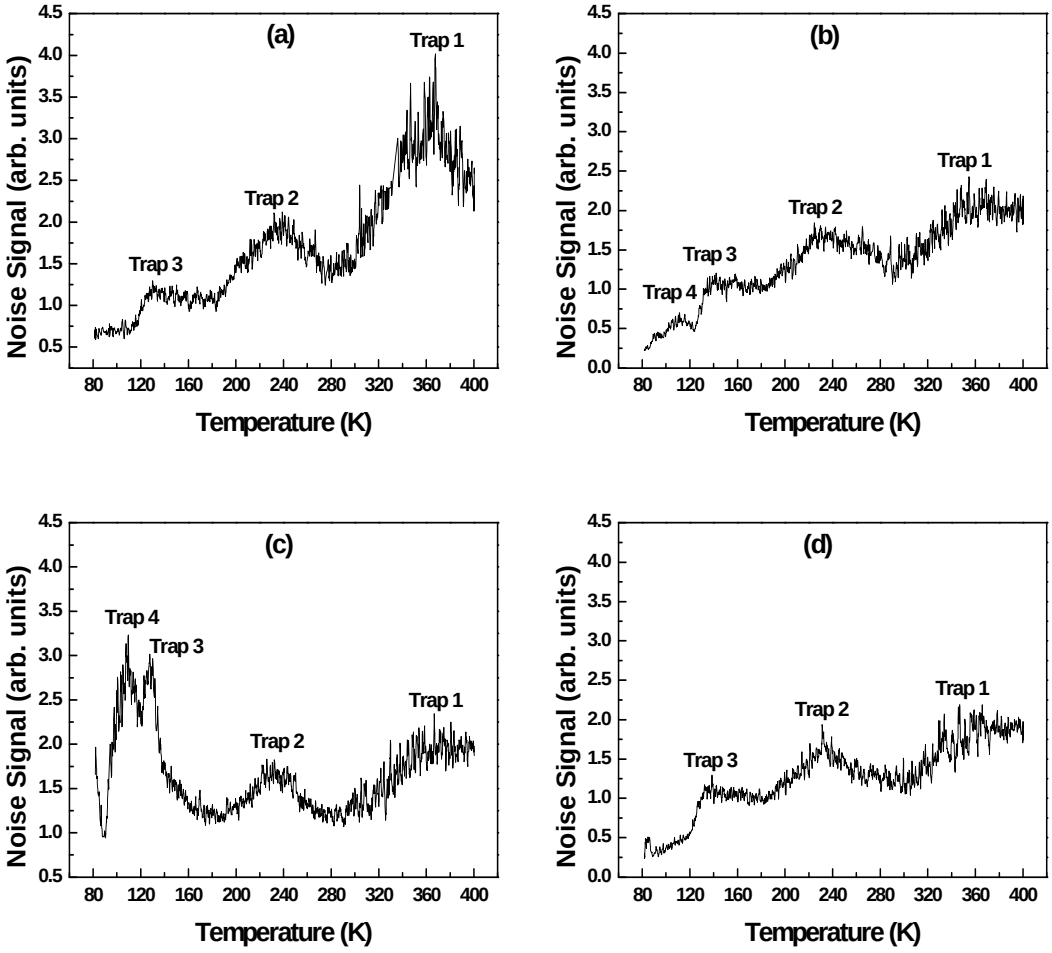


Figure 6.6. Noise signal measurements using lock-in amplifier for sample $E_{1.0}$; (a) after cooling down to 82 K, (b) after applying of 5.5 V, (c) after applying of 8 V, (d) after the light exposure ($\lambda$ = 514 nm).

After that the sample was cooled again to 82 K. At this temperature $E_{1.0}$ sample was exposed to light ($\lambda$ = 514 nm) in order to bring the system to its initial state. Afterwards the voltage from 0 to 8 V in pulsed mode was applied to the sample. The noise signal measurement results are depicted in Figure 6.6c. The amplitude of trap 3 increased more than twice, and the

amplitudes of trap 1 and trap 2 remained the same as for the previous step. Also, it was seen that the amplitude of trap 4 dramatically changed and reached its maximum. This change was due to the real space electron transfer.

According to these studies (see Figure 6.8), trap 4, which was not detected in the $E_{1.0}$ sample before system was exposed to high electric field, was associated with the band of the ionized Si impurities. This band was formed as a result of Si remote δ-doping. All free electrons confined in the quantum well were the electrons that were ionized from the donor states of the Si atoms in AlGaAs barriers. Hence, this Si δ-doping band had enough available states in the AlGaAs barrier, which were allowed for electron transfer at applied high electric fields (real space charge transfer). As the result of this transfer the resistance of the sample increased. With more electrons transferred to those states, the Fermi energy became in resonance with the Si impurity band. Consequently, the amplitude of trap 4 density of noise reached its maximum. It is commonly accepted that generation-recombination process starts to play a dominant role in the noise spectrum when the Fermi energy is in resonance with trap level [65]. Based on these noise studies and previous DLNS studies, it was concluded that during the filling process of the traps by charges, the kinetic processes were involved, i.e. traps “talked” to each other. Because of small change of noise amplitude for trap 2 and trap3, it was suggested that these were intermediate traps with an ability to capture and release carriers quickly. That meant that the life time of electrons on these traps would be short. However, the previously described case was only valid when the impurity band (trap 4) was filled partially. Hence, after applying 8 V to the sample the trap 4 became full enough that the noise signal of trap 3 became dominant.

It is worth to mention here that after each step the Hall effect and I-V measurements were performed in order to get better understanding of the carriers' behavior, and also to create a whole picture of electrons transfer.

As a final step, the sample was exposed to light but no high electric field was applied across the device. The results of noise signal measurement for this step can be seen in Figure 6.6d, and were in very good agreement with Figure 6.6a. The low temperature trap 4 was not present anymore in the noise spectra. However, the amplitude of high temperature trap 1 decreased. It could be due to the difference of the charge state of trap 1 because light excitation was able to recharge trap 1 more efficiently than temperature can in the case represented in Figure 6.8a.

## Chapter 7. Conclusions

Using solid source molecular-beam epitaxy (MBE) Riber 32P system five different samples were grown. Two of them were grown as the reference samples. The first reference sample ($REF_U$) was prepared as 1.5 μm thick $Al_{0.3}Ga_{0.7}As$ epi-layer with Si uniform doping ($N_d = 1\times10^{17}$ $cm^{-3}$). The second reference sample ($REF_\delta$) was prepared in the similar manner, but instead of uniform doping multiple Si δ-dopings were introduced to achieve the same doping density of $N_d=1x10^{17}cm^{-3}$ as for sample $REF_U$. The three last samples were prepared as the quantum well heterostructures. Two symmetrical remote Si δ-dopant layers were located in $Al_{0.3}Ga_{0.7}As$ barriers and separated by 5 nm AlGaAs spacers from 10 nm thick GaAs quantum well. The number of free carriers in the quantum well heterostructure $N_{2D}$ was varied by dopant densities in the AlGaAs barriers: for sample $E_{1.0}$ $N_{2D}=1x10^{12}cm^{-2}$/per layer, for sample $E_{0.8}$ $N_{2D} = 8x10^{11}cm^{-2}$/per layer, and for sample $E_{0.5}$ $N_{2D}=5x10^{11}cm^{-2}$/per layer.

By applying the Hall effect measurements it was possible to obtain the experimental data on electron mobility and carrier density for all samples. The theory of Hall effect measurements and scattering phenomena in bulk materials and AlGaAs/GaAs quantum well heterostructures were briefly discussed and provided some insight on the experimental data. As it was expected the mobility in QWs was much higher than in bulk materials which proved the possibility of its application in high-speed electronics. For all QW heterostructures the electron mobility experienced increases with decreasing of temperature. This increase in mobility was due to the reduced scattering on the phonons as a result of temperature decrease. Further temperature decreases resulted in reduction of phonon scattering and enhanced scattering on ionized impurities. That is why at temperature about 100 K the mobility curve had a peak and even some decrease at low temperatures for each QW sample. This decrease of the mobility has provided

first evidence that conduction of electrons happened in the high mobility quantum well and in the Si impurity band in parallel. Both bands were important to observe real space charge transfer at high electric fields. To prove this concept the measurements of the carrier concentration were used. The measured carrier density at moderate temperatures exhibited normal behavior for semiconductors, i.e. decreasing of carrier density with lowering temperature. However, at temperatures lower than 100 K, where the peak of the mobility was observed, an anomalous behavior was observed for carrier density, i.e. increasing of free carriers with decreasing of temperature. This increase was explained as a result of multi-band conduction effect through the GaAs quantum well and Si impurity band.

Standard photolithography techniques for patterning semiconductor materials were used to achieve the desired device structure. The ohmic contacts were fabricated using e-beam evaporation of the metals. By depositing AuGe/Ni/Au layers high quality ohmic contacts were achieved. To estimate the contact resistance the TLM technique was applied at room temperature. Furthermore, the temperature measurements of the contact resistance were done. These studies indicated that contact resistance increased with decreasing temperature. This fact was very important to fabricate high frequency devices to operate at low temperatures where contact resistance can have negative influence.

In addition to the Hall effect measurements the noise studies of the grown materials were applied to identify available deep states in GaAs quantum well heterostructures. The noise spectra were taken in the temperature range of 82 K to 390 K with 10 K stesp. Based on the experimental results it was seen that with increasing temperature the density of noise tended to increase as well. These measurements allowed identification of deep levels causing generation-recombination noise at certain temperatures. Four deep traps in the

AlGaAs/GaAs heterostructures were found. These traps were identified as deep levels in the AlGaAs barriers, based on the comparison of noise data for QW heterostructures and the AlGaAs reference samples. The activation energies of each defect were measured. The exact location of the deep trap below the conduction band gap was found only for some of them. The results of this analysis were presented in Table 5.1. Hence, by applying noise spectroscopy the impurity system was probed and studied in great detail. Using noise measurements as a function of applied electric field and by applying noise spectra modeling, the Hooge parameter was estimated for each heterostructure.

In order to observe the NDR phenomena the pulsed current-voltage measurements were done on FET like devices. The pulsed I-V measurements performed in dark at 82 K revealed the NDR in quantum well heterostructures. It was a proof of the real space charge transfer between the GaAs quantum well and AlGaAs barriers. However, at this step it was impossible to say where the electrons were transferred and what mechanism led to the NDR. To get more insight on the NDR mechanism temperature cycling and light excitation experiments were performed. Both experiments (temperature and light) proved that quantum well/impurity system could be recharged, i.e. returned to its initial state after charge transfer happened. Based on the fact that thermal energy of about 34 meV (for T = 390K) was enough to recharge this system to its initial state, it was concluded that the electrons transfer happen into the shallow level. That is why it was suggested that the most probable states where electrons can be transferred are ionized Si atoms in the δ-doping layers.

The experiments with light ($\lambda$ = 514 nm), similar to experiments at high temperatures, proved that quantum well/impurity system can be returned to its initial state and also the NDR can be measured again. Based on the experimental data it was shown that the threshold voltage

was the same after light excitation in all cases. However, the peak value of the current saturation was different. Hence, it was concluded that the maximum channel current depends on the number of free carriers in the quantum well. That is why with exposure this system to high temperatures or to band-to-band illumination, the number of the released free carriers from the deep trap states in AlGaAs and returned back to GaAs quantum well was different.

The last set of experiments was done to prove where the electron transfer happens in the quantum well/impurity system. The temperature dependent noise studies were done by using lock-in technique at fixed frequency in four probe geometry for sample $E_{1.0}$.

These temperature dependent noise experiments were performed for four different cases after: (1) system was cooled to 82 K and no electric field was applied; (2) at 82 K, the voltage of 5.5 V was applied (corresponding electric field was 484 V/cm); (3) at 82 K after the system was returned to its initial state by light illumination, the voltage of 8 V was applied (corresponding electric field was 705 V/cm); and (4) after system was recharged by light at 82 K to its initial state, the noise measurements were performed again. The sequence of these experiments allowed tracking of where the charge transfer had happened in the quantum well/impurity system. It was shown that free carriers from the quantum well are transferred mainly into the trap level located 22 meV below the AlGaAs conduction band, which was associated with Si impurity band (trap 4). The other three traps, 1, 2 and 3 participated in carrier capture as well. In addition, according to the amplitude distribution between traps in the noise spectrum, it was concluded that traps 2 and 3 were able to capture and release carriers faster than trap 1. Again, the excitation of sample with band-to-band illumination allowed to recharge system to its initial state and reproduce the noise spectrum of the GaAs/AlGaAs heterostructure as it was measured before application of any thermal, light or electric field excitation.

# Chapter 8. Future Work

For future work such aspects can be considered:

1. To perform more in deep analysis of Hooge's parameter using TLM technique.
2. To test the multi-band conductivity for this system by applying high magnetic fields at low temperatures (82 K). The Shubnikov-de Haas studies will be used.
3. Detailed studies of the defect states after light excitation and applying high electric field at different frequencies and temperatures have to be done. This will allow receiving quantitative characteristics of the defects and number of carriers traps to each defect separately.
4. To perform the I-V studies as a function of temperature in order to study NDR phenomena as a function of temperature.
5. To fabricate the FET transistor for high-frequency electronics and to measure its performance. The goal has to be to create a device that can perform at terahertz frequencies.

**References**


[1] M. Aust et al., “A 94-GHz monolithic balanced power amplifier using 0.1-μm gate GaAs-based HEMT MMIC production process technology,” IEEE Microwave and Guided Wave Letters, vol. 5, no. 1, pp. 12-14, Jan. 1995.

[2] P. M. Solomon and H. Morkoc, “Modulation-doped GaAs/AlGaAs heterojunction field-effect transistors (MODFET’s), ultrahigh-speed device for supercomputers,” IEEE Transactions on Electron Devices, vol. 31, no. 8, pp. 1015- 1027, Aug. 1984.

[3] N. Balkan, B. K. Ridley, A. J. Vickers, and N. A. T. O. S. A. Division, Negative differential resistance and instabilities in 2-D semiconductors. Springer, 1993.

[4] R. C. Dorf, The electrical engineering handbook: Sensors, nanoscience, biomedical engineering, and instruments. CRC. Press, 2006.

[5] S. M. Sze and K. K. Ng, Physics of semiconductor devices. John Wiley and Sons, 2007.

[6] S. M. Sze, Physics of Semiconductor Devices, 2nd ed. John Wiley & Sons, Inc., 1981.

[7] B. K. Ridley, “Specific Negative Resistance in Solids,” Proceedings of the Physical Society, vol. 82, pp. 954-966, Dec. 1963.

[8] M. Keever, “Measurements of hot-electron conduction and real-space transfer in GaAs-AlxGa1−xAs heterojunction layers,” Applied Physics Letters, vol. 38, p. 36, 1981.

[9] Z. S. Gribnikov, K. Hess, and G. A. Kosinovsky, “Nonlocal and nonlinear transport in semiconductors: Real-space transfer effects,” Journal of Applied Physics, vol. 77, p. 1337, 1995.

[10] B. R. Nag, Electron transport in compound semiconductors, vol. 11. Berlin: Springer-Verlag, 1980.

[11] “http://www.ioffe.ru/SVA/NSM/Semicond/GaAsSb/bandstr.html.” .

[12] J. B. Gunn, “Microwave Oscillation of Current in III-V Semiconductors,” Solid State Communication, vol. 1, no. 88, 1963.

[13] Z. I. Alferov, “The history and future of semiconductor heterostructures,” Semiconductors, vol. 32, no. 1, pp. 1-14, Jan. 1998.

[14] F. Rinaldi, “Basics of Molecular Beam Epitaxy (MBE),” Annual Report, Optoelectronics Department, University of Ulm, 2002.

[15] H. Ibach and H. Lüth, Solid-State Physics. Berlin, Heidelberg: Springer Berlin Heidelberg, 2010.

[16] J. H. Neave, B. A. Joyce, P. J. Dobson, and N. Norton, “Dynamics of film growth of GaAs by MBE from Rheed observations,” Applied Physics A Solids and Surfaces, vol. 31, no. 1, pp. 1-8, May 1983.

[17] K. F. Brennan and A. S. Brown, Theory of modern electronic semiconductor devices. New York: John Wiley & Sons, Inc., 2002.

[18] D. Miller, “Optical Physics of Quantum Wells,” 23-Jun-2011. Available: http://ee.stanford.edu/~dabm/181.pdf. [Accessed: 23-Jun-2011].

[19] C. Hamilton and J. Marsh, “Quantum wells integrate optical devices,” D&R Idustry Articles, 20-Feb-2002. Available: http://www.design-reuse.com/articles/2389/opto-electronics-quantum-wells-integrate-optical-devices.html.

[20] P. Harrison, Quantum Wells, Wires and Dots, John Wiley & Sons, Ltd. The Atrium, Southern Gate, Chichester: John Wiley & Sons, Ltd., 2005.

[21] A. Y. Shik, Quantum Wells: Physics & Electronics of Twodimensional Systems, 1st ed. World Scientific Pub Co Inc, 1997.

[22] A. Bauer et al., “Mid-infrared semiconductor heterostructure lasers for gas sensing applications,” Semiconductor Science and Technology, vol. 26, p. 014032, Jan. 2011.

[23] A. L. Luque and A. Viacheslav, Eds., “III-V Heterostructures in Photovoltaics,” in Concentrator Photovoltaics, vol. 130, Berlin, Heidelberg: Springer Berlin Heidelberg, pp. 25-50.

[24] Z. I. Alferov, “Nobel Lecture: The double heterostructure concept and its applications in physics, electronics, and technology,” Reviews of Modern Physics, vol. 73, no. 3, p. 767, Oct. 2001.

[25] Z. I. Alferov, V. M. Andreev, and V. D. Rumyantsev, “III-V Solar Cells and Concentrator Arrays,” in High-Efficient Low-Cost Photovoltaics, vol. 140, V. Petrova-Koch, R. Hezel, and A. Goetzberger, Eds. Berlin, Heidelberg: Springer Berlin Heidelberg, pp. 101-141.

[26] R. A. Smith, Semiconductors, 2nd ed. Cambridge University Press, London, 1978.

[27] D. C. Look, Electrical Characterization of GaAs Materials and Devices. John Wiley & Sons Inc, 1989.

[28] G. E. Stillman and C. M. Wolfe, “Electrical characterization of epitaxial layers,” Thin Solid Films, vol. 31, no. 1-2, pp. 69-88, Jan. 1976.

[29] O. Manasreh, *Semiconductor Heterojunctions and Nanostructures*, 1st ed. McGraw-Hill Professional, 2005.

[30] W. Walukiewicz, H. E. Ruda, J. Lagowski, and H. C. Gatos, “Electron mobility in modulation-doped heterostructures,” Physical Review B, vol. 30, no. 8, pp. 4571-4582, Oct. 1984.

[31] V. P. Kunets et al., “Interface roughness scattering in laterally coupled InGaAs quantum wires,” Applied Physics Letters, vol. 97, p. 262103, 2010.

[32] J. D. Plummer, M. Deal, and P. D. Griffin, Silicon VLSI Technology: Fundamentals, Practice, and Modeling, 1st ed. Prentice Hall, 2000.

[33] M. M.-A. J. Voncken, The epitaxial lift-off process: parameter studies and solar cell application. 2004.

[34] J. Renuka, “Approaching Fundamental Limits on Signal Detection,” Transaction on Electron Devices, vol. 41, no. 11, Nov. 1994.

[35] R. S. Popović, Hall effect devices. CRC Press, 2004.

[36] F. N. Hooge, “1/f noise sources,” IEEE Transactions on Electron Devices, vol. 41, no. 11, pp. 1926-1935, Nov. 1994.

[37] F. N. Hooge, “1/f noise is no surface effect,” Physics Letters, vol. 29, p. 139, 1969.

[38] P. Grigolini, G. Aquino, M. Bologna, M. LukoviÄ‡, and B. J. West, “A theory of noise in human cognition,” Physica A: Statistical Mechanics and its Applications, vol. 388, no. 19, pp. 4192-4204, Oct. 2009.

[39] F. N. Hooge, T. G. M. Kleinpenning, and L. K. J. Vandamme, “Experimental studies on 1/f noise,” Reports on Progress in Physics, vol. 44, pp. 479-532, May 1981.

[40] M. E. Levinshtein, “Nature of the volume 1/f noise in the main materials of semiconductor electronics: Si, GaAs, and SiC,” Physica Scripta, vol. 69, pp. 79-84, Jan. 1997.

[41] O. Jantsch, “Flicker (1/f) noise generated by a random walk of electrons in interfaces,” IEEE Transactions on Electron Devices, vol. 34, no. 5, pp. 1100- 1115, May 1987.

[42] L. K. .Vandamme, Xiaosong Li, and D. Rigaud, “1/f noise in MOS devices, mobility or number fluctuations?,” IEEE Transactions on Electron Devices, vol. 41, no. 11, pp. 1936-1945, Nov. 1994.

[43] L. K. .Vandamme, D. Rigaud, J.-M.Peransin, R. Alabedra, and J.-M. Dumas, “Gate current 1/f noise in GaAs MESFET’s,” IEEE Transactions on Electron Devices, vol. 35, no. 7, pp. 1071-1075, Jul. 1988.

[44] L. K. .Vandamme, “Noise as a diagnostic tool for quality and reliability ofelectronic devices,” IEEE Transactions on Electron Devices, vol. 41, no. 11, pp. 2176-2187, Nov. 1994.

[45] L. Ren, “Intrinsic and extrinsic 1/f noise sources in proton-irradiated n-GaAs epitaxial layers,” Journal of Applied Physics, vol. 74, p. 4534, 1993.

[46] B. Streetman and S. Banerjee, Solid State Electronic Devices, 6th ed. Prentice Hall, 2005.

[47] A. L. McWhorter, “1/f noise and related surface effects in germanium,” Massachusetts Institute of Technology: Cambridge, 1955.

[48] F. N. Hooge and P. A. Bobbert, “On the correlation function of 1/f noise,” Physica B: Condensed Matter, vol. 239, no. 3-4, pp. 223-230, Aug. 1997.

[49] F. N. Hooge and M. Tacano, “Experimental studies of 1f noise in n-GaAs,” Physica B: Condensed Matter, vol. 190, no. 2-3, pp. 145-149, Jul. 1993.

[50] L. K. .Vandamme, “Bulk and surface 1/f noise,” IEEE Transactions on Electron Devices, vol. 36, no. 5, pp. 987-992, May 1989.

[51] P. H. Handel, “Nature of 1/f Phase Noise,” Physical Review Letters, vol. 34, no. 24, p. 1495, Jun. 1975.

[52] A. van der Ziel, “Unified presentation of 1/f noise in electron devices: fundamental 1/f noise sources,” Proceedings of the IEEE, vol. 76, no. 3, pp. 233- 258, Mar. 1988.

[53] V. V. Carolyne M., “A survey of results and future prospects on quantum 1Æ’f noise and 1Æ’f noise in general,” Solid-State Electronics, vol. 34, no. 1, pp. 1-21, Jan. 1991.

[54] V. P. Kunets et al., “Deep traps in GaAs/InGaAs quantum wells and quantum dots, studied by noise spectroscopy,” Journal of Applied Physics, vol. 104, p. 103709, 2008.

[55] M. E. Levinshtein and S. L. Rumyantsev, “Noise spectroscopy of local levels in semiconductors,” Semiconductor Science and Technology, vol. 9, pp. 1183-1189, Jun. 1994.

[56] M. Tacano, “Hooge fluctuation parameter of semiconductor microstructures,” IEEE Transactions on Electron Devices, vol. 40, no. 11, pp. 2060-2064, Nov. 1993.

[57] M. Tacano and Y. Sugiyama, “1/f noise in GaAs filaments,” IEEE Transactions on Electron Devices, vol. 38, no. 11, pp. 2548-2553, Nov. 1991.

[58] M. Tacano, T. Kanayama, and Y. Sugiyama, “1/f noise in quarter-micron filaments of GaAs and InP made by focused ion-beam implantation,” Solid-State Electronics, vol. 34, no. 2, pp. 193-196, Feb. 1991.

[59] F. Scholz, J. M. Hwang, and D. K. Schroder, “Low frequency noise and DLTS as semiconductor device characterization tools,” Solid-State Electronics, vol. 31, no. 2, pp. 205-217, Feb. 1988.

[60] F. J. Scholz and J. W. Roach, “Low-frequency noise as a tool for characterization of near-band impurities in silicon,” Solid-State Electronics, vol. 35, no. 4, pp. 447-452, Apr. 1992.

[61] D. Sodini, G. Lecoy, D. Rigaud, and M. Rolland, “Impedance and noise in the channel of a GaAs Schottky-gate field-effect transistor,” Solid-State Electronics, vol. 20, no. 7, pp. 579-581, Jul. 1977.

[62] D. Sodini, A. Touboul, G. Lecoy, and M. Savelli, “Generation-recombination noise in the channel of GaAs Schottky-gate field-effect transistors,” Electronics Letters, vol. 12, no. 2, pp. 42-43, Jan. 1976.

[63] V. Kunets, “Micro-Hall Devices Based onHigh-Electron-Velocity Semiconductors,” Humboldt University, Germany, 2004.

[64] J. A. Copeland, “Semiconductor impurity analysis from low-frequency noise spectrum,” Trans. Electron Devices, vol. 18, pp. 50-53, 1971.

[65] V. P. Kunets et al., “Generation–recombination noise in doped-channel $Al_{0.3}Ga_{0.7}As/GaAs/In_{0.2}Ga_{0.8}As$ quantum well micro-Hall devices,” Journal of Applied Physics, vol. 94, p. 7590, 2003.

[66] L. Ren, “Intrinsic and extrinsic 1/f noise sources in proton-irradiated n-GaAs epitaxial layers,” Journal of Applied Physics, vol. 74, no. 7, pp. 4534-4539, Oct. 1993.

[67] L. Ren and F. N. Hooge, “Temperature dependence of $1/f$ noise in epitaxial n-type GaAs,” Physica B: Condensed Matter, vol. 176, no. 3, pp. 209-212, Mar. 1992.

[68] K. T.G.M., “Scattering mechanisms and 1f noise in semiconductors,” Physica B+C, vol. 103, no. 2-3, pp. 345-347, Feb. 1981.

[69] J. R. Kirtley, T. N. Theis, P. M. Mooney, and S. L. Wright, “Noise spectroscopy of deep level (DX) centers in GaAs-AlxGa1-xAs heterostructures,” Journal of Applied Physics, vol. 63, no. 5, pp. 1541-1548, Mar. 1988.

[70] J.-P. Teyssier, P. Bouysse, Z. Ouarch, D. Barataud, T. Peyretaillade, and R. Quere, “40-GHz/150-ns versatile pulsed measurement system for microwavetransistor isothermal characterization,” IEEE Transactions on Microwave Theory and Techniques, vol. 46, no. 12, pp. 2043-2052, Dec. 1998.

## Appendix A: Noise Spectra Analysis on the Matter of Traps and Impurity States for All Samples

All these spectra were estimated. For all these graphs $\omega=2\pi f$, where f is the frequency that was used during the experiment.

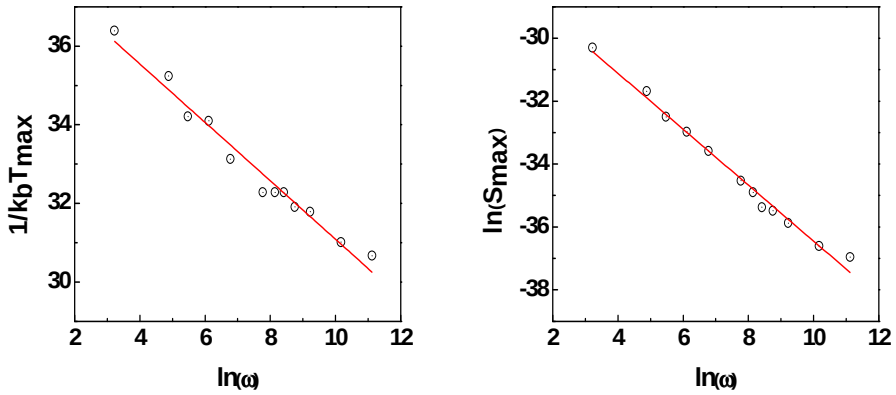


Figure A.1. Plots of $S_{max}(\omega)$and $T_{max}(\omega)$for $REF_U$ sample (Trap1).

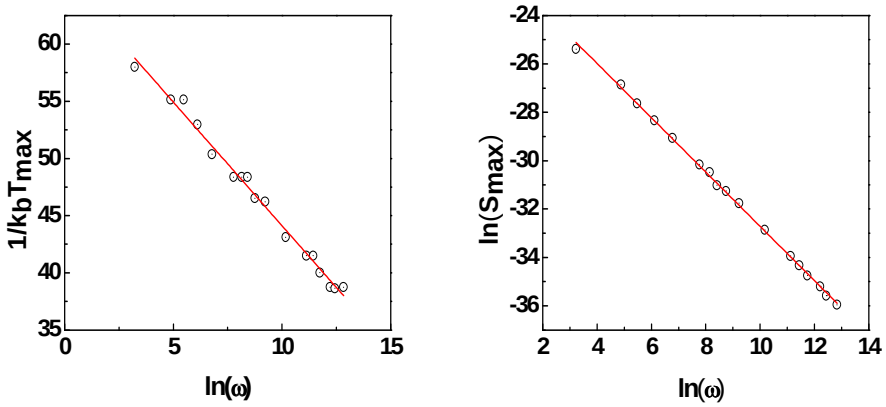


Figure A.2. Plots of $S_{max}(\omega)$and $T_{max}(\omega)$for $REF_U$ sample (Trap2).

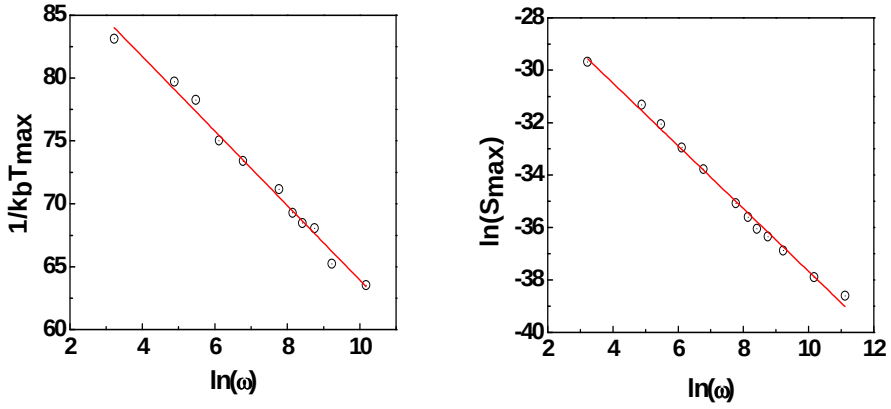


Figure A.3. Plots of $S_{max}(\omega)$and $T_{max}(\omega)$for $REF_U$ sample (Trap3).

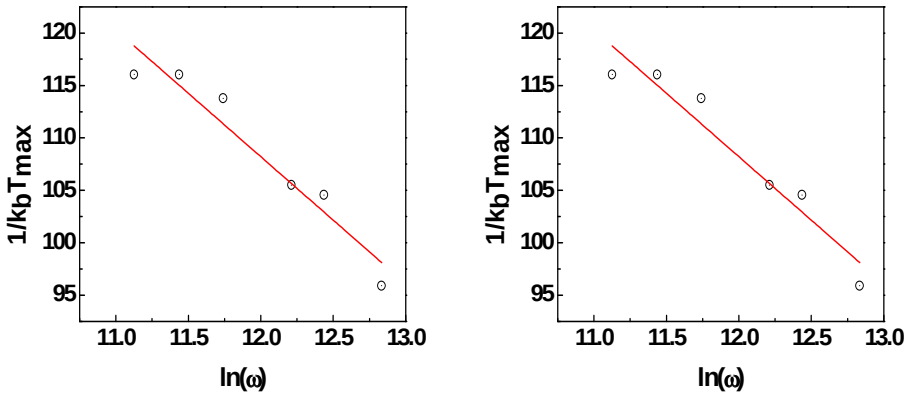


Figure A.4. Plots of $S_{max}(\omega)$and $T_{max}(\omega)$for $REF_U$ sample (Trap4).

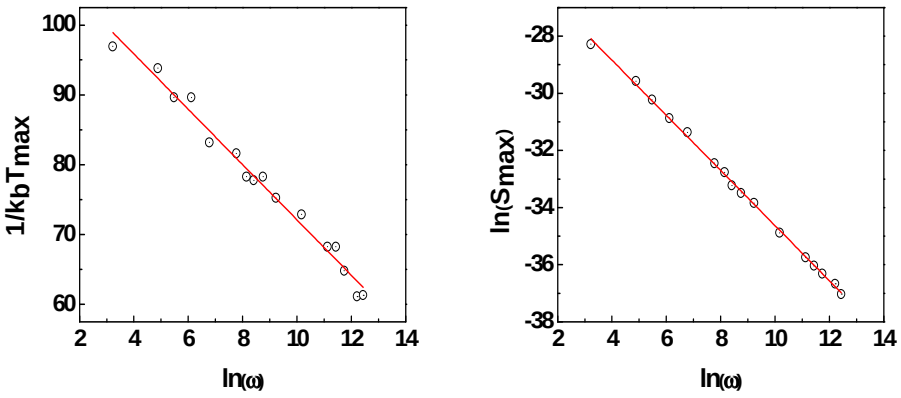


Figure A.5. Plots of $S_{max}(\omega)$and $T_{max}(\omega)$for $E_{1.0}$ sample (Trap1).

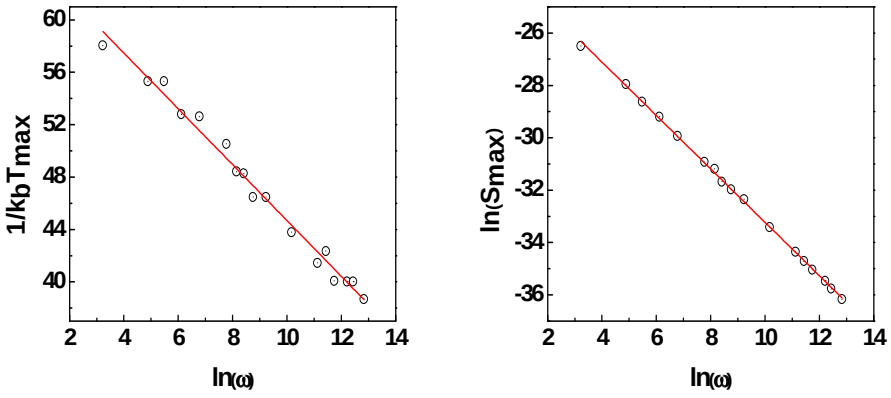


Figure A.6. Plots of $S_{max}(\omega)$and $T_{max}(\omega)$for $E_{1.0}$ sample (Trap2).

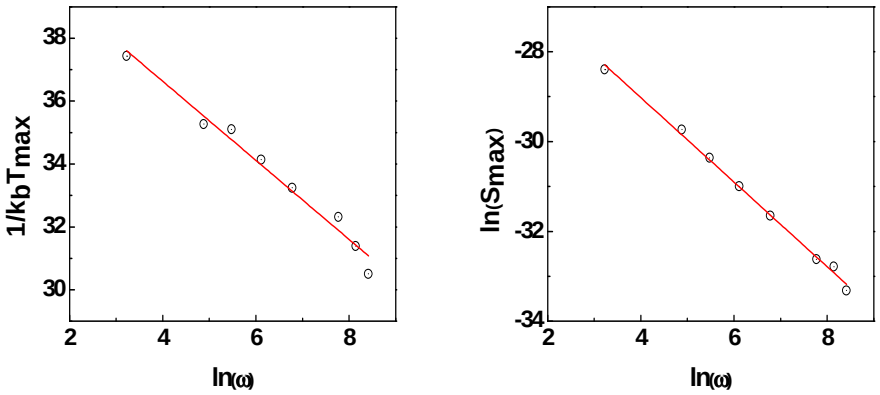


Figure A.7. Plots of $S_{max}(\omega)$and $T_{max}(\omega)$for $E_{1.0}$ sample (Trap3).

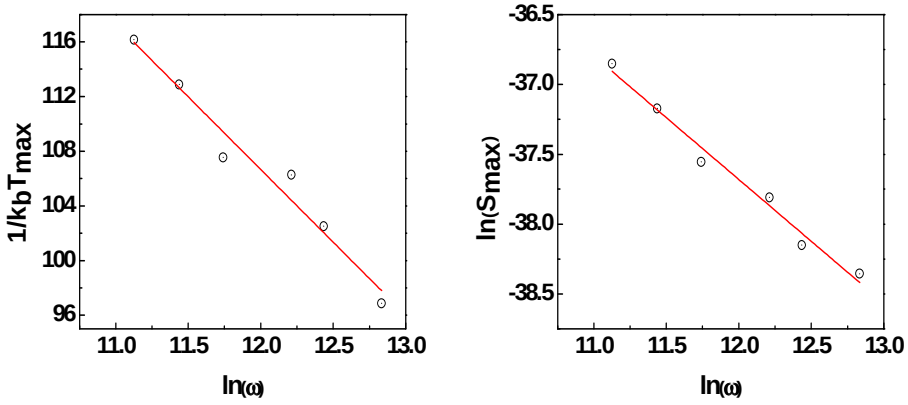


Figure A.8. Plots of $S_{max}(\omega)$and $T_{max}(\omega)$for $E_{0.8}$ sample (Trap1).

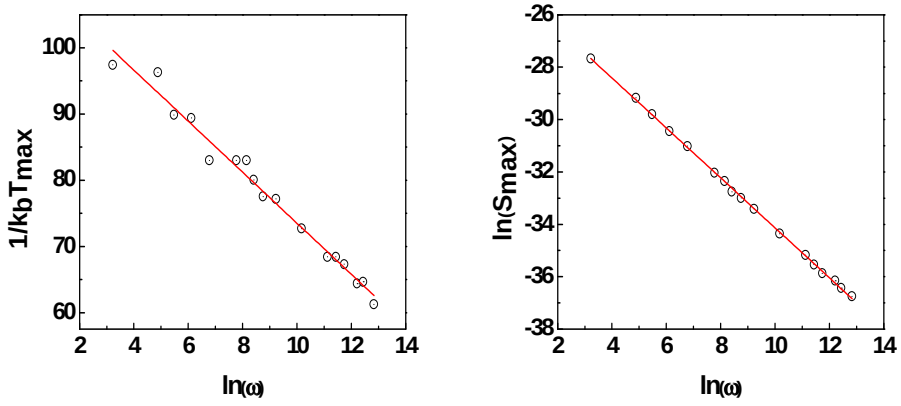


Figure A.9. Plots of $S_{max}(\omega)$and $T_{max}(\omega)$for $E_{0.8}$ sample (Trap2).

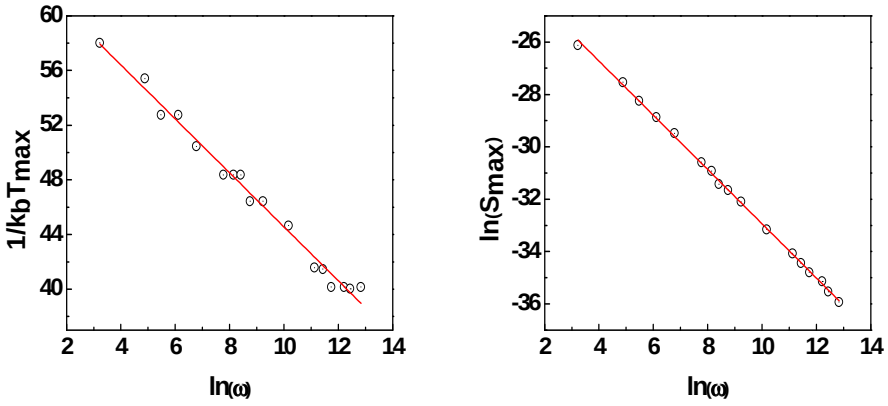


Figure A.10. Plots of $S_{max}(\omega)$and $T_{max}(\omega)$for $E_{0.8}$ sample (Trap3).

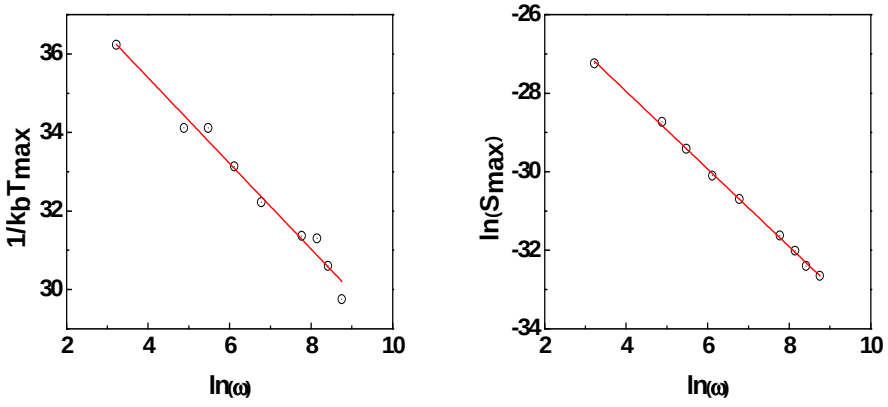


Figure A.11. Plots of $S_{max}(\omega)$and $T_{max}(\omega)$for $E_{0.8}$ sample (Trap4).

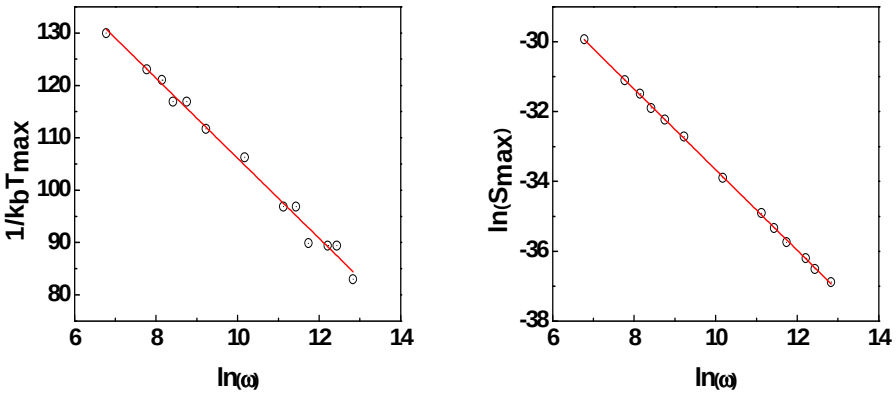


Figure A.12. Plots of $S_{max}(\omega)$and $T_{max}(\omega)$for $E_{0.5}$ sample (Trap1).

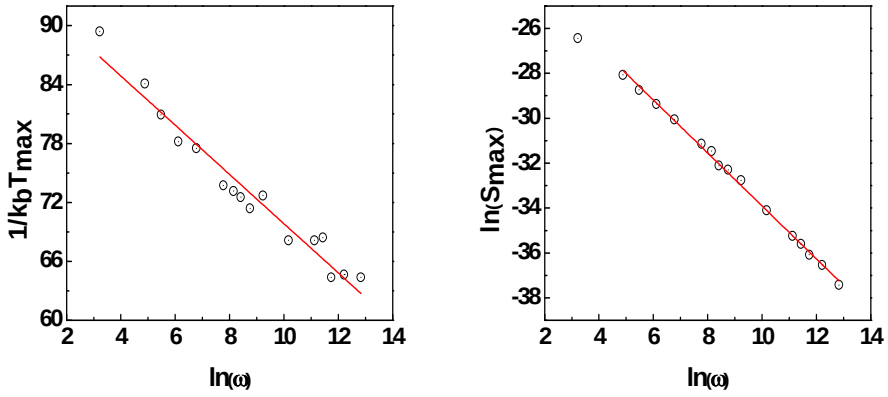


Figure A.13. Plots of $S_{max}(\omega)$and $T_{max}(\omega)$for $E_{0.5}$ sample (Trap2).

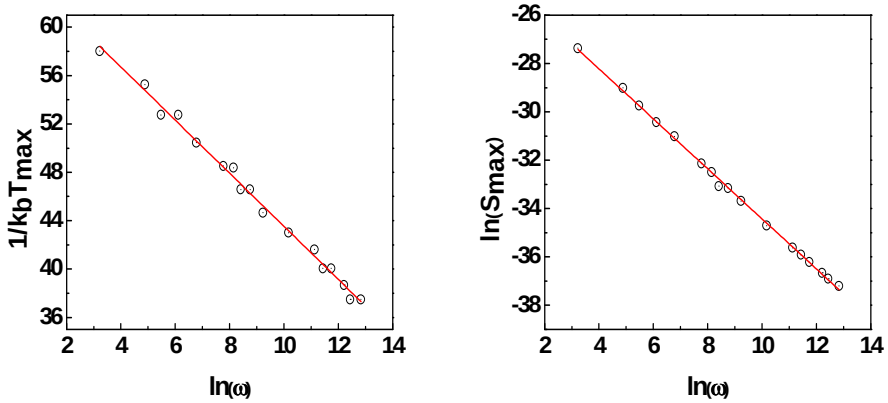


Figure A.14. Plots of $S_{max}(\omega)$and $T_{max}(\omega)$for $E_{0.5}$ sample (Trap3).

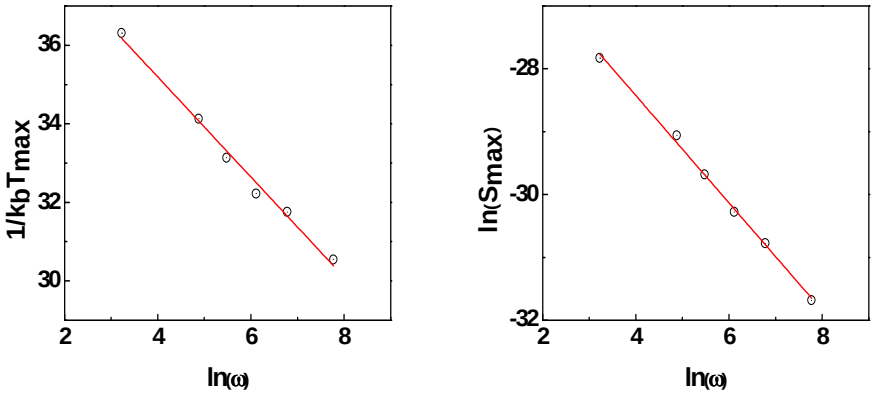


Figure A.15. Plots of $S_{max}(\omega)$and $T_{max}(\omega)$for $E_{0.5}$ sample (Trap4).

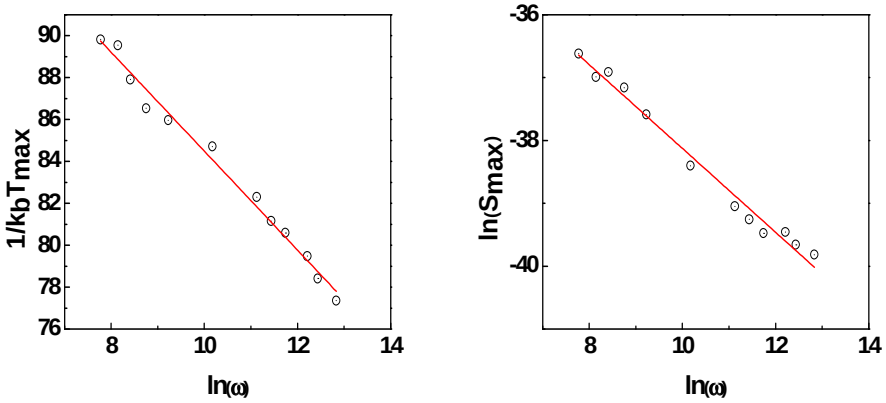


Figure A.16. Plots of $S_{max}(\omega)$and $T_{max}(\omega)$for $REF_{\delta}$ sample (Trap1).

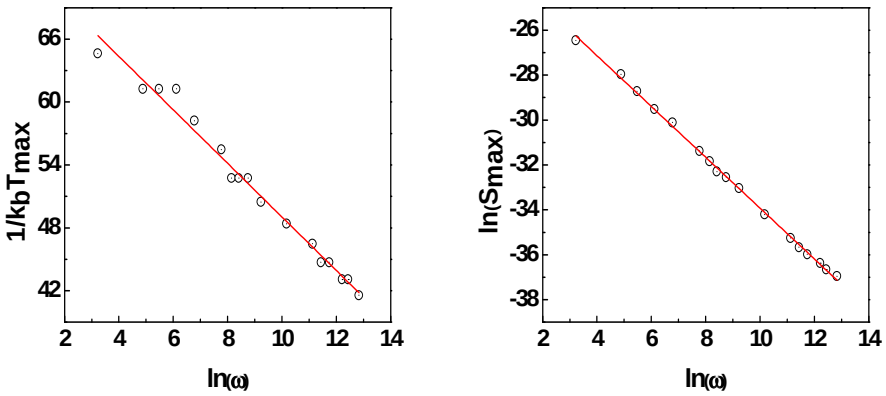


Figure A.17. Plots of $S_{max}(\omega)$and $T_{max}(\omega)$for $REF_{\delta}$ sample (Trap2).

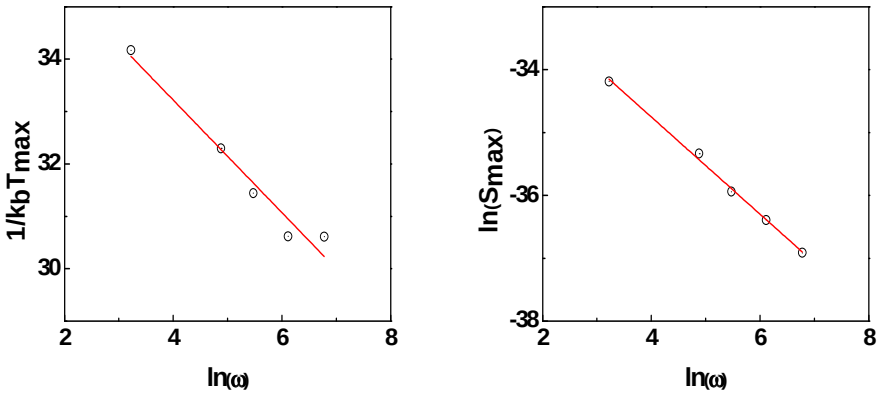


Figure A.18. Plots of $S_{max}(\omega)$and $T_{max}(\omega)$for $REF_{\delta}$ sample (Trap3).

## Appendix B: Description of Research for Popular Publication

### BREAKING THE OHM'S LAW: IS IT FANTASY OR REALITY?

Every year there are a lot of changes take place in the world technology and science that result in new devices that operate with novel physical approach. With development of new technologies, e.g. Molecular Beam Epitaxy (MBE), it turns out to be possible to grow new materials with very high precision and different complexity. In other words, by using MBE each individual atom of different materials can accurately be places on top of each other in order to form a new crystal structure. And as a result new properties of these crystals can be achieved.

Nowadays the MBE technique has been greatly developed and such complicated structures as quantum wells (QWs) can be easily grown. In order to form the QW one layer of GaAs has to be sandwiched between two other layers of AlGaAs which have higher band gap and will form barriers for GaAs (see Figure 1).

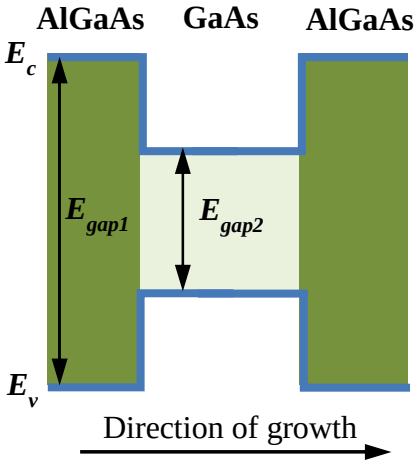


Figure 1. Bandgap diagrams for a single quantum well.

Specific structures of GaAs/AlGaAs materials can be used in high-speed electronics to create a device that will work as an oscillator and amplifier. One way to generate these high frequencies in solid state semiconductor devices with applying of electric field is to have the negative differential resistance (NDR) in this device.

At the University of Arkansas this NDR phenomena was deeply investigated in Prof. Gregory Salamo research group. According to Nazariy Andrushchak, Master student who was working on this project "The telecommunications and all its applications are moving into the range of high frequencies. That is why it can very important to have some type of the device that can perform at high frequencies range. And because of the fact that QW heterostructures with remote doping have extremely high electron mobility, they can be the best candidates as novel materials for future high-speed electronics and communication".

The simplest QW heterostructure that can be grown by MBE is depicted in Figure 2.

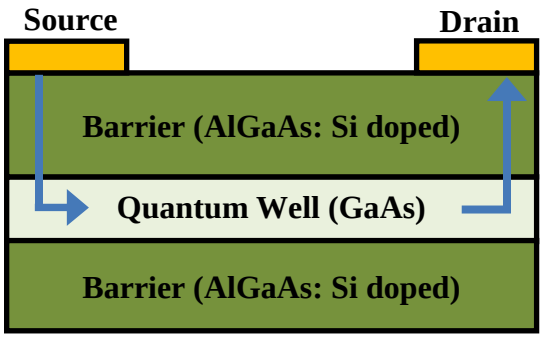


Figure 2. The simple quantum well heterostructure grown by MBE with ohmic contacts on top.

It is worse to mention, that the electrons for the structure in Figure 2 will be able to move only in the in-plane direction

of GaAs material, and movement in the AlGaAs direction will be limited. On top of this system two ohmic contacts are mounted in order to perform electric characterization measurements.

It is well known that for the system that has ohmic contacts (the resistance of these contacts does not play any role in the electric properties of the material), by performing current-voltage measurements it will be possible to achieve the behavior that is shown in Figure 3a.

However, at high electric fields, the current-voltage curve might behave differently. As it can be seen in Figure 3b with applying more electric field at some voltage $V_T$ the current starts to decrease with increasing of voltage up to $V_d$. After that point, with further increase of voltage through the device the current will be increased, but with lower speed (because of smaller slope).

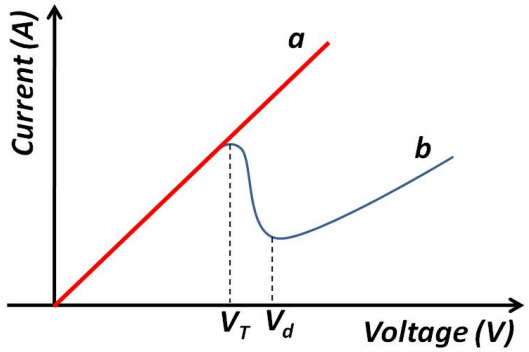


Figure 3. The I-V curve for semiconductor device system with (a) typical I-V behavior, and (b) in system that has negative differential resistance region.

This region, where with increasing of voltage the current decreases, called NDR region.

However, before start using any new materials for certain applications, in deep analysis has to be performed to understand the mechanism of real space charge transfer (RST) that leads to NDR. At low electric field the electrons will be located in the quantum well. However, with increasing of the electric field these electrons will get enough energy to overcome the AlGaAs barrier. As result of this movement the majority of conductive electrons will be transferred to the AlGaAs and the behavior of this material will be changed. The process of this electron transfer that is shown in Figure 4 is called real space charge transfer.

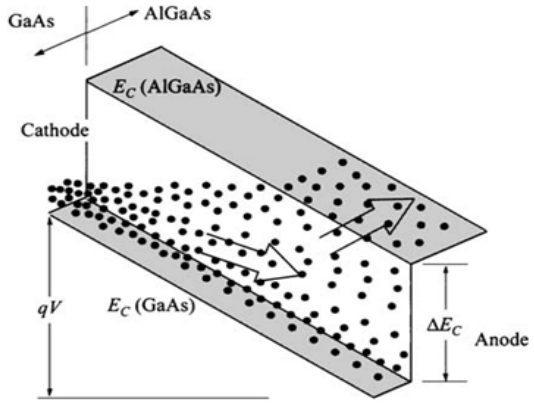


Figure 4. Energy-band diagram that shows the RST mechanism occurring at applied high electric field [1].

At the University of Arkansas the RST mechanism was explained for $Al_{0.3}Ga_{0.7}As$/GaAs system with using the schematic diagram of the conduction band that is depicted in Figure 5.

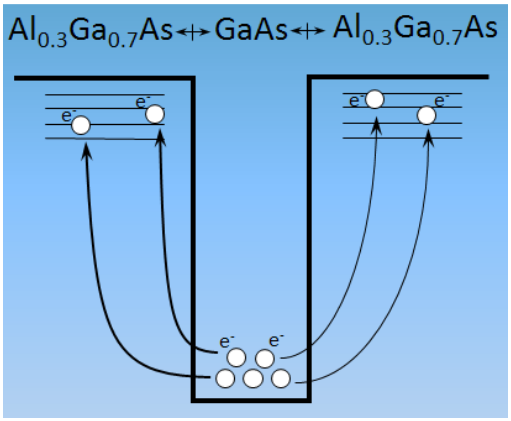


Figure 5. Schematic diagram of the conduction band for $Al_{0.3}Ga_{0.7}As$/GaAs system.

Numbers of steps were done to explain this RST mechanism. Initially, by using MBE technique different samples with different Si doping concentration were grown. These doping concentrations were varied in order to achieve different amount of impurity states in AlGaAs layer, which played a role of electron traps. These traps were used as locations for those electrons, which were transferred from the QW after high electric field was applied to the sample. Hence, samples with QW were grown and by using photolithography technique special pattern were applied. Next, the Hall effect measurements were performed to measure mobility and carrier density in order to differentiate between different scattering mechanisms. After that, the Deep Level Noise Spectroscopy was applied to investigate samples on the matter of impurity states and defects. Later on pulsed I-V measurements were performed to observe the NDR.

"This amount of experiments was enough to prove the presence of NDR in these samples", said Nazariy Andrushchak. "However, in order to explain how RST mechanism occurs in these samples and where electrons were transferred the lock-in technique with light excitation and temperature cycling was applied". After these experiments were done it was possible to conclude that electron transfer take place from the QW to the impurities that were located in the AlGaAs.

Professor Salamo's research group from University of Arkansas was able to show the presence of NDR in samples that were grown using the MBE technique, and also to explain the mechanism of real space charge transfer (RST) that results in NDR. "Based on this fundamental research it will be possible to get sufficient information about the system structure and its behavior for its further application in high-speed electronics", said Nazariy Andrushchak.

**References**

[1] S. M. Sze and K. K. Ng, *Physics of semiconductor devices*. John Wiley and Sons, 2007.

## Appendix C: Executive Summary of Newly Created Intellectual Property

The summary of results obtained in this work for potential Intellectual Property creation are:

(1) New recipes for quantum well heterostructure MBE growth which exhibit NDR were created.

(2) New experimental setup for band to band light excitation at different temperatures.

(3) The LabView code which was specially developed to analyze the noise spectral density data received from applying Deep Level Noise Spectroscopy technique.

## Appendix D: Potential Patent and Commercialization Aspects of listed Intellectual Property Items

### D.1. Patentability of Intellectual Property (Could Each Item be Patented)

The three items listed were considered first from the perspective of whether or not the item could be patented.

(1) New recipes for quantum well heterostructure MBE growth which exhibit NDR were created. These recipes can be patented. However, in order to do this more in deep analysis has to be performed for better understanding the properties of the materials.

(2) A new experimental setup for band to band light excitation at different temperatures was created only for this particular project needs. However, it can be patented.

(3) The LabView code which was specially developed to analyze the noise spectral density data that was received from applying Deep Level Noise Spectroscopy technique cannot be patented, because several modules of the code were taken from the standard LabView drivers library provided by National Instruments.

### D.2. Commercialization Prospects (Should Each Item Be Patented)

The three items listed were then considered from the perspective of whether or not the item should be patented.

(1) New recipes for quantum well heterostructure MBE growth which exhibit NDR should not be patented because any change in the thickness of this structure can be considered as a new structure. Hence, it is impossible to protect all variants for structure growth.

(2) A new experimental setup for band to band light excitation at different temperatures was created only for these particular project needs, so the range of its application is

very limited. Hence, it has very narrow range of applications in compare to other commercial available setups of the similar principle of operation. Therefore, it should not be patented.

(3) As this has been shown that it cannot be patented, no discussion of should it be patented is needed.

**D.3. Possible Prior Disclosure of IP**

The following items were discussed in a public forum or have published information that could impact the patentability of the listed IP.

(1) New recipes for quantum well heterostructure MBE growth which exhibit NDR have not been discussed in any forum.

## Appendix E. Societal and Environmental Impact of Research

### 1. Applicability of research methods to other problems

The methodology to study the density of noise can be used to perform similar measurements for other heterostructure systems that contain quantum dots and quantum wires. Furthermore, this methodology can be used to analyze even more complicated heterostructures on the matter of impurity states and defects.

### 2. Impact of research results on US and global society

The research results obtained from this thesis can be used to create a high-frequency type of the devices, such as: the local oscillators, power amplifiers and field effect transistors, which can perform in the frequency range from 1 to 300 GHz. If it will be possible to create these types of devices, the global society as well as U.S. will experience increase in speed of computers operation, data transferring and better quality of telecommunication services.

### 3. Impact of research results on the environment

All the samples that were used in this thesis were grown using MBE. Nowadays, MBE is considered as one of the cleanest fabrication techniques because all the growth takes place in the ultra-high vacuum conditions and the samples contain no toxic waste. Fabrication of special pattern on these samples by applying photolithography techniques and also creating metal contacts was performed in the special lab, where all used materials were properly utilized. The equipment and materials that were used for electrical characterization measurements had no impact on the environment as well.

## Appendix F: Microsoft Project for MS Microelectronics-Photonics Degree Plan

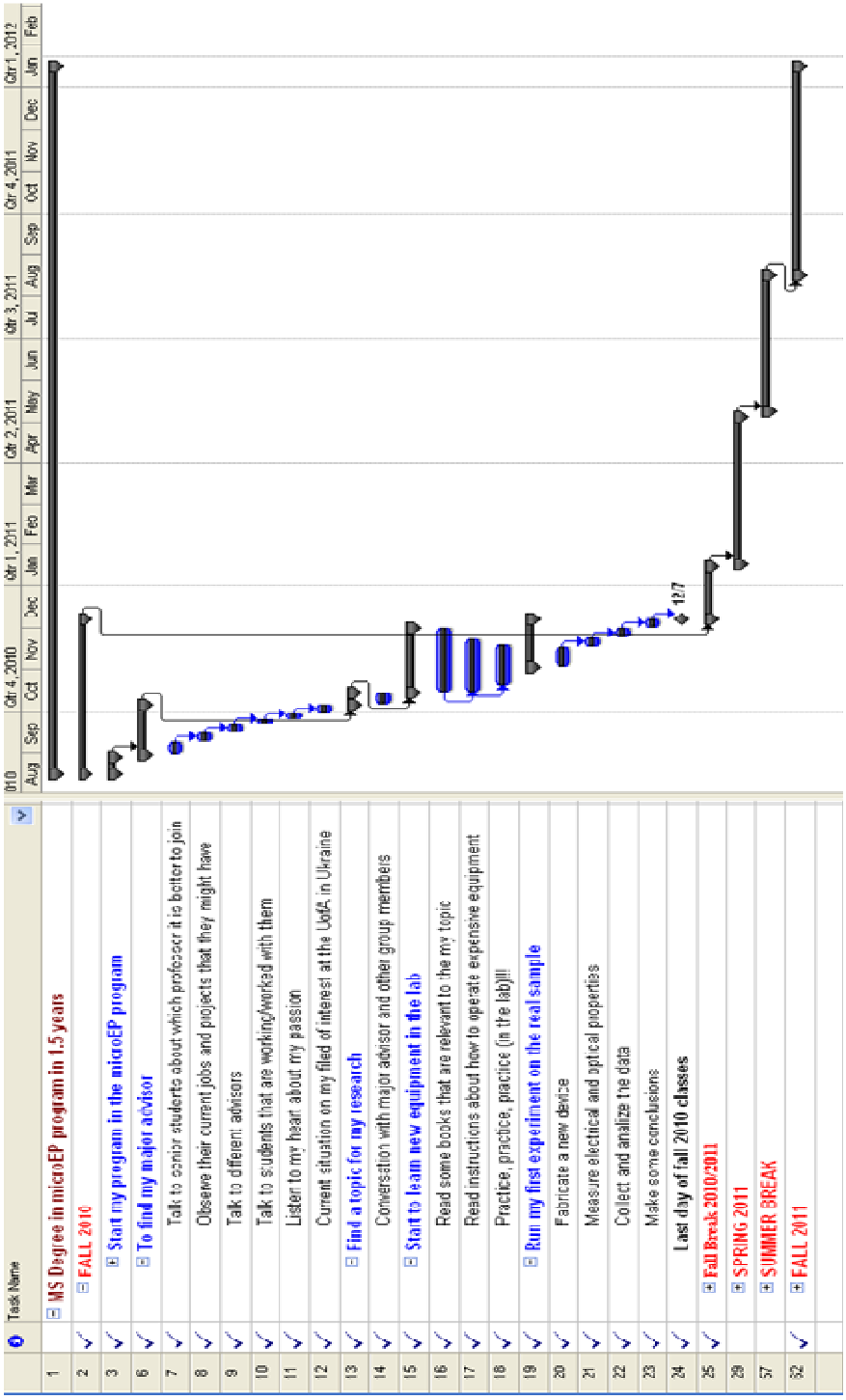

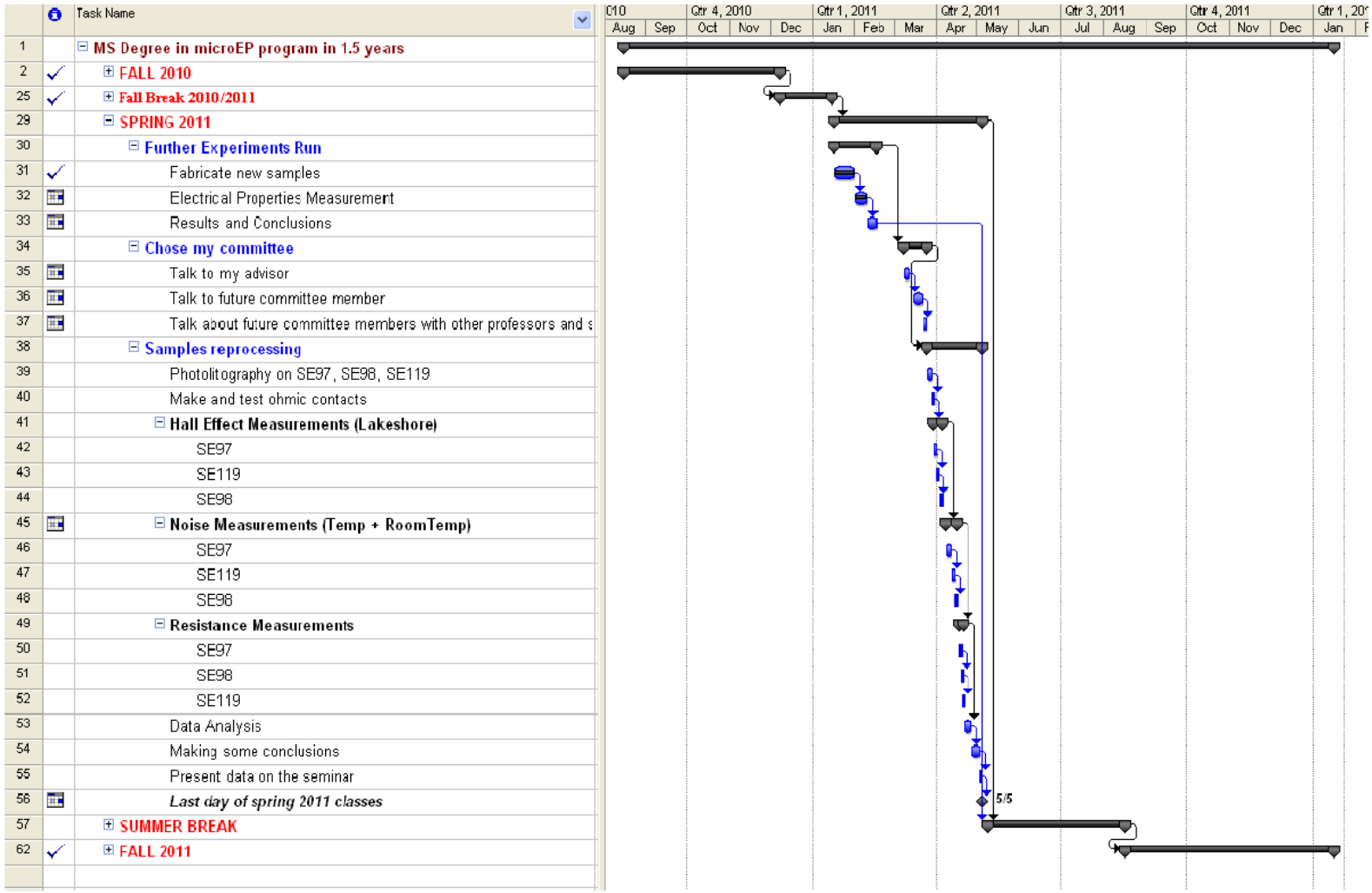

| | | Task Name |
|---|---|---|
| 1 | | MS Degree in microEP program in 1.5 years |
| 2 | ✓ | FALL 2010 |
| 25 | ✓ | Fall Break 2010/2011 |
| 29 | | SPRING 2011 |
| 30 | | Further Experiments Run |
| 31 | ✓ | Fabricate new samples |
| 32 | | Electrical Properties Measurement |
| 33 | | Results and Conclusions |
| 34 | | Chose my committee |
| 35 | | Talk to my advisor |
| 36 | | Talk to future committee member |
| 37 | | Talk about future committee members with other professors and s |
| 38 | | Samples reprocessing |
| 39 | | Photolitography on SE97, SE98, SE119 |
| 40 | | Make and test ohmic contacts |
| 41 | | Hall Effect Measurements (Lakeshore) |
| 42 | | SE97 |
| 43 | | SE119 |
| 44 | | SE98 |
| 45 | | Noise Measurements (Temp + RoomTemp) |
| 46 | | SE97 |
| 47 | | SE119 |
| 48 | | SE98 |
| 49 | | Resistance Measurements |
| 50 | | SE97 |
| 51 | | SE98 |
| 52 | | SE119 |
| 53 | | Data Analysis |
| 54 | | Making some conclusions |
| 55 | | Present data on the seminar |
| 56 | | *Last day of spring 2011 classes* |
| 57 | | SUMMER BREAK |
| 62 | ✓ | FALL 2011 |

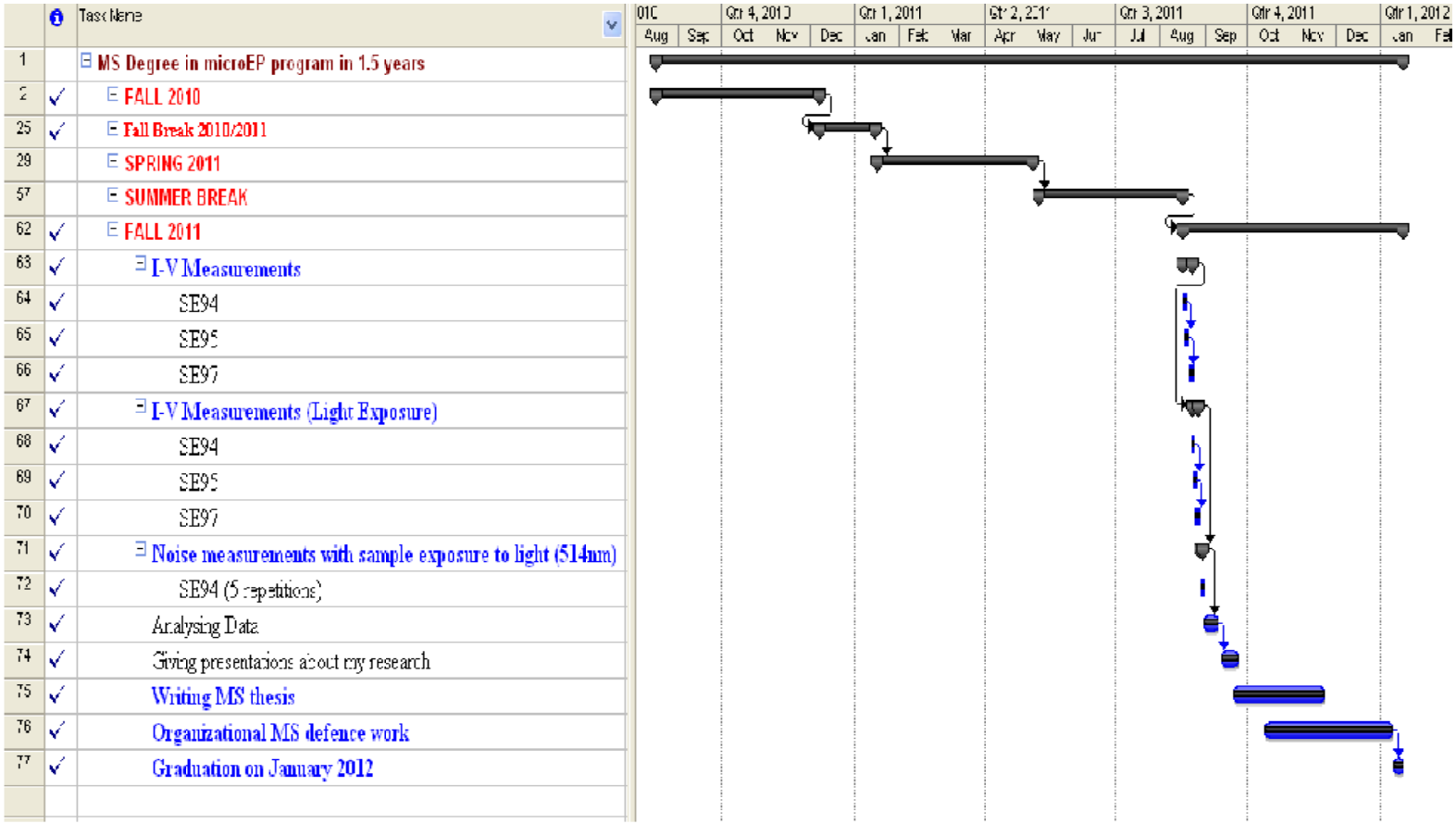

| | | Task Name |
|---|---|---|
| 1 | | MS Degree in microEP program in 1.5 years |
| 2 | ✓ | FALL 2010 |
| 25 | ✓ | Fall Break 2010/2011 |
| 29 | | SPRING 2011 |
| 57 | | SUMMER BREAK |
| 62 | ✓ | FALL 2011 |
| 63 | ✓ | I-V Measurements |
| 64 | ✓ | SE94 |
| 65 | ✓ | SE95 |
| 66 | ✓ | SE97 |
| 67 | ✓ | I-V Measurements (Light Exposure) |
| 68 | ✓ | SE94 |
| 69 | ✓ | SE95 |
| 70 | ✓ | SE97 |
| 71 | ✓ | Noise measurements with sample exposure to light (514nm) |
| 72 | ✓ | SE94 (5 repetitions) |
| 73 | ✓ | Analysing Data |
| 74 | ✓ | Giving presentations about my research |
| 75 | ✓ | Writing MS thesis |
| 76 | ✓ | Organizational MS defence work |
| 77 | ✓ | Graduation on January 2012 |

## Appendix G: Software Used in This Research

**Computer #1:** Laptop
Model Number & Serial Number: Gateway M250, 0036648557
Location: Moves (typically, lab or home)
Owner: Nazariy Andrushchak
**Software #1:**
Name: OriginPro 8 Student Version
Purchased By: Nazariy Andrushchak
**Software #2:**
Name: MS Office 2007
Purchased By: Nazariy Andrushchak
**Software #3:**
Name: LabView 2010 Student Version
Purchased By: Nazariy Andrushchak

**Computer #2:** Desktop
Model Number & Serial Number: Digital Instruments P4, 400220-002
Location: NANO 152
Owner: Dr. Greg Salamo
**Software #1:**
Name: Lab View 2007
Purchased By: Dr. Greg Salamo

**Computer #3:** Desktop
Model Number & Serial Number: Gateway Pentium, 236452
Location: NANO 152
Owner: Dr. Greg Salamo
**Software #1:**
Name: MMR Hall and Van der Pauw Measurement System
Purchased By: Dr. Greg Salamo

**Computer #4:** Desktop
Model Number & Serial Number: Dell Optiplex, DRXM5
Location: NANO 152
Owner: Dr. Greg Salamo
**Software #1:**
Name: Metrics
Purchased By: Dr. Greg Salamo